Control Methods of Powertrains with Backlash and Time Delay

Vom Promotionsausschuss der
Technischen Universität Hamburg
zur Erlangung des akademischen Grades
Doktor-Ingenieurin (Dr.-Ing.)
genehmigte Dissertation

von

Hong Truc Pham

aus

Stuttgart

2019

1. Gutachter: Prof. Dr.-Ing. Robert Seifried
2. Gutachter: Prof. Dr.-Ing. Herbert Werner
Tag der mündlichen Prüfung: 5. April 2019

MuM Notes in Mechanics and Dynamics

Editor: Prof. Dr.-Ing. Robert Seifried
Hamburg University of Technology
Institute of Mechanics and Ocean Engineering (MuM)
www.tuhh.de/mum

Volume 2
Hong Truc Pham
"Control Methods of Powertrains with Backlash and Time Delay"
Hamburg, 2019
© Copyright Hong Truc Pham 2019

Vorwort

Die vorliegende Dissertation ist während eines Kooperationsprojekts zwischen dem Institut für Mechanik und Meerestechnik der Technischen Universität Hamburg und der digitalen Antriebsentwicklung der Porsche AG entstanden.

Ich möchte mich hierbei bei allen herzlich bedanken, die in den letzten Jahren zum Gelingen dieser Arbeit beigetragen haben. Besonders hevorheben möchte ich

- Prof. Dr.-Ing. Robert Seifried an erster Stelle, der mich beispielhaft in der gesamten Promotionszeit als Erstgutachter unterstützte. Insbesondere dafür, dass er stets großes Interesse an meinem Thema zeigte, wertvolle Impulse zur Berarbeitung des Projekts gab und sich immer Zeit nahm. Vielen Dank für die hervorragende Zusammenarbeit.
- Herrn Dr. Christan Scholz, der die Anregung zur Bearbeitung dieses interessanten und vielseitigen Themas gab. Zudem mit seinem Erfahrungsschatz und wertvollen Ratschlägen ein wichtiger Begleiter des Projekts war.
- Prof. Dr.-Ing. Herbert Werner, für die Übernahme des Zweitgutachtens und die kompetente Diskussion in der Promotionsprüfung.
- Prof. Dr.-Ing. Friedrich Wirz, der als Prüfungsvorsitzender maßgeblich für eine angenehme Stimmung während der Prüfung sorgte.
- Herrn Gerd Bofinger und Dr. Bruno Kistner für die Ermöglichung dieses Kooperationsprojekts und das mir entgegengebrachte Vertrauen.
- Die Studenten, die in Form einer Abschlussarbeit oder eines Praktikums mich in meinem Promotionsprojekt unterstützten. Insbesondere gilt mein Dank Andreas Hock, Lutz Mager und Simon Speidel.
- Meine Kolleginnen und Kollegen am Institut für Mechanik und Meerestechnik für den wissenschaftlichen Austausch und ihre große Gastfreundschaft. Die Besuche am Institut waren für mich immer eine sehr schöne Zeit.
- Meine Familie und Freunde, dafür dass ihr die Konstanten in meinem Leben seid und ich immer auf euch zählen kann.
- Zu guter Letzt Dominik, mein Begleiter und meine größte Unterstützung im Leben.

Leonberg, im April 2019 Truc Pham

To my parents

Contents

Symbols

The following is a list of important symbols that appear in this thesis. Multidimensional vector quantities and matrices are marked by bold font. Scalar and one dimensional vector quantities are displayed in normal font. Some symbols have multiple meanings, however, the correct assignment will appear from the context in the dissertation.

Acronyms

A/D	analog to digital
BEV	battery electric vehicle
D/A	digital to analog
DIFF	differential
ds	drive shaft
EM	electric machine
FB	feedback
FF	feedforward
HEV	hybrid electric vehicle
ICE	internal combustion engine
IS	input shaft (gear)
PE	power electronics
PHEV	plug-in hybrid electric vehicle
REF	reference
rpm	revolutions per minute
SISO	single-input/single-output
SP	Smith Predictor
TD	torsional damper
TM	transmission
VEH	vehicle
ZOH	zero order hold

Latin Minuscules

a	longitudinal acceleration
c	spring stiffness
d	viscous damping coefficient
e	error
f	frequency
k	sampling step
k_p	proportional control gain
$\mathbf{k}$	control gain vector
m	mass of a body
n	system order
p	minimal coordinates
$\mathbf{q}$	modal coordinates
r	radius
s	displacement
u	system input
v	velocity
$\mathbf{x}$	state vector
y	system output
z	flat output or discrete eigenvalue

Latin Capitals

$\mathbf{A}$	system matrix
$\mathbf{B}$	input matrix or observability matrix
$\mathbf{C}$	output matrix
$\mathbf{D}$	damping matrix or feedthrough matrix
F	force
G	transfer function
$\mathbf{I}$	identity matrix
J	moment of inertia
$\mathbf{K}$	stiffness matrix or controller
$\mathbf{M}$	mass matrix
N	degree of freedom
$\mathbf{P}$	controllability matrix
R	gear ratio
T	torque, period
$\hat{\mathbf{X}}$	modal matrix

Greek Letters

α	half backlash gap
δ	disturbance torque
Δ	difference
$\Delta\varphi$	torsion rotation angle
$\Delta\omega$	torsion angular velocity
Θ	summarized moments of inertia
λ	eigenvalue
ξ	damping ratio
σ	fade-out function
τ	time delay
$\boldsymbol{\phi}$	transformation matrix
φ	rotation angle
ω	angular velocity in rad/s or rpm
ω_b	bandwidth in rad/s
ω_0	sampling frequency in rad/s

Abstract

A major current focus in vehicle development is to accomplish multiple objectives simultaneously: more comfort, more agile dynamic behavior and components protection. These goals are often in conflict with each other, since high performance driving maneuvers often cause powertrain oscillations. These oscillations are uncomfortable for the passengers and stressing for powertrain components. Therefore, methods are required to reduce driveline oscillations, but preserve high performance. The increase of electronics in cars enables to reduce undesired driveline oscillations by using intelligent functions. Electronic functions have the main advantage that no physical changes of vehicle components are necessary and therefore no weight is added. Furthermore, control functions are flexible and can be easier adapted to different powertrain types than mechanical approaches.

This dissertation focuses on the design of powertrain control functions for conventional, hybrid electric, and battery electric vehicles to reduce driveline oscillations. The goal of the control design is to accomplish all three goals in the best possible way by using knowledge of the oscillation behavior of the powertrain system. Thereby, lower frequency oscillations up to eight hertz are focused in this work. Detailed simulation models and reduced control models of conventional, hybrid electric, and battery electric powertrains are derived and analyzed. Based on the derived linear control models, a flatness-based feedforward controller is designed with arbitrary chosen transition time to prevent driveline oscillations. Furthermore, the flatness-based approach generates desired trajectories for feedback control. Then, extensions of backlash and time delay dynamics are given. First, backlash control is investigated. Backlash is necessary in mechanical systems due to tolerances and easy mounting and can therefore not be avoided. In particular, the effect of backlash is significant during load changes from pull to thrust condition and vice versa. Therefore, the linear flatness-based approach is extended by a smooth nonlinear backlash model and feedforward and feedback controller are designed based on this extension. Second, the destabilizing effect of time delay is focused and compensation methods are derived. Time delay can occur in control systems due to electric and mechanical reasons. The powertrain control system is considered as a digital system in order to take sampling time into account. Then, the closed loop stability of time delayed systems is investigated using stability diagrams. Compensation methods, namely, Smith predictor, observer based design, and state prediction are derived to enable well damped controlled systems with time delay. Finally, the two control approaches are combined for control of powertrain systems with backlash and time delay in an ad-hoc approach.

All control approaches are evaluated in time simulation and partly in test drives. Simulation studies and experimental results show improved performance, drive comfort and stability by applying the developed approaches, such that the addressed goal conflict can be solved.

Chapter 1

Introduction

1.1 Motivation

Electronic systems in passenger cars play a major part regarding the current in-depth changes in the automotive development. The automotive industry has to face the challenges of electrification, autonomous driving, and connected vehicles as new chances, see [Sommer17]. Furthermore, [Barra16] announces that the automotive industry is in the midst of seeing more changes in the next five years than it has seen in the last fifty years. In order to enable all these changes, intelligent functions are necessary. These functions undertake tasks of the driver and perform them often even better. For instance, an automatic dual-clutch transmission can provide full shift comfort, and significantly improved fuel efficiency and performance towards manual actions of a driver, as addressed in [Matthes05]. The remarkable increase of electronics in vehicles in recent years, as described in [MencherEtAl14] or [BayindirGözüküçükTeke11], allows to develop these functions in a wide range. Thereby, the cost of electronics in cars is expected to reach more than 30% of the overall costs by 2017, as presented in [PwC13]. Further increase is expected and the automobile evolves into a part of the networked world with high performance processors, see [TraubMaierBarbehön17]. Automotive control is a substantial part of the electronic systems and covers engine control, powertrain control, and vehicle control, as discussed in [KienckeNielsen05].

The focus of this dissertation is on powertrain control. The increase of electronics in cars enables to reduce undesired powertrain torsional oscillations by using intelligent control functions. These oscillations can be induced by changes of the desired steady-state driving torque and by disturbances, such as rolling resistance, since components of the powertrain are flexible, see [ErikssonNielsen14]. The vibrations are undesired due to the following three aspects. Firstly, performance of the vehicle is reduced, because energy is dissipated in the oscillations and the desired longitudinal acceleration of the car is

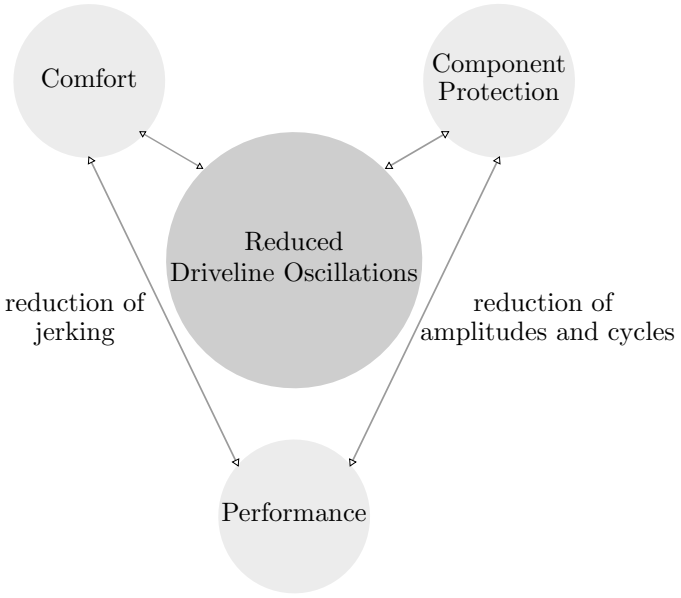

Figure 1.1: Multiple challenges of driveline oscillations

not reached. Secondly, driveline components are more stressed based on high oscillation amplitudes and cycles. And thirdly, driveline oscillations are uncomfortable for vehicle occupants. Hence, the overall objective is to achieve more performance, more comfort, and more component protection. This is challenging, since the objectives, as illustrated in Fig. 1.1, are already conflicted, see [PhamEtAl17]. For example, more comfort and more component protection can be easily achieved by reduction of performance. However, to keep or increase performance at the same time is much more challenging. Especially for sport cars, the high performance property is of crucial importance.

Model-based powertrain control undertakes tasks of the driver and attempts to accomplish all three goals in the best possible way by using a powertrain model. Thereby, the control units regulate actuators of the powertrain in such a way that driveline oscillations are compensated or even prevented. Typical actuators of the controller are the drive unit, as combustion engine or electric machine, and the gear clutch.

Powertrain control has the advantage that no physical changes of components are necessary. For example a typical mechanical approach is to increase the radius of a shaft in order to increase damping. However, such a change is often unrealizable due to cost and package space, as discussed in [EmadiLeeRajashekara08]. Moreover, powertrain control has the advantage that no weight is added. This advantage is crucial in the current discussion of consumption and emission reduction.

An further aspect is that the variety of vehicle types and variants explodes, see [CAR12]. Powertrain control, as a software solution, is much better suitable to overcome the rising complexity and variety of vehicles than mechanical solutions. Control is an easily adaptable method and can be applied to a wide range of powertrain types with minor or

no adjustments.

The design of powertrain control is challenging, when the effect of nonlinear dynamics are dominant in the powertrain. Nonlinear dynamics has to be considered in the design to avoid instability and performance degradation. Much research in recent years has focused on powertrain control with backlash, see for example [LagerbergEgardt05]. Backlash mostly occurs as the gap between two gear teeth and is necessary due to mounting reasons. The system dynamics is nonlinear when the backlash is traversed, since no torque is transmitted within the backlash gap, but torque is abruptly induced, when contact is achieved again. Due to this hard nonlinearity, driveline oscillations can be introduced and degrade the comfort of the system.

Another important role plays time delay in powertrain systems, as for instance investigated in [BaumannEtAl06]. A powertrain controller, which does not consider time delay, can destabilize the powertrain system, when the amount of time delay in the powertrain is significant. Time delay can origin from the physical behavior of the actuators in the powertrain or from electric delays due to signal processing and time sampling.

The described two dynamics of backlash and time delay in the powertrain system cannot be avoided, but influence the system behavior significantly and hence, lead to challenges in powertrain control design. These are in the focus of this work.

1.2 Literature Survey of Related Work

Powertrain control is an important field of research and there exists several works on this topic. This section gives an overview over recent works on powertrain control and includes related work to powertrain modeling, linear powertrain control, powertrain control with backlash, and powertrain control with focus on time delay. The survey of related work in this section lay the foundations for the next section, where the research gaps are discussed and the main contributions of this dissertation are stated.

The names powertrain and driveline are sometimes used as synonyms in literature. In order to prevent misunderstanding, a definition of powertrain and driveline, as used in [PhamEtAl17] and [KienckeNielsen05], is given here for the following. It is distinguished that powertrain includes the component drive unit (engine), while driveline does not include the drive unit. Therefore, for control the name powertrain is preferred in this work, since the drive units are used as actuators in the control systems. On the other hand, driveline oscillations is used here to describe the torsional oscillation of the whole system.

Powertrain Modeling

General studies on modeling of conventional powertrains, i.e. with combustion engine, can be found in [KienckeNielsen05], [DolciniWitBéchart10], and [ErikssonNielsen14]. These works investigate the dynamics of the powertrain as a multibody system and correspond equations of motion are given. In addition, a deep analysis of tire modeling is presented in [Pacejka12], which has to be included in the model, since the wheel-road contact is the last element of the powertrain. Further studies on the powertrain dynamics as a chain of oscillators are given in [SchrammHillerBardini10], [DresigRockhausenHolzweißig13], [DresigFidlin14], and [FischerEtAl16]. Eigenfrequencies and eigenforms are calculated and discussed in these works.

Discussion on the configuration of hybrid electric and battery electric powertrains are given for instance in [SciarrettaGuzzella07], [WallentowitzFreialdenhoven11], and [KhajepourFallahGoodarzi14]. More detailed hybrid electric powertrain models are presented in [AwadallahEtAl17], and [JauchEtAl18]. The electric machine is included in these models. Furthermore, a separation clutch is added, as shown in [JauchEtAl18]. This clutch allows to separate the internal combustion engine from the remaining powertrain.

Linear Powertrain Control

Simplified control models are used for control design. Control models with two lumped masses are described e.g. in [ErikssonNielsen14], [BaumannEtAl06], [BruceEgardtPettersson05] and [TemplinEgardt09]. Reduced control models with three lumped masses can be found in [VadamaluBeidl16], and [JauchEtAl18]. A comprehensive overview in feedback control of the powertrain is given in [ErikssonNielsen14]. Especially, feedback control of the steady-state is discussed in this book. Further studies can be found on powertrain control of load changes, gear shifting, and engine irregularity.

Control for load changes is for example investigated in [BaumannEtAl06]. A proportional-derivative controller is designed and parametrized by the root-locus method in order to reduce driveline oscillations. Furthermore, linear-quadratic regulators are for instance designed in [BruceEgardtPettersson05] and [TemplinEgardt09]. An approximate inverse plant model in combination with a filter is additionally designed in order to get reference trajectories for the linear-quadratic regulator in [BruceEgardtPettersson05]. The regulator in [TemplinEgardt09] is based on a reformulated system model, which allows control of zero steady-states.

Moreover, control for shifting is investigated, among others, in [PetterssonNielsen00], [RainerFrankDirk10], [JoachimReussHorwath09], and [GolkaniEtAl17]. In the research papers of [PetterssonNielsen00] and [JoachimReussHorwath09] the driveshaft torque and driveline oscillations are controlled to zero for gear shifting. Thereby, a proportional-integral-

derivative controller is applied in combination with an observer. In [RainerFrankDirk10] a feedforward controller is designed for shifting using the electric machine and clutch of a hybrid electric vehicle. In the work of [GolkaniEtAl17], a linear optimization problem is formulated to minimize additionally the energy losses in the clutches.

Studies on control of engine irregularity in a hybrid electric vehicle are for instance presented in [NjehCauetCoirault11], and [VadamaluBeidl16]. Both studies use the electric machine for control to compensate oscillations induced by the irregularity of a combustion engine. In [NjehCauetCoirault11] a linear parameter varying control strategy is designed, since the oscillation frequency varies with the rotation speed of the combustion engine. The control approach of [VadamaluBeidl16] involves a model predictive controller.

Powertrain Control with Backlash

An overview on powertrain control, which considers the dynamics of backlash explicitly, can be found in [Lagerberg01]. In this work over forty papers are reviewed and categorized by linear, passive and active nonlinear backlash control. Furthermore, the main backlash models are described and the various control methods are evaluated. Active controller tries to achieve fast contact mode, when the system is in backlash. These controllers are rated by the survey to have the most potential for achieving good system performance. In [Brogliato18] the control of backlash is analyzed in a tutorial from a mechanical point of view. There, dynamical equations of multibody systems with backlash are given as a Lagrangian system and various modeling examples are presented. Two control methods are reviewed, namely control with persistent contact and control with impacting trajectories.

Investigations on modeling of backlash can be found in various works, as for instance in [NordinGalic'Gutman97], [Lagerberg01], or [NordinGutman02]. In these works physical representations of backlash are derived, as well as simplified models for control. Moreover, observers are designed in [LagerbergEgardt07] and [Haschka MarkusVolker07] based on backlash models. [LagerbergEgardt07] applies a switching Kalman filter to estimate the offset parameters introduced by backlash. Thus, during backlash traversing a wait-mode is introduced. On the other hand, a nonlinear observer without switching is presented in [Haschka MarkusVolker07]. Thereby, backlash is separated in the observer model and this nonlinearity is handled as a nonlinear disturbance.

Advanced feedback controllers can be designed based on the knowledge of predicted system state. For instance, a switching controller is presented in [LagerbergEgardt05]. A state feedback controller is used in contact mode, but when the backlash gap has to be traversed, the control system switches to a model predictive controller, such that a fast backlash traversing is realized. A further optimization based controller is presented in [TemplinEgardt09]. There the backlash handling strategy introduces a torque hold level, such that the requested engine torque is limited, while the backlash is traversed. Moreover,

in [AngeringerHornReichhartinger12] and [Speidel17] sliding mode controllers are designed to control the nonlinear powertrain system with backlash. In [BoveeRizzoni16], a numerical model-based approach is presented. The driver's torque request is shaped by experiments such that the undesired effects of the nonlinear backlash dynamics are prevented.

Powertrain Control with Time Delay

There are numerous research interests in control of systems with time delay. A survey is given for instance in [Richard03]. In this work an overview of existing control approaches is provided and open problems regarding input delays, discrete implementation, and using knowledge about the delay in control design, are discussed. A further overview with focus on application is presented in [SipahiEtAl11]. Examples of systems with delays are given in the field of engineering, biology, physics, operations research, and economics. The limitations and potential advantages of delays are discussed and the limitations are illustrated using stability charts.

Deeper analysis on stability charts can be found for example in [Stépán89], [InspergerStépán11], and [HajduInsperger16]. These research investigate the construction of stability charts. In [Stépán89] stability analysis of delay-differential equations are focused and therefore, infinite-dimensional systems are considered. Semi-discretization, as a simplified alternative method for calculation of stability charts, is presented in [InspergerStépán11]. It uses numerical methods and derives finite-dimensional matrices for stability calculation. Furthermore, based on the derived methods in [Stépán89], the studies in [HajduInsperger16] analyze the robustness to model uncertainties of time delayed system controlled by a Smith predictor. Further studies on design of Smith predictors are given, besides [Smith57], for instance in [Palmor80] and [Normey-Rico07].

There exists few works on control of powertrains with time delay. Time delay can originate in the powertrain from combustion process of the engine and data acquisition from sensors, as described in [BaumannEtAl06]. In this work a Smith predictor is added to compensate the time delay. In [VadamaluBeidl16] dead time and time lag behavior of the actuator are considered. Dead time is compensated by a recursive prediction law and the lag behavior is modeled and included in a model predictive control scheme.

1.3 Contributions and Outline

In summary, there exist several different approaches to powertrain modeling and control. However, there are still many open questions, which are mostly relevant in high performance vehicles. In the following, these open areas are listed.

There exists a wide range of powertrain types due to electrification. However, so far most

work has concentrated on conventional powertrains. Also few researchers have investigated and compared the dynamics and control design of the main different powertrain types, conventional, hybrid electric, and battery electric, at once.

Furthermore, little work has been done on feedforward control design of load changes. A feedforward controller is favored since it complements a feedback controller to improve the tracking performance. In addition, it cannot destabilize the controlled system, as a feedback controller could do due to uncertainties. Especially, there exists a gap in feedforward control design which take the dynamics of backlash into account. Hence, an efficient feedforward control method is necessary that can be easily implemented in electronic control units.

Another aspect is that few work has focused on desired trajectory generation for load changes of powertrains with and without backlash. Desired trajectories are necessary to control the transient behavior of the system during load changes.

Moreover, the growing number of electronic control units makes it necessary to investigate the sources of time delay in powertrains and the destabilizing effect of it. The interaction between discrete implemented controllers and the continuous powertrain system has to be analyzed. If the system is destabilized by high time delays, compensation methods are needed. The combining of backlash and time delay in powertrain systems is a further area that has been hardly explored.

The main contributions of this thesis are the following:

- Detailed simulation models and control models of the powertrain are derived and analyzed for conventional, hybrid electric, and battery electric powertrains. Thereby, two-mass control models are given for conventional and battery electric powertrains, and a three-mass control model is given for hybrid electric powertrains. It is shown that the eigenvectors of the lowest dominant frequency of these powertrain types are similar. Results of these investigations are partly published in [PhamEtAl17].

- Flatness-based feedforward controllers are designed for two and three-mass control models in order to enable load changes with reduced driveline oscillations. This method is validated in experimental cars. Furthermore, the method is extended to powertrains with backlash by using a smooth backlash model. Desired trajectories are generated by the feedforward approaches and are applied for feedback control of the transient dynamics. Partial results are already published in [PhamBushnell15] and [PhamEtAl16]. Furthermore, parts of the approach are protected in patent [PhamScholzRoulet16].

- The powertrain with feedback and feedforward controller is considered as a digital control system. Stability regarding sampling time, actuator and measurement dead time is investigated. The compensation methods Smith predictor, observer based

method, and state prediction are designed and compared using stability diagrams. Partial results to this are published in [PhamScholzSeifried17].

- Finally, a fist ad hoc approach is derived, which combines the separately deduced control methods of backlash and time delay, such that control of these two effects at the same time is possible. The approach is evaluated in simulation.

The thesis is organized as follows. In Chapter 2, the torsion oscillation dynamics of conventional, hybrid electric, and battery electric powertrains is investigated, since this dynamics is relevant for powertrain control. First, detailed simulation models are derived as multibody systems for each powertrain type, then reduced control models are given and its eigenfrequencies and mode shapes are analyzed. The specifications of powertrain control in this work are defined in Chapter 3. Linear control methods, including flatness-based feedforward control and feedback control, are designed. Further, simulations and experimental results are provided. In Chapter 4, the linear control problem is extended by the nonlinear effects of backlash traversing and suitable control methods are derived. Chapter 5 focuses on the effect of time delay to powertrain control. The sources of time delay are discussed and different time delay compensation methods are presented. The methods are evaluated and compared using stability charts. In Chapter 6, the two effects of backlash and time delay are considered together. First results of an ad hoc approach are presented. Conclusions and an outlook for future work are given in Chapter 7.

Chapter 2

Driveline Oscillation Dynamics

In order to design control methods, which reduce driveline oscillations, knowledge of the longitudinal dynamics of powertrains is necessary. Therefore, modeling of powertrains is developed in this chapter. All three powertrain types namely conventional, hybrid electric, and battery electric are modeled here using multibody systems. First, a detailed multibody system model is used to demonstrate natural frequencies and mode shapes of the powertrain. Then, appropriate control models are derived from the detailed model by using knowledge of the mode shape. It is shown that two-mass and three-mass control models can represent the dominant torsion oscillation dynamics of all three powertrain types. In addition, the following chapters applies the detailed model to simulation studies in order to validate the developed designed control methods.

2.1 Modeling of Powertrains

There exists different types of powertrains depending on the applied drive unit or units. The most common type is the conventional powertrain, whereby an internal combustion engine powers the vehicle. Usually, a torsional damper, starting element and gearbox with several gears are also included. The torsional damper has the purpose to reduce rotational irregularity of the crankshaft and the clutch is used as a starting element, as well as to enable gear changes, see [DresigFidlin14].

For reasons related with the reduction of CO_2- and NO_x-emission, electrified vehicles are continuing to grow in importance. The first step of electrification are hybrid electrified vehicles with internal combustion engine and electric machine. The final stage of electrification are battery electrified vehicles. They are powered by one or several electric machines and use batteries to store energy. Particular benefits of electric vehicles are potentially zero CO_2- and NO_x-emission and the high energy efficiency of electric machines, as discussed in [KhajepourFallahGoodarzi14], and [ChanBouscayrolChen10].

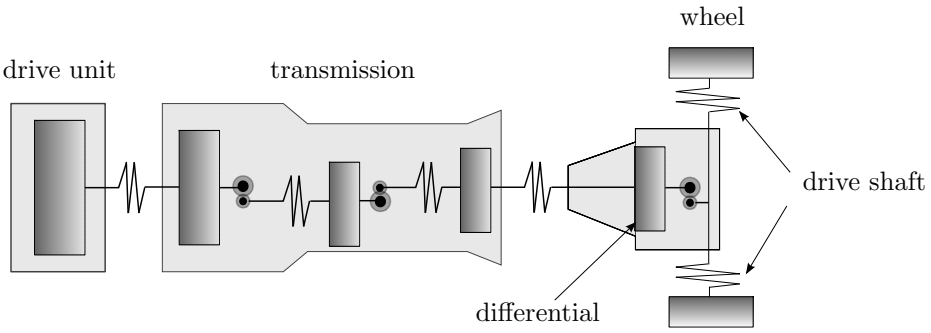

Figure 2.1: Generic powertrain of a conventional, hybrid electric or battery electric vehicle.

Furthermore, electric vehicles do not require a torsional damper, a starting element or many gears.

Besides the different drive technologies, general parts of all three powertrain types are drive unit, transmission with one or several gears, differential, drive shafts, and wheels. Another common aspect is that all three powertrain types can be modeled as a multibody system to analyze the rotational dynamic behavior of interconnected powertrain components, as described for instance in [FischerEtAl16], [ErikssonNielsen14], [DresigRockhausenHolzweißig13], [DolciniWitBéchart10], and [SchrammHillerBardini10]. In Fig. 2.1 a generic powertrain model is illustrated as a multibody system. The powertrain is divided into rigid bodies interconnected by spring-damper elements. Components such as drive unit, transmission, wheels, and vehicle body are represented by moments of inertia and mass, respectively. Flexible shafts and tires are represented by spring-damper elements. This structure allows rotational motion and in particular the representation of driveline oscillations. The rotational motion is caused by external torques of the drive unit, possible clutch, or brakes, as well as disturbances. Investigations on modeling disturbances, as wind and rolling resistance, can be found e.g. in [Gillespie92].

Spring-damper elements can be modeled linearly using Hooke's law or by nonlinear characteristics. Nonlinear characteristics are especially striking in the dynamics of torsional dampers and tires. A typical spring characteristic of a dual mass flywheel, as discussed in [FidlinSeebacher06], is illustrated in Fig. 2.2. The individual sections of the characteristic are linear.

The longitudinal tire force is a nonlinear function of wheel slip and normal load acting on the tire, see [Pacejka12]. In Fig. 2.2 the tire force characteristics is shown. The dynamics of the tire has a damping effect on the powertrain and the contact between tire and street converts the rotational motion of the wheels to a longitudinal of the vehicle. The dynamic behavior of the tire is nearly linear and stable for small tire slip.

The detailed simulation models apply the nonlinear characteristics of torsional damper and tires, whereby the control models apply the linear representations. In the following sections, detailed models of conventional, hybrid electric and battery electric powertrains

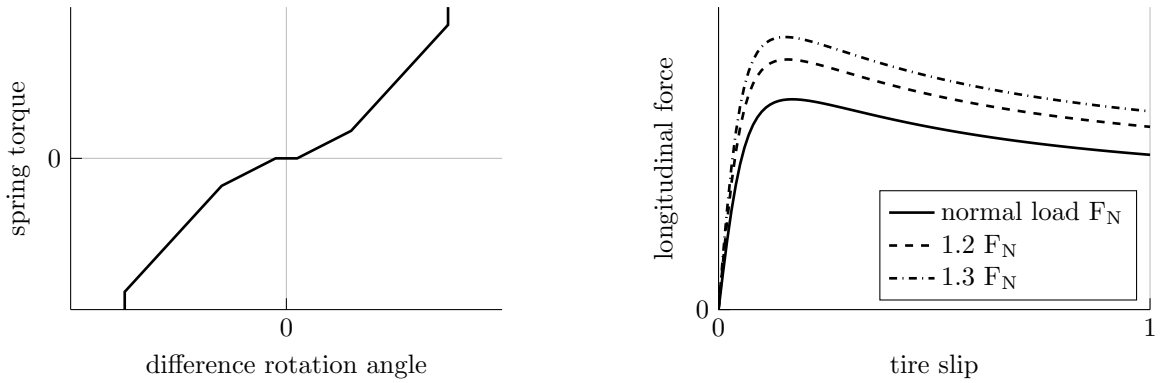

Figure 2.2: Nonlinear torque characteristics of a dual mass flywheel (left) and nonlinear tire force characteristics for various normal load (right).

are presented and the analysis of each specific vibration behavior is discussed.

2.2 Conventional Powertrains

In a conventional powertrain an internal combustion engine (ICE), such as a gasoline or diesel engine, drives the vehicle. Figure 2.3 shows schematically the torque characteristic of a gasoline engine. The pull characteristic illustrates that the idle speed of the engine is unequal to zero. For this reason a clutch or torque converter is necessary to separate the engine from the remaining powertrain, such that the vehicle can stand still, although the engine speed is unequal zero. In the further course of the work a clutch is considered. Furthermore, in order to take more advantages of the performance characteristic of the engine, different gears are required to shift the engine rotation speed in an area with maximal torque, see for instance [NaunheimerBertscheLechner07]. Therefore, in addition to the internal combustion engine, the clutch is another actuator in the powertrain. It controls the transmission of the torque which is built by the drive unit.

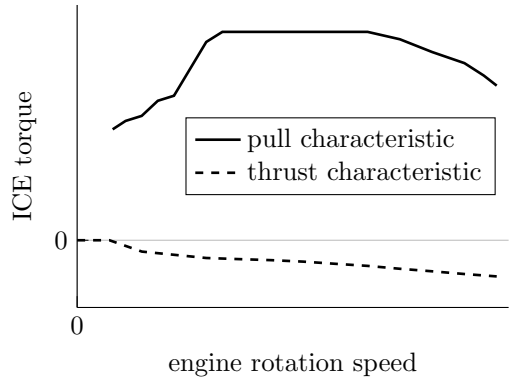

Figure 2.3: Characteristic curve of an internal combustion engine for pull and thrust.

2.2.1 Detailed Simulation Model

In this work the detailed rear-wheel drive powertrain model as configured in Fig. 2.4 is used to exemplary simulate oscillations caused by load changes or launching. The model consists of moments of inertia of internal combustion engine (ICE) J_1, torsional damper (TD) J_2, clutch J_3, transmission (TM) J_4, differential (DIFF) J_5, wheels $J_{6,7}$ and the vehicle mass m_{VEH}. Furthermore, the moments of inertia and vehicle mass are coupled by linear and nonlinear spring-damper elements $c_1, c_2, \ldots, c_{6,long}$ and $d_1, d_2, \ldots, d_{6,long}$. Nonlinear spring-damper elements are applied to the torsional damper and tires with characteristics as illustrated in Fig. 2.2. For reasons of clarity, damping parameters are not depicted in Fig. 2.4. The gear ratios R_{gear} and R_{DIFF} transform the rotation speeds to smaller velocities and the tire radius r_{tire} transform the rotary motions to a longitudinal. It is assumed that the internal combustion engine and the clutch can be directly actuated by the engine torque T_{ICE} and clutch torque T_{clutch}. The braking torques T_{brake} are set to zero and the disturbance force $F_{disturbance}$ is modeled as described in [Gillespie92].

The parameters of moments of inertia, mass, spring stiffness, gear ratios, and radius are listed in Tab. 2.1. Linearized stiffness parameters of the torsional damper and tires are also given. A damping coefficients d_i, with $i \in \{1, 2, \ldots, N\}$ where N is the degree of freedom of the system, depends on the stiffness c_i of the respective axis as discussed in [Schlecht09]. The damping coefficients for the detailed simulation model are approximated by $d_i \approx \gamma\sqrt{c_i}$ with $\gamma \in [0.0001, 0.001]$.

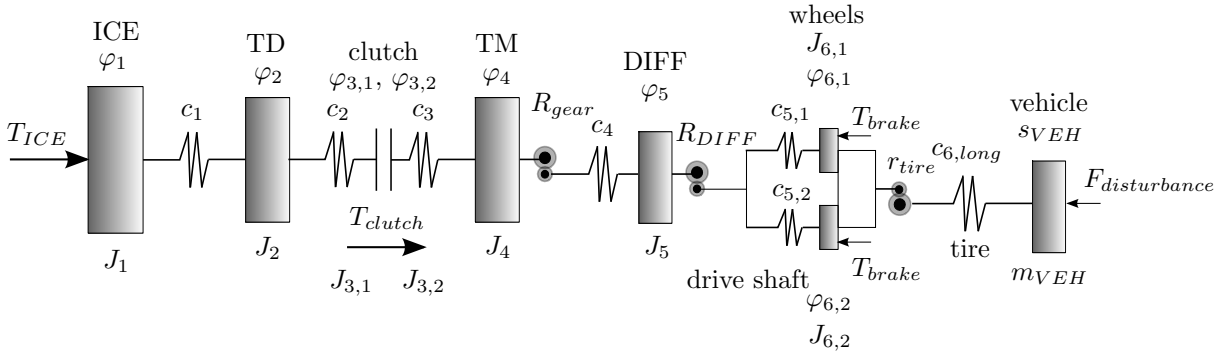

Figure 2.4: Detailed multibody model of a conventional powertrain.

2.2.2 Oscillation Analysis and Control Models

The dynamic behavior of a conventional powertrain during load change and launching is nearly linear, if the wheels are not slipping and the torsional damper is acting within the linear area of the spring characteristic. Therefore, the torsional vibration behavior can be investigated using modal analysis. The equations of motion have to be derived. States of

component	physical size	variable	value	unit
ICE	moment of inertia	J_1	0.3	kgm^2
TD	moment of inertia	J_2	0.05	kgm^2
clutch primary	moment of inertia	$J_{3,1}$	0.09	kgm^2
clutch secondary	moment of inertia	$J_{3,2}$	0.01	kgm^2
TM	moment of inertia	J_4	0.03	kgm^2
DIFF	moment of inertia	J_5	0.05	kgm^2
wheel left and right	moment of inertia	$J_{6,1}, J_{6,2}$	4	kgm^2
vehicle	mass	m_{VEH}	2000	kg
shaft ICE - TD linearized	stiffness	c_1	$2e3$	Nm/rad
shaft TD - clutch primary	stiffness	c_2	$5e4$	Nm/rad
shaft clutch secondary - TM	stiffness	c_3	$1e6$	Nm/rad
shaft TM - DIFF	stiffness	c_4	$1e6$	Nm/rad
drive shaft left and right	stiffness	$c_{5,1}, c_{5,2}$	$3.44e4$	Nm/rad
tire linearized	stiffness	$c_{6,long}$	$9.8e5$	N/m
gear	ratio 1st gear	R_{gear}	6	1
DIFF	ratio	R_{DIFF}	3	1
tire	radius	r_{tire}	0.35	m

Table 2.1: Parameters of the detailed simulation model of a conventional powertrain.

the system are rotation angles φ_i, angular velocities ω_i and displacement s_{VEH}, velocity v_{VEH} of each moment of inertia J_i, with $i \in \{1, 2, \ldots, N-1\}$ and vehicle mass m_{VEH}, respectively. Before the system equations are derived, simplifications are made.

First, gear ratios are incorporated. Figure 2.5 illustrates the transformation. A gear ratio R between two inertias J_k and J_l can be incorporated into

$$J_l = J_{l,R}R^2, \quad T_l = T_{l,R}R, \quad c = c_R R^2, \quad d = d_R R^2 \tag{2.1}$$

and

$$\varphi_l = \frac{\varphi_{l,R}}{R}, \quad \dot{\varphi}_l = \frac{\dot{\varphi}_{l,R}}{R}. \tag{2.2}$$

with new moment of inertia $J_{l,R}$, load torque $T_{l,R}$, damping d_R, and stiffness c_R and new states $\varphi_{l,R}$, and $\dot{\varphi}_{l,R}$ as described in [KienckeNielsen05], [DolciniWitBéchart10], and [PhamEtAl17].

Second, the total moment of inertia of the clutch is sum up with

$$J_3 = J_{3,1} + J_{3,2}. \tag{2.3}$$

Furthermore, left and right drive shafts and wheels are grouped together into

$$\begin{aligned} c_5 &= c_{5,1} + c_{5,2}, \\ d_5 &= d_{5,1} + d_{5,2}, \\ J_6 &= J_{6,1} + J_{6,2}. \end{aligned} \tag{2.4}$$

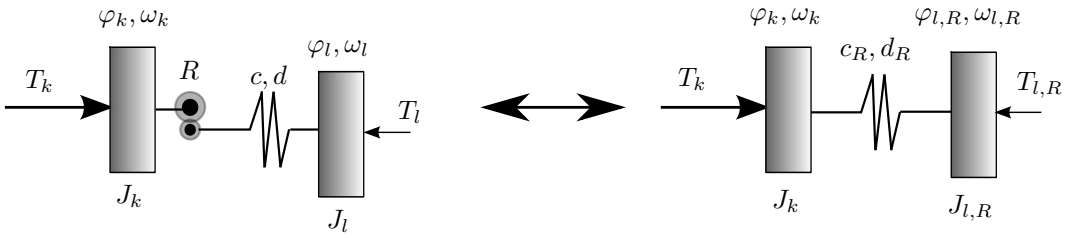

Figure 2.5: Incorporating gear ratio R into moment of inertia $J_{l,R}$, load torque $T_{l,R}$, damping d_R and spring stiffness c_R.

Third, the longitudinal motion of the vehicle mass m_{VEH} is transformed to a rotational equivalent. The tire radius r_{tire} is treated as a torque reducing gear ratio. Hence, the moment of inertia of the vehicle reads

$$J_7 = m_{VEH} r_{tire}^2, \tag{2.5}$$

stiffness and damping coefficients read

$$c_6 = c_{6,long} r_{tire}^2, \quad d_6 = d_{6,long} r_{tire}^2, \tag{2.6}$$

and the new rotational states are

$$\varphi_7 = \frac{s_{veh}}{r_{tire}}, \quad \omega_7 = \frac{v_{veh}}{r_{tire}}. \tag{2.7}$$

Applying these transformations, the conventional powertrain can be transformed to a chain of moments of inertia without explicit modeling gear ratios but by using transformed and summarized parameters as depicted in Fig. 2.6. Between moments of inertia four and five, as well es five and six, gear ratios are placed. Moreover, between moments of inertia six and seven the tire radius is located. The new state vector with rotation angle φ_i and angular velocity ω_i is

$$\boldsymbol{x}_{conv} = \left[\varphi_1, \varphi_2, \varphi_3, \varphi_4, \varphi_{5,R}, \varphi_{6,R}, \varphi_{7,R}, \omega_1, \omega_2, \omega_3, \omega_4, \omega_{5,R}, \omega_{6,R}, \omega_{7,R}\right]^T. \tag{2.8}$$

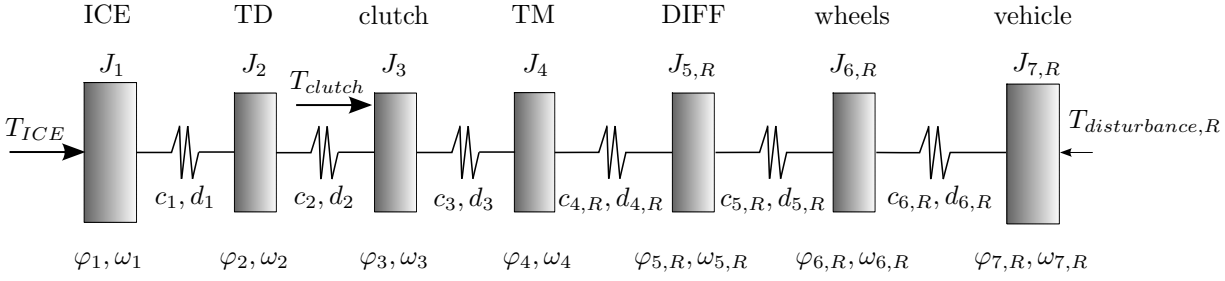

Figure 2.6: Conventional powertrain as a chain of inertias and spring-damper elements modeled with incorporated gear ratios.

The dynamic equation of the system in state space formulation is given by

$$\dot{\boldsymbol{x}}_{conv=} = \underbrace{\begin{pmatrix} 0 & \boldsymbol{I}_N \\ \boldsymbol{M}_{conv}^{-1}\boldsymbol{K}_{conv} & \boldsymbol{M}_{conv}^{-1}\boldsymbol{D}_{conv} \end{pmatrix}}_{=\boldsymbol{A}_{conv}} \boldsymbol{x}_{conv}, \tag{2.9}$$

The identity matrix $\boldsymbol{I}_N$ has size N which is the degree of freedom of the system. The stiffness matrix $\boldsymbol{K}_{conv}$ is tridiagonal and defined with transformed parameters as

$$\boldsymbol{K}_{conv} = \begin{pmatrix} -c_1 & c_1 & 0 & 0 & 0 & 0 & 0 \\ c_1 & -(c_1+c_2) & c_2 & 0 & 0 & 0 & 0 \\ 0 & c_2 & -(c_2+c_3) & c_3 & 0 & 0 & 0 \\ 0 & 0 & c_3 & -(c_3+c_{4,R}) & c_{4,R} & 0 & 0 \\ 0 & 0 & 0 & c_{4,R} & -(c_{4,R}+c_{5,R}) & c_{5,R} & 0 \\ 0 & 0 & 0 & 0 & c_{5,R} & -(c_{5,R}+c_{6,R}) & c_{6,R} \\ 0 & 0 & 0 & 0 & 0 & c_{6,R} & -c_{6,R} \end{pmatrix}. \tag{2.10}$$

The damping matrix $\boldsymbol{D}_{conv}$ has the same structure as $\boldsymbol{K}_{conv}$, but using damping constants d_i instead of stiffness constants c_i. The mass matrix $\boldsymbol{M}_{conv}$ is given by the diagonal matrix

$$\boldsymbol{M}_{conv} = \begin{pmatrix} J_1 & 0 & 0 & 0 & 0 & 0 & 0 \\ 0 & J_2 & 0 & 0 & 0 & 0 & 0 \\ 0 & 0 & J_3 & 0 & 0 & 0 & 0 \\ 0 & 0 & 0 & J_4 & 0 & 0 & 0 \\ 0 & 0 & 0 & 0 & J_{5,R} & 0 & 0 \\ 0 & 0 & 0 & 0 & 0 & J_{6,R} & 0 \\ 0 & 0 & 0 & 0 & 0 & 0 & J_{7,R} \end{pmatrix} \tag{2.11}$$

with moments of inertia J_i and $J_{i,R}$, respectively, with $i \in \{1, 2, \ldots, 7\}$ as diagonal elements.

Hence, the natural frequency and eigenmode of the conventional powertrain can be calculated with system matrix $\boldsymbol{A}_{conv}$ defined in (2.9). For the sake of simplicity, the damping matrix $\boldsymbol{D}_{conv}$ is set to zero, since powertrains are underdamped systems and the impact of damping to natural frequency and eigenmode is very small and for instance describe in [MagnusPoppSextro13].

Remark

Equation (2.1) clearly shows that a gear ratio R reduces the stiffness and damping of the system by the factor of $\frac{1}{R^2}$ as discussed in [FischerEtAl16]. Additional gear ratios in the system increase this effect and further reduce stiffness and damping. The consequences are high amplitude and long decay time, when the system is stimulated by impulsive load changes or periodical suggestion as discussed in [PhamEtAl17].

2.2.2.1 Closed Clutch

Usually during driving, the clutch is closed and the whole powertrain is connected. For this condition, the vibrational behavior of the whole conventional powertrain model is investigated. The natural frequency and eigenmode of the vibrations are calculated by analyzing system matrix $\boldsymbol{A}_{conv}$ given in (2.9). The system is parameterized by the values given in Tab. 2.1 and zero damping coefficients. The system state $\boldsymbol{x}_{conv}$ is defined in (2.8). The resulting natural frequencies are

$$\begin{aligned} &f_0 = 0\ Hz, \quad &&f_1 = 2.6\ Hz, \quad &&f_2 = 21.1\ Hz, \quad &&f_3 = 31.5\ Hz, \\ &f_4 = 188.7\ Hz, \quad &&f_5 = 706.6\ Hz, \quad &&f_6 = 1064.6\ Hz \end{aligned} \tag{2.12}$$

with f_0 as the frequency of the rigid body mode. The dominant frequency can be investigated by simulation of a load change. Figure 2.7 shows the system, which is excited by the torque ramp T_{ICE}. The vibrational behavior of engine angular velocity ω_{ICE}, wheel angular velocity multiplied by the total gear ratio $\omega_{wheel}R_{total}$, and longitudinal vehicle acceleration a_{VEH} is depicted. The total gear ratio of gearbox and differential is given as $R_{total} = R_{gear}R_{DIFF}$. The low frequency f_1 with 2.6 Hz appears clearly, especially in the longitudinal acceleration of the vehicle. The other frequencies are hardly noticeable.

Furthermore, the eigenvector of the dominant frequency f_1 is calculated to analyze the deflection shape. According to Fig. 2.8 on the left, the corresponding eigenvector shows that moments of inertia of internal combustion engine, torsional damper, clutch, transmission, and differential vibrate synchronous. However, wheels and vehicle vibrate out of phase to the other inertias. This out-of-phase oscillation can also be seen in Fig. 2.7 between angular velocity of internal combustion engine ω_{ICE} and wheels multiplied by the total

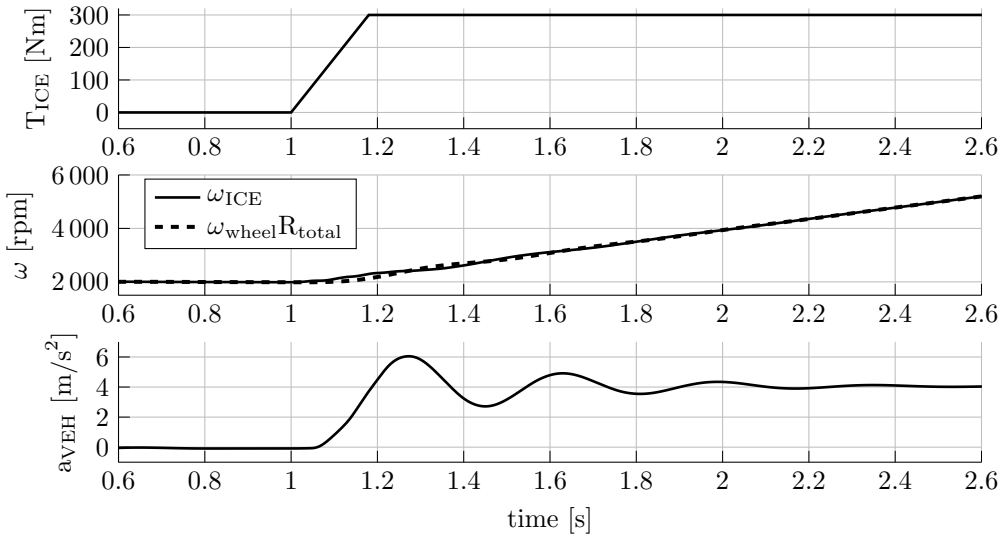

Figure 2.7: Simulation a load change with the detailed conventional powertrain model with closed clutch. The system is excited by the torque ramp T_{ICE}.

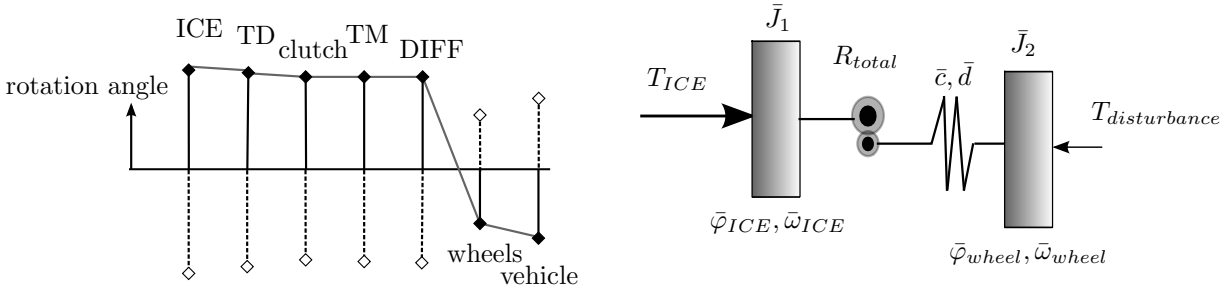

Figure 2.8: Eigenvector of the dominant frequency f_1 (left) and two-mass control model (right) of a conventional powertrain with closed clutch.

gear ratio $\omega_{wheel} R_{total}$.

Using this knowledge of the dominant eigenmode, a control model with two inertias and one spring-damper element as shown in Fig. 2.8 (right) is deduced to represent this vibration behavior. Similar control models of conventional powertrains can be found in [GrotjahnQuernheimZemke06] and [ErikssonNielsen14]. The equations of motion of the two-mass control model are

$$\begin{aligned}
\dot{\bar{\varphi}}_{ICE} &= \bar{\omega}_{ICE}, \\
\dot{\bar{\varphi}}_{wheel} &= \bar{\omega}_{wheel}, \\
\bar{J}_1 \dot{\bar{\omega}}_{ICE} &= -\frac{1}{R_{total}} \bar{c} \left(\frac{1}{R_{total}} \bar{\varphi}_{ICE} - \bar{\varphi}_{wheel} \right) - \frac{1}{R_{total}} \bar{d} \left(\frac{1}{R_{total}} \bar{\omega}_{ICE} - \bar{\omega}_{wheel} \right) + T_{ICE}, \\
\bar{J}_2 \dot{\bar{\omega}}_{wheel} &= \bar{c} \left(\frac{1}{R_{total}} \bar{\varphi}_{ICE} - \bar{\varphi}_{wheel} \right) + \bar{d} \left(\frac{1}{R_{total}} \bar{\omega}_{ICE} - \bar{\omega}_{wheel} \right) - T_{disturbance}.
\end{aligned} \tag{2.13}$$

In the following, states and parameters of control models are denoted with a bar. The states are rotation angle and angular velocity of the internal combustion engine $\bar{\varphi}_{ICE}, \bar{\omega}_{ICE}$, and rotation angle and angular velocity of the wheel $\bar{\varphi}_{wheel}, \bar{\omega}_{wheel}$. The parameters of this model can be approximated by the parameters of the detailed model from Tab. 2.1 by

$$\begin{aligned}
\bar{J}_1 &= J_1 + J_2 + J_3 + J_4 + \frac{1}{R_{gear}^2} J_5, \\
\bar{J}_2 &= J_6 + m_{VEH} r_{tire}^2, \\
\bar{c} &= c_5, \\
\bar{R}_{total} &= R_{gear} R_{DIFF},
\end{aligned} \tag{2.14}$$

with stiffness c_5 from (2.4).

The largest displacement is the difference between the rotation angles of differential and wheels, see Fig. 2.8, which corresponds to the drive shafts. Therefore the stiffness parameter of the control model is estimated by these drive shaft stiffnesses. The damping factor

$\bar{d}$ of the control system has to represent damping of the drive shaft as well as damping resulting from the tires. Hence, it is $\bar{d} \gg d_{driveshaft}$. The value of $\bar{d}$ is approximated such that the amplitudes of the control model corresponds to the amplitudes of the general model. The parameters of the control model are summarized in Tab. 2.2. Besides this

$\bar{J}_1$	0.481	kgm^2
$\bar{J}_2$	249	kgm^2
$\bar{c}$	3.44e4	Nm/rad
$\bar{d}$	350	Nms/rad
R_{total}	18	1

Table 2.2: Parameters of the control model of a conventional powertrain with closed clutch.

simple estimation, optimization techniques can be applied to get even better agreement between control model and detailed simulation model if necessary.

Finally, a load change is simulated by the detailed model as well as the derived control model. The simulation results are shown in Fig. 2.9. The system is excited in the first row by the torque ramp T_{ICE}. System responses are shown below. Good agreement between state $\omega_{ICE}, \omega_{wheel}$ and vehicle acceleration a_{VEH} of detailed simulation model and control model can be observed. Thereby, the vehicle acceleration $\bar{a}_{VEH}$ of the control model is defined as

$$\bar{a}_{VEH} = \dot{\bar{\omega}}_{wheel} r_{tire}. \tag{2.15}$$

Further adjustments of the control parameters are not necessary.

2.2.2.2 Open Clutch - Launching

In a conventional powertrain the clutch is open at the beginning of launching or gear shifting. In this case internal combustion engine, torsional damper and primary clutch are not coupled with the remaining powertrain. Therefore, the vibration behavior of a conventional powertrain with open clutch has to be analyzed additionally.

Figure 2.10 shows the reduced powertrain, when the first two moments of inertia and the primary clutch are not coupled. Thus, only the elements clutch secondary, transmission TM, differential $DIFF$, wheels, and vehicle are included. System state $\boldsymbol{x}_{conv,red}$, stiffness matrix $\boldsymbol{K}_{conv,red}$, and mass matrix $\boldsymbol{M}_{conv,red}$ are reduced to

$$\boldsymbol{x}_{conv,red} = \left[\varphi_3, \varphi_4, \varphi_{5,R}, \varphi_{6,R}, \varphi_{7,R}, \omega_1, \omega_2, \omega_3, \omega_4, \omega_{5,R}, \omega_{6,R}, \omega_{7,R}\right]^T, \tag{2.16}$$

$$\boldsymbol{K}_{conv,red} = \begin{pmatrix} -c_3 & c_3 & 0 & 0 & 0 \\ c_3 & -(c_3 + c_{4,R}) & c_{4,R} & 0 & 0 \\ 0 & c_{4,R} & -(c_{4,R} + c_{5,R}) & c_{5,R} & 0 \\ 0 & 0 & c_{5,R} & -(c_{5,R} + c_{6,R}) & c_{6,R} \\ 0 & 0 & 0 & c_{6,R} & -c_{6,R} \end{pmatrix}, \tag{2.17}$$

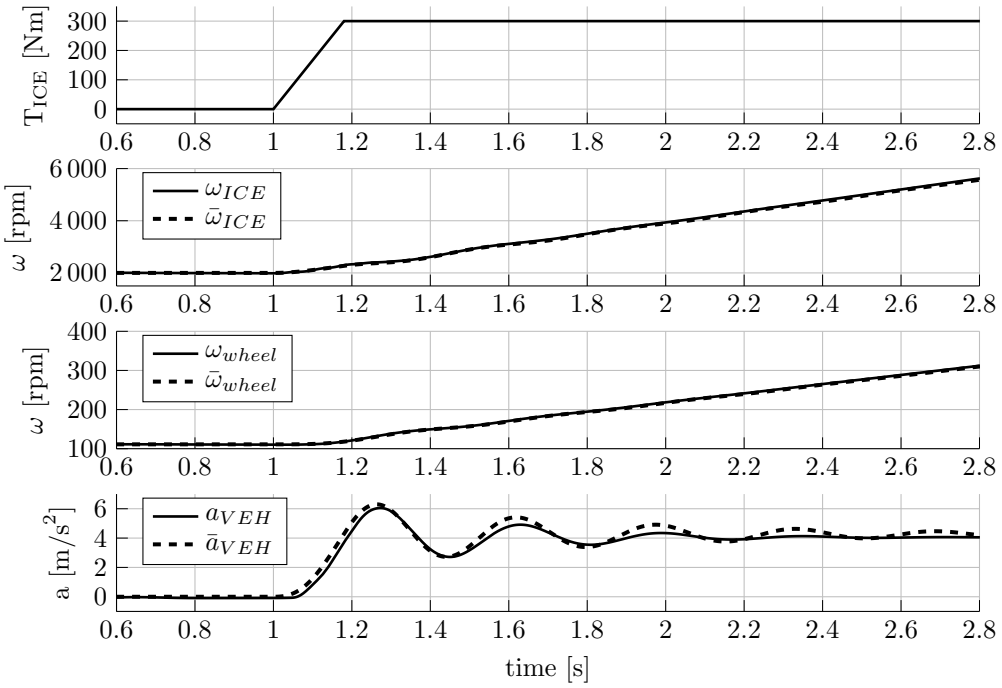

Figure 2.9: Simulation of a load change with closed clutch by general and control model. States of the control model are marked with a bar.

$$\boldsymbol{M}_{conv,red} = \begin{pmatrix} J_{3,2} & 0 & 0 & 0 & 0 \\ 0 & J_4 & 0 & 0 & 0 \\ 0 & 0 & J_{5,R} & 0 & 0 \\ 0 & 0 & 0 & J_{6,R} & 0 \\ 0 & 0 & 0 & 0 & J_{7,R} \end{pmatrix}. \tag{2.18}$$

The damping matrix $\boldsymbol{D}_{conv,red}$ has again the same structure as $\boldsymbol{K}_{conv,red}$, where damping constants instead of stiffness constants are used, see (2.9). In order to investigate the vibration behavior with open clutch, natural frequencies and eigenvectors of the reduced

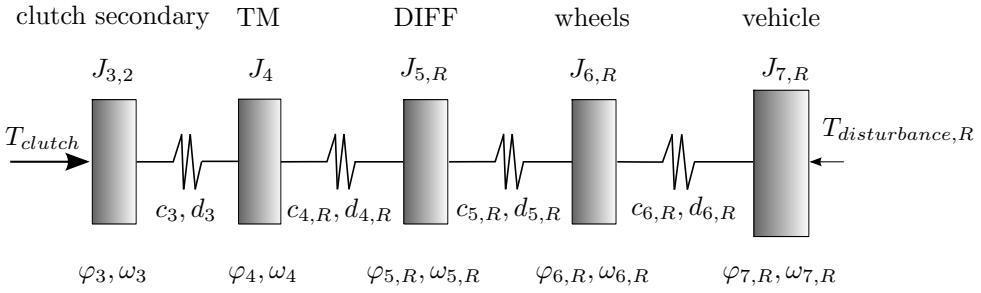

Figure 2.10: Conventional powertrain with open clutch to analyze vibration behavior of launching.

system matrix $\boldsymbol{A}_{conv,red}$ are evaluated, with

$$\boldsymbol{A}_{conv,red} = \begin{pmatrix} 0 & \boldsymbol{I}_{N-2} \\ \boldsymbol{M}_{conv,red}^{-1}\boldsymbol{K}_{conv,red} & \boldsymbol{M}_{conv,red}^{-1}\boldsymbol{D}_{conv,red} \end{pmatrix}. \tag{2.19}$$

The identity matrix $\boldsymbol{I}_{N-2}$ has the reduced size $N-2$, since two degrees of freedom are omitted due to the open clutch.

Applying the parameters summarized in Tab. 2.1, the resulting frequencies with zero damping matrix are

$$\begin{aligned} &f_0 = 0\ Hz, \qquad f_1 = 7.3\ Hz, \qquad f_2 = 31.6Hz, \\ &f_3 = 724.6\ Hz, \quad f_4 = 1839.6\ Hz. \end{aligned} \tag{2.20}$$

Figure 2.11 shows a simulated race start, which is an agile launching. At the beginning the clutch is open and the engine is driven to a large initial speed value $\omega_{ICE,0} = 5000\ rpm$ by the engine torque T_{ICE}. As the clutch is open, the angular velocity of input shaft ω_{IS} and wheel ω_{wheel} are zero. At time $t = 1.5\ s$ the clutch is closed by a torque ramp T_{clutch}. The reference clutch torque $T_{clutch,REF}$ is shown in the figure. Simultaneously, the torque of the internal combustion T_{ICE} is increased to the desired maximum torque 350 Nm. When the clutch is completely closed, when the angular velocity of the input shaft ω_{IS} is synchronized with the angular velocity of the internal combustion engine ω_{ICE} at $t = 2.65$. Furthermore, the dominant natural frequency f_1 is during launching at 7.3 Hz and can be seen in the vehicle acceleration a_{VEH} between 1.5 s to 2.65 s. After the clutch is closed, the frequency of the vehicle acceleration a_{VEH} is smaller and corresponds to the dominant natural frequency for closed clutch with 2.6 Hz.

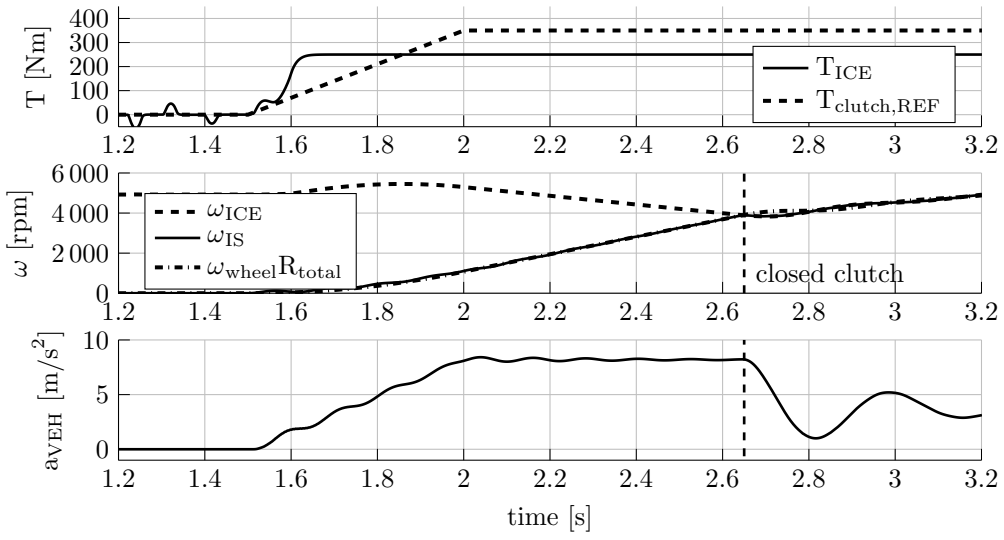

Figure 2.11: Simulation of launching of a conventional powertrain. The general model is parameterized by values in Tab. 2.1.

As in the case with closed clutch, only the low frequency f_1 is dominant. Therefore, the corresponding eigenmode of f_1 is calculated and is depicted in Fig. 2.12. The deflection shape shows the largest displacement between differential and wheels, similar to the case with closed clutch, see Fig. 2.8. After the clutch is closed, the eigenmode shown in Fig. 2.8 appears. A similar control model as for closed clutch can be applied for launching. The control model with two-degrees of freedom is shown in Fig. 2.12 on the right. The corresponding equations of motion for open clutch read

$$\begin{aligned}
\dot{\bar{\varphi}}_{IS} &= \bar{\omega}_{IS}, \\
\dot{\bar{\varphi}}_{wheel} &= \bar{\omega}_{wheel}, \\
\bar{J}_1\dot{\bar{\omega}}_{IS} &= -\frac{1}{R_{total}}\bar{c}\left(\frac{1}{R_{total}}\bar{\varphi}_{IS} - \bar{\varphi}_{wheel}\right) - \frac{1}{R_{total}}\bar{d}\left(\frac{1}{R_{total}}\bar{\omega}_{IS} - \bar{\omega}_{wheel}\right) + T_{clutch}, \\
\bar{J}_2\dot{\bar{\omega}}_{wheel} &= \bar{c}\left(\frac{1}{R_{total}}\bar{\varphi}_{IS} - \bar{\varphi}_{wheel}\right) + \bar{d}\left(\frac{1}{R_{total}}\bar{\omega}_{IS} - \bar{\omega}_{wheel}\right) - T_{disturbance}.
\end{aligned} \tag{2.21}$$

As in (2.13) states and parameters of the control model are denoted with a bar. The states of the open clutch system are rotation angle and angular velocity of the input shaft $\bar{\varphi}_{IS}, \bar{\omega}_{IS}$, and rotation angle and angular velocity of the wheel $\bar{\varphi}_{wheel}, \bar{\omega}_{wheel}$. The parameters can be approximated by

$$\begin{aligned}
\bar{J}_1 &= J_{3,2} + J_4 + \frac{1}{R_{gear}^2}J_5, \\
\bar{J}_2 &= J_6 + m_{veh}r_{tire}^2, \\
\bar{c} &= c_5, \\
\bar{R}_{total} &= R_{gear}R_{DIFF},
\end{aligned} \tag{2.22}$$

with values from Tab. 2.1 and stiffness c_5 from (2.4). Table 2.3 presents the resulting parameters.

Launching is simulated by the detailed simulation model and derived control model in

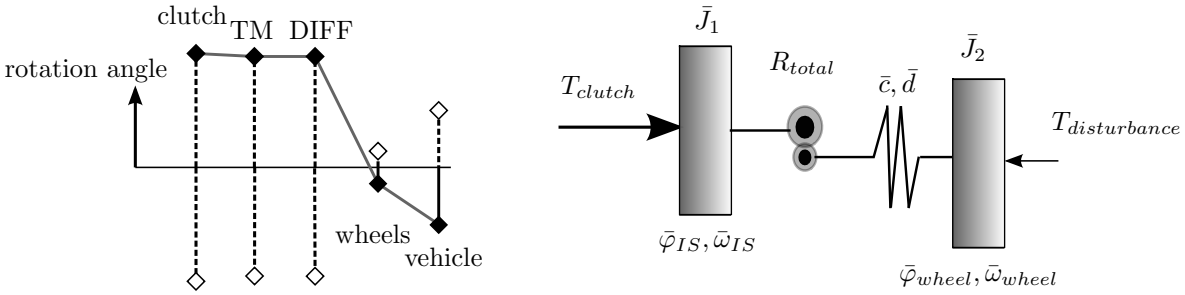

Figure 2.12: Eigenvector of the dominant frequency 7.3 Hz (left) and two-mass control model (right) of a conventional powertrain with open clutch.

Fig. 2.13. As the clutch is open, general and control model show good agreement. The dominant frequency 7.3 Hz can be simulated by the control model during open clutch. When the clutch is closed, the first eigenfrequency of the detailed simulation model is reduced and switching to the control model for closed clutch would be appropriate.

$\bar{J}_1$	0.0414	kgm^2
$\bar{J}_2$	249	kgm^2
$\bar{c}$	3.44e4	Nm/rad
$\bar{d}$	50	Nms/rad
$\bar{R}_{total}$	18	1

Table 2.3: Parameters of the control model of a conventional powertrain with open clutch.

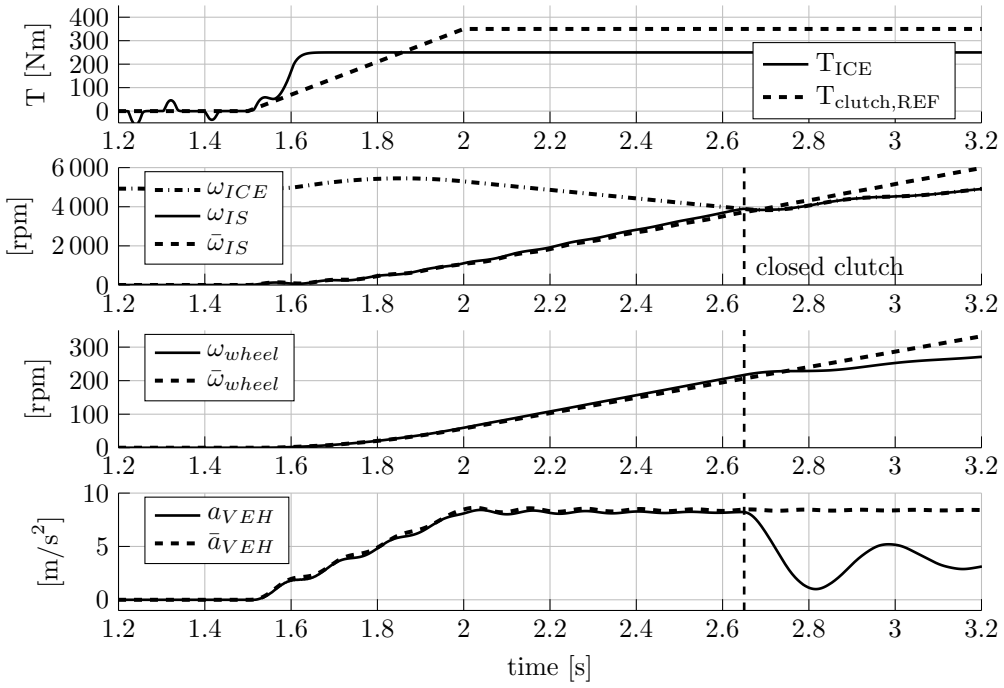

Figure 2.13: Simulation of launching with open clutch by general and control model. States of the control model are marked with a bar.

2.3 Hybrid Electric Vehicles

The main difference between conventional and hybrid electric powertrains is that the latter one has an electric machine (EM) as an additional drive unit. The electric machine is powered by a battery, which can be charged by the combustion engine or by recuperation during braking. In the particular case of a plug-in hybrid electric vehicle (PHEV), the battery can additionally be charged from an external electrical power source.

Combustion engine and electric machine can be arranged in four different main hybrid architectures, namely parallel hybrid, series hybrid, split axle hybrid, and power split hybrid as illustrated in Fig. 2.14 and described in [Kirchner07], [SciarrettaGuzzella07], and [ErikssonNielsen14]. The power of internal combustion engine and electric machine can be added in parallel hybrid electric vehicles, as the internal combustion engine is mechanically coupled with the electric machine. In series hybrid electric vehicles the internal combustion engine is not mechanically coupled with the remaining powertrain. The internal combustion engine drives a generator, which supply energy for the battery and the electric machine. Further, power split hybrid electric vehicles are similar to series hybrid electric vehicles, but the internal combustion engine can also drive the powertrain directly. In a split axle hybrid electric vehicle, each drive unit, internal combustion engine and electric machine, drives each axis separately.

Usually, parallel systems are more efficient than other configurations as described in [Pistoia10] and thus are common. The parallel architecture allows the vehicle to drive in pure combustion engine mode, pure electric machine mode or in a combined mode of combustion engine and electric machine, see [KumPengBucknor11]. A separation clutch or a freewheel enables switching between these modes. In the following parallel hybrid electric vehicles are investigated.

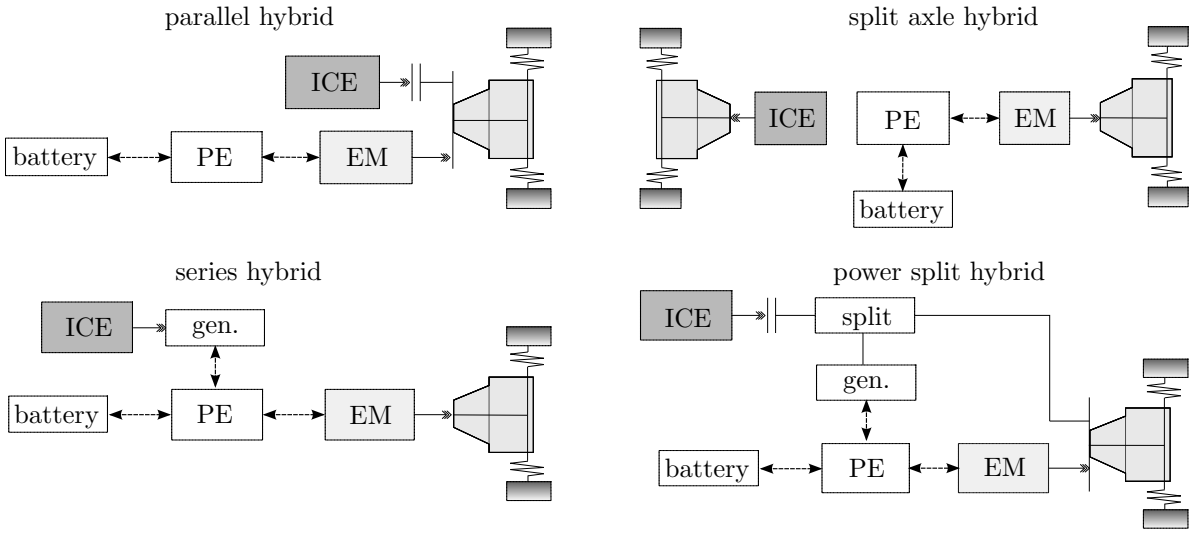

Figure 2.14: Main architectures of hybrid electric vehicles with power electronics (PE) as described in [ErikssonNielsen14].

2.3.1 Detailed Simulation Model

The torsional oscillation behavior of a rear-wheel drive parallel hybrid electric vehicle as shown in Fig. 2.15 is analyzed. Compared to the conventional powertrain, shown in Fig. 2.4, an electric machine (EM), separation clutch, battery, and power electronics (PE) are added. The drive torque of the combustion engine T_{ICE} and of the electric machine T_{EM} can act on the system. Battery management and operating strategy are not investigated, since driveline oscillations are focused.

Furthermore, unlike with conventional powertrains, parallel hybrid electric powertrains can consist of two clutches, namely a separation and a gear clutch. The task of a gear clutch with torque $T_{gear,clutch}$ in hybrid electric vehicles is similar to those in conventional. However, a separation clutch has the task to couple or decouple the internal combustion engine from the remaining powertrain with clutch torque $T_{sep,clutch}$. When the separation clutch is open, the electric machine is solely responsible for the drive. This powertrain configuration is similar to a conventional powertrain, since there is only one drive unit available and the remaining powertrain is equal. In the case of closed clutch there are two larger moments of inertia in the front part of the powertrain and two drive units can act on the system simultaneously. Thus, the system dynamics is new and this case with closed separation and gear clutch has to be studied, therefore the clutch torques $T_{sep,clutch}, T_{gear,clutch}$, as external actuators, are not further considered.

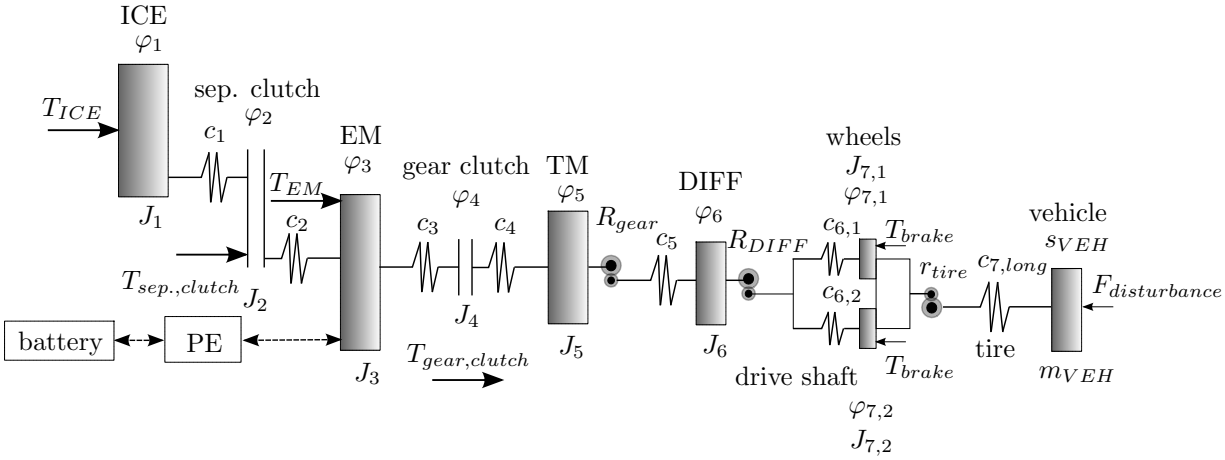

Figure 2.15: Detailed multibody model of a parallel hybrid electric powertrain.

2.3.2 Oscillation Analysis and Control Model

The parallel hybrid electric powertrain shown in Fig. 2.15 is parameterized with values summarized in Tab. 2.4.

component	physical size	variable	value	unit
ICE	moment of inertia	J_1	0.3	kgm^2
separation clutch	moment of inertia	J_2	0.02	kgm^2
EM	moment of inertia	J_3	0.1	kgm^2
gear clutch	moment of inertia	J_4	0.1	kgm^2
TM	moment of inertia	J_5	0.03	kgm^2
DIFF	moment of inertia	J_6	0.05	kgm^2
wheel left and right	moment of inertia	$J_{7,1}, J_{7,2}$	4	kgm^2
vehicle	mass	m_{VEH}	2000	kg
shaft ICE - separation clutch	stiffness	c_1	$4.5e3$	Nm/rad
shaft separation clutch - EM	stiffness	c_2	$1e6$	Nm/rad
shaft EM - gear clutch	stiffness	c_3	$1e6$	Nm/rad
shaft gear clutch - TM	stiffness	c_4	$1e6$	Nm/rad
shaft TM - DIFF	stiffness	c_5	$1e6$	Nm/rad
drive shaft left and right	stiffness	$c_{6,1}, c_{6,2}$	$3.44e4$	Nm/rad
tire linearized	stiffness	$c_{7,long}$	$9.8e5$	Nm/rad
gear	ratio 2nd gear	R_{gear}	2.5	1
DIFF	ratio	R_{DIFF}	4	1
tire	radius	r_{tire}	0.35	m

Table 2.4: Parameters of the general model of a hybrid electric powertrain.

As shown for conventional powertrains in (2.1)-(2.7) reformulations are done. Gear ratios are incorporated in system parameters $c_{5,R}, d_{5,R}, J_{6,R}, \varphi_{6,R}, \omega_{6,R}, \ldots, J_{8,R}$. Furthermore, moment of inertias of the wheels, and stiffness and damping of the drive shafts are sum up. The longitudinal motion s_{VEH}, v_{VEH} of the vehicle is converted to a rotational motion $\varphi_{8,R}, \omega_{8,R}$.

According to conventional powertrains the natural frequencies and eigenvectors are calculated. Two new states φ_3, ω_3 have to be added to the system state vector due to the electric machine and thus the system order of a parallel hybrid electric powertrain is greater than of a conventional powertrain. The new state vector reads

$$\boldsymbol{x}_{PHEV} = \left[\varphi_1, \varphi_2, \varphi_3, \varphi_4, \varphi_5, \varphi_{6,R}, \varphi_{7,R}, \varphi_{8,R}, \omega_1, \omega_2, \omega_3, \omega_4, \omega_5, \omega_{6,R}, \omega_{7,R}, \omega_{8,R}\right]^T . \quad (2.23)$$

with states shown in Fig. 2.16.

The resulting 8 natural frequencies are

$$\begin{aligned} &f_0 = 0\ Hz, && f_1 = 3.8\ Hz, && f_2 = 28.7\ Hz, && f_3 = 31.9Hz, \\ &f_4 = 602.6\ Hz, && f_5 = 1076.7\ Hz, && f_6 = 1261.5\ Hz, && f_7 = 2876.4\ Hz. \end{aligned} \quad (2.24)$$

A load change simulation by the detailed hybrid model is given in Fig. 2.17. Hereby, both engine torque T_{ICE} and electric machine torque T_{EM} are changed from 0 to 250 Nm. The

angular velocities $\omega_{ICE}, \omega_{EM}, \omega_{wheel}$ and the vehicle longitudinal acceleration a_{VEH} show the dominant low frequency f_1 from Eq. (2.24).

In order to synthesize a control model, the first two essential eigenmodes of the system are calculated. Figure 2.18 shows the dominant eigenvectors of f_1 and f_2. The lowest eigenmode of the hybrid powertrain is comparable to the lowest mode of the conventional powertrain, see Fig. 2.8. For the parallel hybrid electric vehicle, a two-mass control model is not sufficient as there exist two inputs T_{ICE}, T_{EM}, which have to be considered in control model design. Therefore, the knowledge about the second eigenmode is used to deduce a three-mass control model as shown in Fig. 2.19. The first mass of inertia $\bar{J}_1$ represents the combustion engine, the second mass of inertia $\bar{J}_2$ represents electric machine to differential and the third mass of inertia $\bar{J}_3$ represents the vehicle mass.

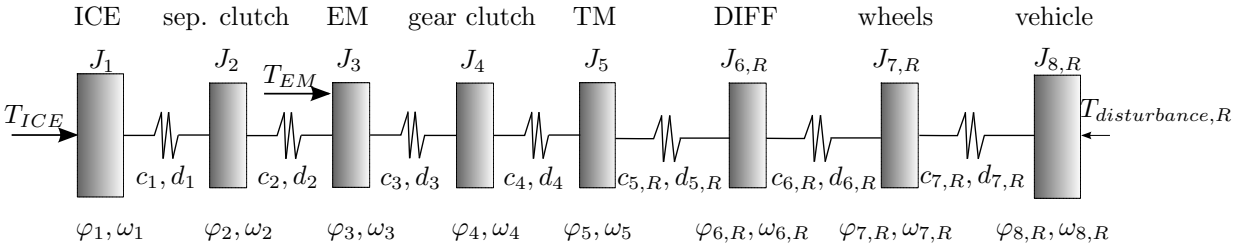

Figure 2.16: Parallel hybrid electric powertrain as a chain of inertias and spring-damper elements modeled with incorporated gear ratios.

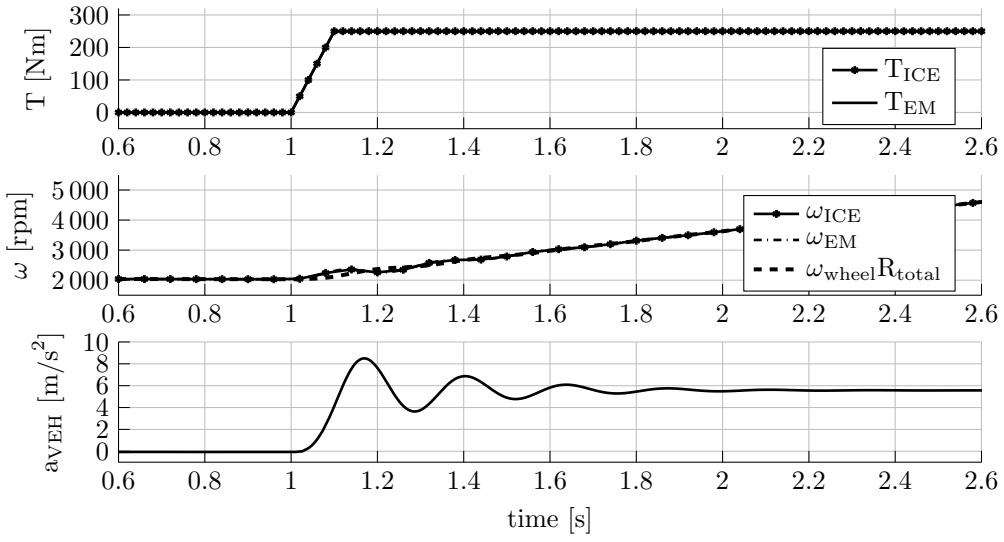

Figure 2.17: Simulation of a load change of internal combustion engine T_{ICE} and electric machine T_{EM} with detailed powertrain model as shown in Fig. 2.15.

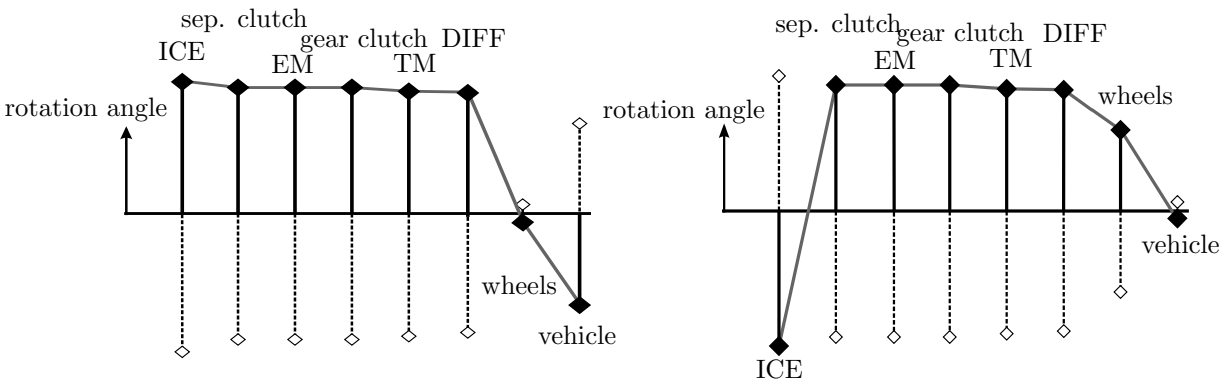

Figure 2.18: First eigenvector of the frequency f_1 (left) and second eigenvector of the frequency f_2 (right) of a parallel hybrid electric powertrain with closed separation and gear clutch.

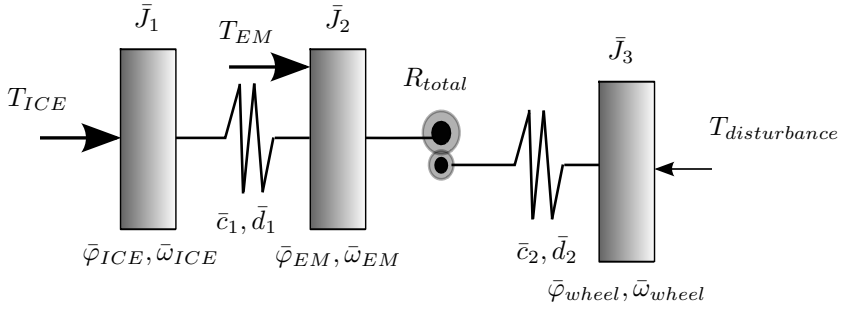

Figure 2.19: Three-mass control model of a hybrid electric powertrain with input T_{ICE} and T_{EM}.

The dynamic equations of the control model with three-degrees of freedom read

$$
\begin{aligned}
\dot{\bar{\varphi}}_{ICE} &= \bar{\omega}_{ICE} \\
\dot{\bar{\varphi}}_{EM} &= \bar{\omega}_{EM} \\
\dot{\bar{\varphi}}_{wheel} &= \bar{\omega}_{wheel} \\
\bar{J}_1\dot{\bar{\omega}}_{ICE} &= -\bar{c}_1\left(\bar{\varphi}_{ICE} - \bar{\varphi}_{EM}\right) - \bar{d}_1\left(\bar{\omega}_{ICE} - \bar{\omega}_{EM}\right) + T_{ICE} \\
\bar{J}_2\dot{\bar{\omega}}_{EM} &= \bar{c}_1\left(\bar{\varphi}_{ICE} - \bar{\varphi}_{EM}\right) + \bar{d}_1\left(\bar{\omega}_{ICE} - \bar{\omega}_{EM}\right) \\
&\quad - \frac{1}{R_{total}}\bar{c}_2\left(\frac{1}{R_{total}}\bar{\varphi}_{EM} - \bar{\varphi}_{wheel}\right) - \frac{1}{R_{total}}\bar{d}_2\left(\frac{1}{R_{total}}\bar{\omega}_{EM} - \bar{\omega}_{wheel}\right) + T_{EM} \\
\bar{J}_3\dot{\bar{\omega}}_{wheel} &= \bar{c}_2\left(\frac{1}{R_{total}}\bar{\varphi}_{EM} - \bar{\varphi}_{wheel}\right) + \bar{d}_2\left(\frac{1}{R_{total}}\bar{\omega}_{EM} - \bar{\omega}_{wheel}\right) - T_{disturbance}
\end{aligned}
\tag{2.25}
$$

and the parameters can be approximated by

$$\begin{aligned}
\bar{J}_1 &= J_1 + J_2, \\
\bar{J}_2 &= J_3 + J_4 + J_5 + \frac{1}{R_{gear}^2} J_6, \\
\bar{J}_3 &= J_7 + m_{veh} r_{tire}^2, \\
\bar{c_1} &= c_1, \\
\bar{c_2} &= c_6, \\
\bar{d_1} &= d_1,
\end{aligned} \tag{2.26}$$

whereby J_{K0} is the mass of inertia of the separation clutch and J_{K1} mass of inertia of the gear clutch. The damping factor $\bar{d_2}$ can be approximated by simulation study as in the case of conventional powertrain.

Table 2.5 provides the applied control model parameters. Simulation of a load change by

$\bar{J}_1$	0.32	kgm^2
$\bar{J}_2$	0.238	kgm^2
$\bar{J}_3$	249	kgm^2
$\bar{c}_1$	4.5e3	Nm/rad
$\bar{c}_2$	3.44e4	Nm/rad
$\bar{d}_1$	0.1	Nms/rad
$\bar{d}_2$	350	Nms/rad
$\bar{R}_{total}$	10	1

Table 2.5: Parameters of the control model of a hybrid electric powertrain.

the control model as well as by the detailed model is shown in Fig. 2.20. The simulation shows the same scenario as in Fig. 2.17. Torque of the internal combustion engine T_{ICE} and the electric machine T_{EM} are ramped to 250 Nm. Good agreement between detailed and control model is indicated by the simulation.

2.4 Battery Electric Vehicles

Battery electric vehicles (BEV) have no internal combustion engine and are gaining in importance. The number of electric vehicles sold has increased in the last years and politics supports this development strongly. Reasons for this development are, besides the low CO_2- and NO_x-emission of electric cars, the increasing electric drive range, and the very high level of efficiency. Electric motors can transform electric power to mechanic driving power with less than 10 % loss, as discussed in [Karle16]. Furthermore, the motor characteristics shown in Fig. 2.21 demonstrate the benefits of an electric motor compared to a combustion engine:

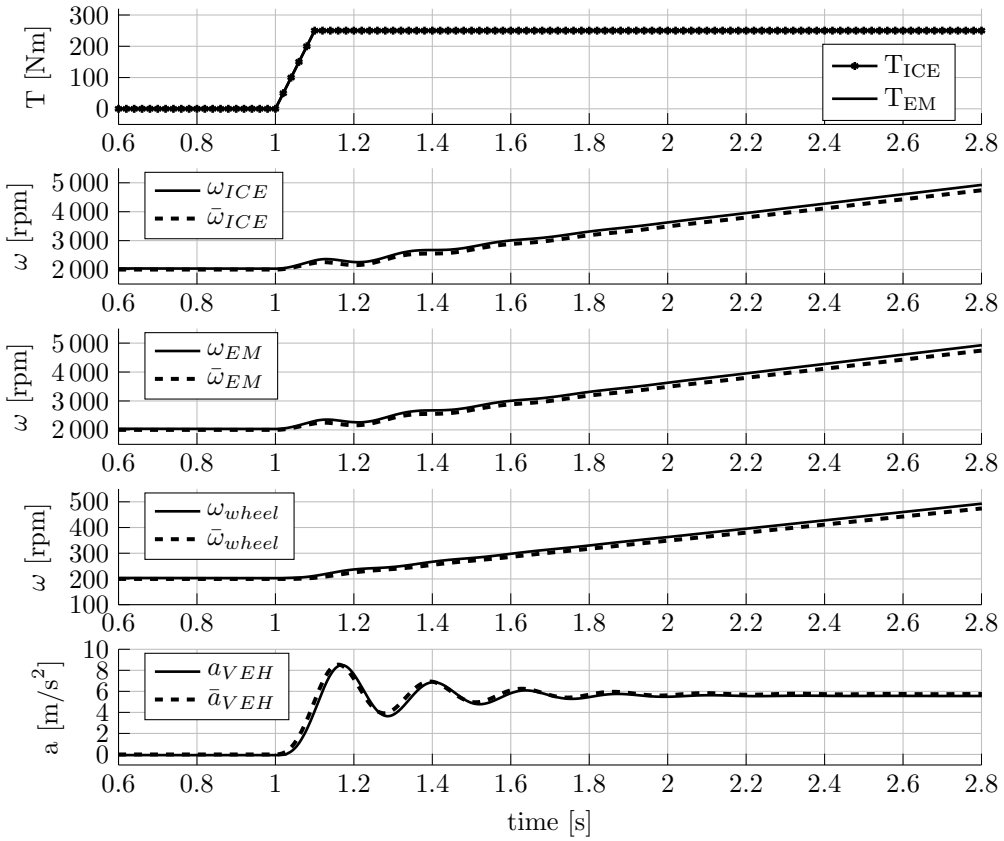

Figure 2.20: Simulation of a load change by detailed and control parallel hybrid electric models. States of the control model are denoted with a bar.

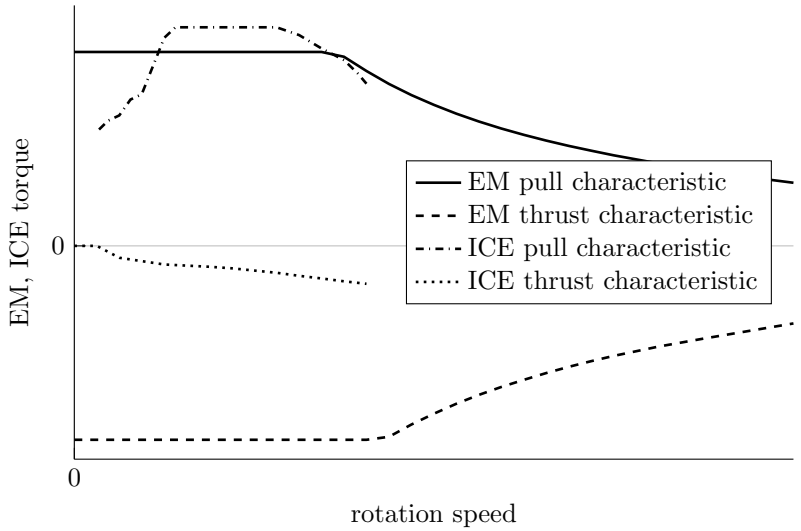

Figure 2.21: Motor characteristic curves of an electric engine for pull and thrust in comparison to the curves of an internal combustion engine.

- An electric motor enables high torque against a large speed range. Therefore, various gears are not necessary to drive in high speed or to take advantage of a high torque

range.

- High torques can be provided even in zero or low speeds. Therefore, no starting element, such as a clutch, is necessary as in the case of combustion engines.

- The available high torque in low speeds of electric motors enable launching with a very high acceleration.

- The thrust characteristic of a electric motor is almost similar to the mirrored pull characteristic. Therefore, the torque range of electric motors is much greater than that of combustion engines and thus high negative torques can be applied. This property is particularly useful for driveline control.

These efficient electric motors can be arranged in a powertrain in various ways. Similar to hybrid electric vehicles, there exist different powertrain architectures for battery electric vehicles. Figure 2.22 shows two common architectures, an electrified front axis and a powertrain with electric wheel hubs, as shown in [WallentowitzFreialdenhoven11] and [KhajepourFallahGoodarzi14]. The electrified front axis is similar to conventional and hybrid electric powertrains. However, the clutch can be omitted here and the transmission has less gears, typically one to two gears. Moreover, in a four wheel drive vehicle with electric axis, there is no mechanical linkage between front and rear axis. Vehicles with electric wheel hubs have the highest degree of freedoms. There is no linkage between front and rear axis as well as left and right wheels. Electric machines can be applied to each wheel and thus it is possible to drive each wheel separately.

In the following, the currently more common vehicles with electric axis are focused. Precisely, an electric front axis with one electric motor is investigated with regard to driveline oscillations.

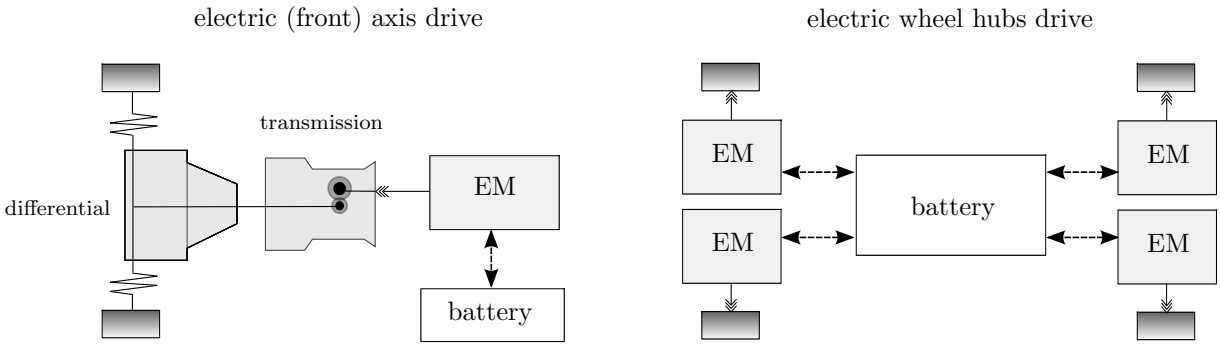

Figure 2.22: Two common architectures of battery electric vehicles.

2.4.1 Detailed Simulation Model

A detailed multibody model of a powertrain with electric axis is shown in Fig. 2.23. The powertrain is driven by the torque T_{EM} of the electric machine and has one fixed gear ratio R_{total}. In contrast to the conventional and hybrid electric powertrain models in Fig. 2.4 and Fig. 2.15 , the drive shafts are modeled here as an own moment of inertia, since the other moments of inertia in the battery electric powertrain are relatively small.

Gear shifting occurs less or not at all in electric vehicles. Therefore, driveline oscillations caused by shifting are reduced. However, other abrupt driving maneuver such as load changes can cause driveline oscillations further on. In particular, the high electric machine dynamics can introduce a large excitation. The detailed multibody model is used to simulate a load change as in the case of conventional and hybrid electric powertrains. Exemplary parameters of the powertrain model are given in Tab. 2.6. Damping coefficients are approximated.

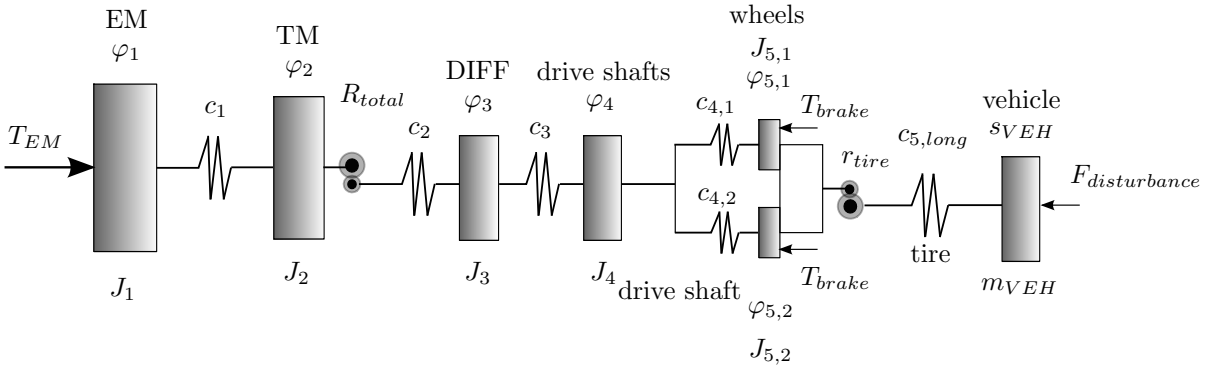

Figure 2.23: Detailed multibody model of a battery electric powertrain.

2.4.2 Oscillation Analysis and Control Model

The parameters of electric powertrains differ from those of conventional powertrains. Moments of inertia of the electric machine and the transmission are much smaller than of conventional. Furthermore, the drive shaft stiffness in this example is smaller than in the examples of conventional and hybrid electric vehicles. This is mostly due to the fact that a front-wheel drive vehicle is analyzed here.

Similar to conventional and hybrid electric powertrains, the gear ratios are incorporated and moments of inertia are sum up as in Eq. (2.1)-(2.7) for conventional powertrains. Hence, the state vector in (2.27) results.

$$\boldsymbol{x}_{BEV} = \left[\varphi_1, \varphi_2, \varphi_{3,R}, \varphi_{4,R}, \varphi_{5,R}, \varphi_{6,R}, \omega_1, \omega_2, \omega_{3,R}, \omega_{4,R}, \omega_{5,R}, \omega_{6,R}\right]^T . \tag{2.27}$$

component	physical size	variable	value	unit
electric machine	moment of inertia	J_1	0.1	kgm^2
transmission	moment of inertia	J_2	0.002	kgm^2
differential	moment of inertia	J_3	0.05	kgm^2
drive shaft left and right	moment of inertia	J_4	$3e-4$	kgm^2
wheel left and right	moment of inertia	J_5	4	kgm^2
vehicle	mass	m_{VEH}	2500	kg
shaft EM-TM	stiffness	c_1	$5e5$	Nm/rad
TM - DIFF	stiffness	c_2	$1e6$	Nm/rad
DIFF - drive shafts	stiffness	c_3	$1e6$	Nm/rad
drive shaft left and right	stiffness	$c_{4,1}, c_{4,2}$	$1.146e4$	Nm/rad
tire linearized	stiffness	$c_{5_{long}}$	$9.8e5$	Nm/rad
gear	total ratio	R_{total}	8	1
tire	radius	r_{tire}	0.35	m

Table 2.6: Parameters of the general model of a battery electric vehicle.

The resulting natural frequencies of the system are

$$\begin{aligned} f_0 &= 0\ Hz, & f_1 &= 6.4\ Hz, & f_2 &= 29.1\ Hz, \\ f_3 &= 2115.8\ Hz, & f_4 &= 6831.7\ Hz, & f_5 &= 9290.1\ Hz. \end{aligned} \tag{2.28}$$

The dominant first frequency with $f_1 = 6.4\ Hz$ is much higher than the dominant frequencies of conventional and hybrid electric vehicles in first and second gear, which are 2.6 Hz and 3.8 Hz, respectively . The reasons for this are smaller moment of inertia of the drive unit and a smaller total gear ratio.

The load change simulation with torque ramp T_{EM} presented in Fig. 2.24 shows clearly the first frequency f_1 in the angular velocities $\omega_{EM}, \omega_{weel}$ of electric machine and wheels, and in the vehicle acceleration signal a_{VEH}.

Despite the different parameters, the dominant eigenvector of f_1, depicted in Fig. 2.25, is similar to the first mode of conventional and hybrid electric powertrains, see Fig. 2.8 and Fig. 2.18, respectively. Since only one actuator is present a control model with two-degree of freedom is sufficient. A two-mass model as illustrated in Fig. 2.25 (right) can be synthesized to represent the first eigenmode. The parameters of the control model are denoted with a bar.

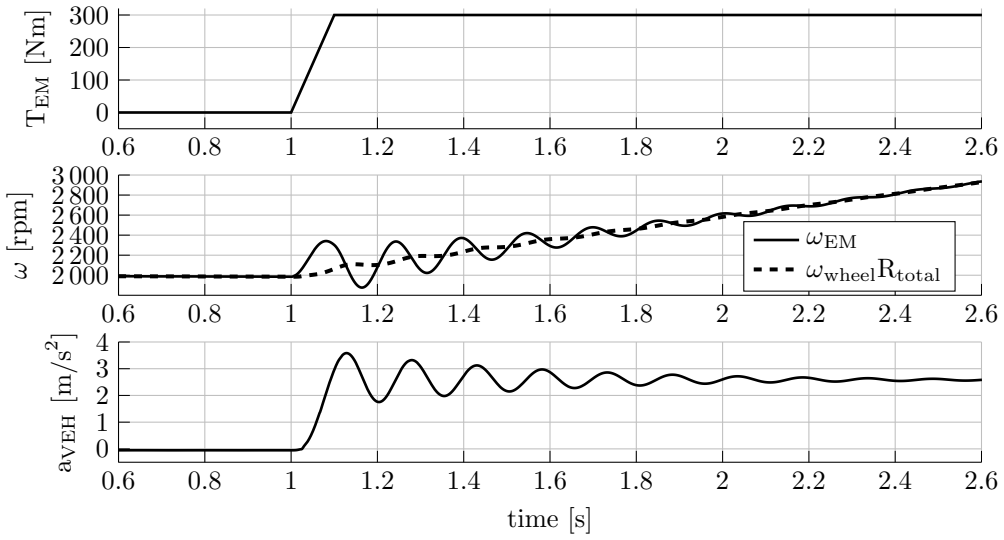

Figure 2.24: Simulation of a load change of a battery electrified powertrain.

The equations of motion of the battery electric vehicle control model reads

$$
\begin{aligned}
\dot{\bar{\varphi}}_{EM} &= \bar{\omega}_{EM} \\
\dot{\bar{\varphi}}_{wheel} &= \bar{\omega}_{wheel} \\
\bar{J}_1 \dot{\bar{\omega}}_{EM} &= -\frac{1}{R_{total}} \bar{c} \left(\frac{1}{R_{total}} \bar{\varphi}_{EM} - \bar{\varphi}_{wheel} \right) - \frac{1}{R_{total}} \bar{d} \left(\frac{1}{R_{total}} \bar{\omega}_{EM} - \bar{\omega}_{wheel} \right) + T_{EM} \\
\bar{J}_2 \dot{\bar{\omega}}_{wheel} &= \bar{c} \left(\frac{1}{R_{total}} \bar{\varphi}_{EM} - \bar{\varphi}_{wheel} \right) + \bar{d} \left(\frac{1}{R_{total}} \bar{\omega}_{EM} - \bar{\omega}_{wheel} \right) - T_{disturbance}.
\end{aligned}
\tag{2.29}
$$

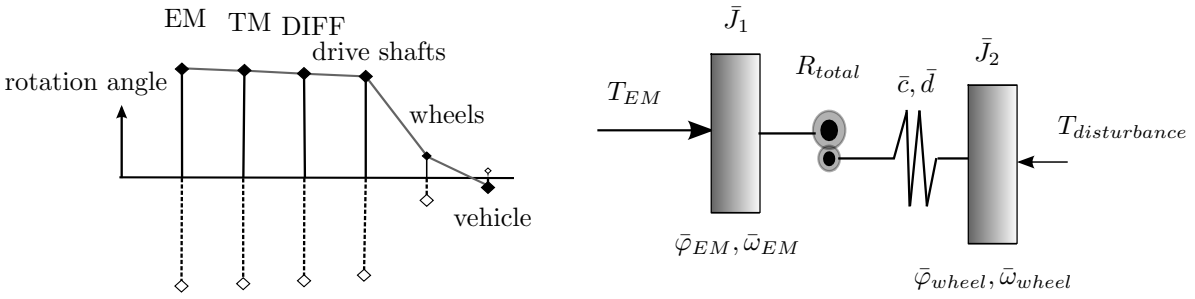

Figure 2.25: Normal mode of the dominant frequency 6.4 Hz (left) and two-mass control model (right) of a battery electric powertrain.

Control model parameters can be found by

$$\begin{aligned} \bar{J}_1 &= J_1 + J_2 + \frac{1}{R_{gear}^2}\left(J_3 + J_4\right), \\ \bar{J}_2 &= J_5 + m_{VEH} r_{tire}^2, \\ \bar{c} &= c_4. \end{aligned} \tag{2.30}$$

Parameters of the control model are summarized in Tab. 2.7. Damping parameter $\bar{d}$ is

$\bar{J}_1$	0.103	kgm^2
$\bar{J}_2$	310.25	kgm^2
$\bar{c}$	1.146e4	Nm/rad
$\bar{d}$	30	Nms/rad
R_{total}	8	1

Table 2.7: Parameters of the control model of a conventional powertrain with closed clutch.

approximated by comparison of the control model with the detailed simulation model. Figure 2.26 shows a load change by the engine torque T_{EM}. It can be seen that the control model matches the detailed model very precisely.

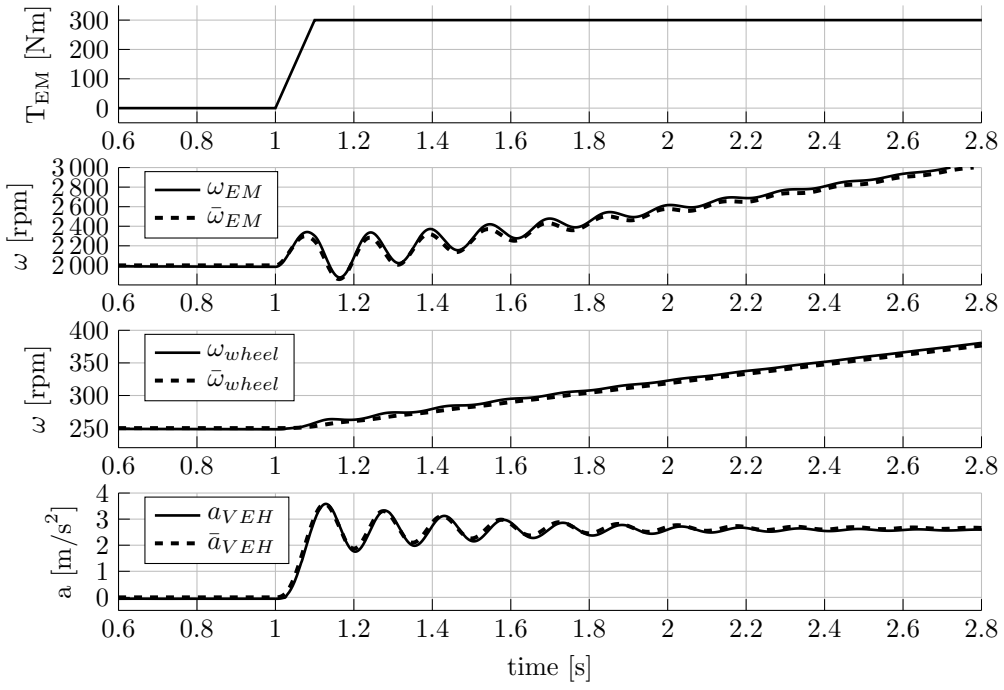

Figure 2.26: Simulation of load change by detailed and control battery electric models. States of the control model are marked with a bar.

2.5 Discussion of the Control Models

In this chapter general powertrain models of conventional, hybrid electric and battery electric vehicles were presented and the linear oscillation behavior of all three powertrain types were investigated. Despite the different powertrain architectures, all eigenvectors of the lowest dominant frequency are similar, as it is shown in Fig. 2.27, even though in electrical powertrain the corresponding frequency is significantly higher. These dominant eigenmodes are particularly visible after suggestions through load changes by the drive unit torque. Especially load changes by electric machines can cause undesired driveline oscillations with high amplitudes due to the high agility of the machines.

The typical dominant low eigenfrequencies of powertrains are between 2 to 8 Hz, which coincide with the eigenfrequency of the human stomach. Hence, these oscillations are particularly uncomfortable for humans as discussed in [KnotheStichel16]. Therefore, control methods are needed to reduce these oscillations. In order to archive this, linear control models were deduced for all three powertrain types in this chapter. In the next Chapter 3 the derived control models are used to design feedforward and feedback controllers. Chapter 4 and 5 extend these control models by dominant dynamics resulting from backlash and time delay.

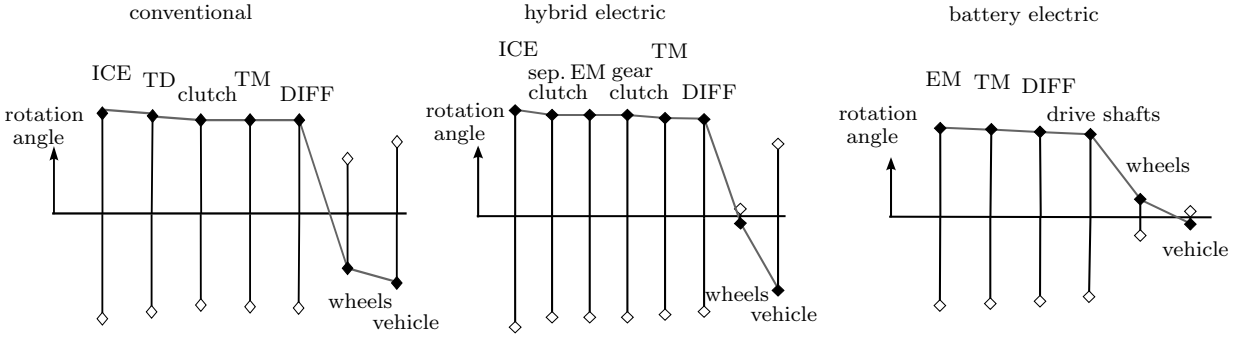

Figure 2.27: Dominant first eigenvectors of a conventional, hybrid electric, and battery electric vehicle.

Chapter 3

Linear Powertrain Control

The previous chapter discusses undesired torsional dynamics of the powertrain, which are induced by load changes or launching. This chapter derives control methods based on linear control models to prevent and reduce these oscillations. The methods include flatness-based feedforward controllers and feedback controllers with desired trajectories for conventional, parallel hybrid electric, and battery electric powertrains. First, a coordinate transformation is applied for a two-mass and three-mass model to separate the rigid body mode from the other modes. Then, the damping behavior of the uncontrolled system is investigated and a desired dynamic behavior is defined. Accordingly, appropriate control approaches are derived. Finally, simulations and experimental results demonstrate that the proposed approaches ensure good damping behavior, greater freedom of choice concerning the transition time and good controlled transient behavior.

3.1 Coordinate Transformation

The system dynamics representation in (2.13), (2.21), (2.29), and (2.25) are not appropriate for torsional vibration damping control design. The reason is that the rigid body mode, indicated by an eigenvalue with $\omega_0 = 0\ \frac{1}{s}$ exists in these system equations. However, the focus is to control the torsion mode and not the rigid mode. Furthermore, the rigid body mode is not asymptotically stable and makes control design more difficult. The following example shows that the rotation angles of a system with rigid body mode can tend to infinity. A two-mass powertrain model is deflected by the initial condition $\boldsymbol{x}_{ext,0} = [0, 0, \omega_{ic,1}, \omega_{ic,2}]^T$ with $\omega_{ic,1}, \omega_{ic,2} \in \mathbb{R}$, then the moments of inertia of the system J_1, J_2 will rotate with a constant velocity and the rotation angles go towards to infinity, although the input and disturbance are zero. Figure 3.1 illustrates the rigid body mode, when the two-mass system with parameters from Tab. 2.2 is deflected by initial condition $\boldsymbol{x}_{ext}(0) = [0, 0, R, 1]^T$ and input and disturbance are set to zero.

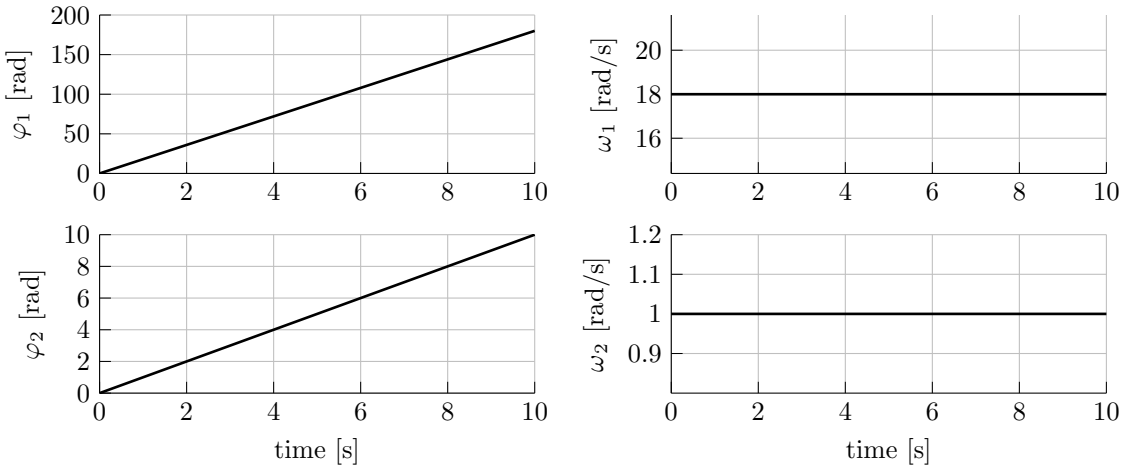

Figure 3.1: Simulation of the rigid body mode. The rotation angles φ_1, φ_2 tend to infinity and the angular velocities ω_1, ω_2 are constant.

This behavior is physically desired and it is not the objective of a control method to stabilize rotation angle and angular velocity to zero, but to control the torsional oscillations to zero. Therefore, the rigid body mode is separated from the dynamics equations of the two-mass and three-mass models by applying a transformation to Byrnes-Isidori normal form. The Byrnes-Isidori normal form is introduced in [ByrnesIsidori88] and [ByrnesIsidori91]. A general introduction into the normal form for linear systems is for instance given in [Ferdinand06].

Two-Mass Model

The equations of motion of a two-mass model, as shown in Fig. 3.2, are revisited. This model is used for conventional powertrains in (2.13) and (2.21), and for battery electric powertrains in (2.29). The system states are given as $\boldsymbol{x}_{ext} = [\varphi_1, \varphi_2, \omega_1, \omega_2]^T$ and the correspond equations are

$$\begin{aligned}
\dot{\varphi}_1 &= \omega_1 \\
\dot{\varphi}_2 &= \omega_2 \\
\dot{\omega}_1 &= -\frac{1}{RJ_1} c \left(\frac{1}{R}\varphi_1 - \varphi_2 \right) - \frac{1}{RJ_1} d \left(\frac{1}{R}\omega_1 - \omega_2 \right) + \frac{1}{J_1} u \\
\dot{\omega}_2 &= \frac{1}{J_2} c \left(\frac{1}{R}\varphi_1 - \varphi_2 \right) + \frac{1}{J_2} d \left(\frac{1}{R}\omega_1 - \omega_2 \right) - \frac{1}{J_2}\delta.
\end{aligned} \tag{3.1}$$

For system parameters c, d, J_1, J_2, R from Tab. 2.2, Tab. 2.3 or Tab. 2.7, the system has double zero eigenvalues $\lambda_{1,2} = 0$ and complex conjugated eigenvalues $\lambda_{3,4} = a \pm bi$ with $a < 0, b \neq 0$ and $a, b \in \mathbb{R}$. The algebraic multiplicity of the eigenvalue $\lambda_{1,2} = 0$ is not equal

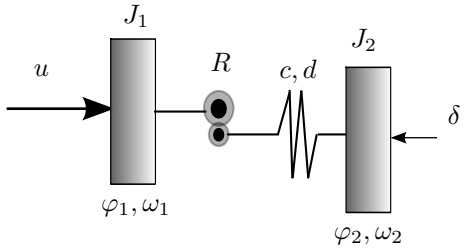

Figure 3.2: Two-mass control model.

to its geometric multiplicity. The algebraic multiplicity is two and the geometric is one. Hence, the system is unstable due to the rigid body mode.

In order to separate the rigid body mode with double eigenvalue $\lambda_{1,2} = 0$ from the remaining system, the system is transformed. The torsion rotation angle is defined as the system output

$$y = \frac{1}{R}\varphi_1 - \varphi_2 \tag{3.2}$$

to represent the torsional behavior. Using this output the Byrnes-Isidori normal form of the two-mass model is derived. New states $\boldsymbol{z} = [z_1, z_2, z_3, z_4]^T$ are introduced with

$$\begin{aligned} z_1 = y = \Delta\varphi &= \frac{1}{R}\varphi_1 - \varphi_2 \\ z_2 = \dot{y} = \Delta\omega &= \frac{1}{R}\omega_1 - \omega_2. \end{aligned} \tag{3.3}$$

The remaining two states z_3, z_4 can be chosen such that the transformation matrix $\boldsymbol{\phi}$ with

$$\boldsymbol{z} = \boldsymbol{\phi}^{-1}\boldsymbol{x}_{ext} \tag{3.4}$$

is regular. The following states are selected

$$\begin{aligned} z_3 &= \varphi_2 \\ z_4 &= \omega_2. \end{aligned} \tag{3.5}$$

Hence, the inverse transformation matrix is given as

$$\boldsymbol{\phi}^{-1} = \begin{bmatrix} \frac{1}{R} & -1 & 0 & 0 \\ 0 & 0 & \frac{1}{R} & -1 \\ 0 & 1 & 0 & 0 \\ 0 & 0 & 0 & 1 \end{bmatrix}. \tag{3.6}$$

The matrix $\boldsymbol{\phi}$ is a global diffeomorphism as the transformation is linear.

Applying the new states the dynamics in Byrnes-Isidori normal form reads

$$\begin{aligned} &\text{input-output behavior} \quad \begin{cases} \dot{z}_1 = \dot{y} = \Delta\dot{\varphi} = z_2 \\ \dot{z}_2 = \ddot{y} = \Delta\dot{\omega} = -\Theta c z_1 - \Theta d z_2 + \dfrac{1}{J_1 R}u + \dfrac{1}{J_2}\delta \end{cases} \\ &\text{internal dynamics} \quad \begin{cases} \dot{z}_3 = \dot{\varphi}_2 = \omega_2 \\ \dot{z}_4 = \dot{\omega}_2 = \dfrac{1}{J_2}c z_1 + \dfrac{1}{J_2}d z_2 - \dfrac{1}{J_2}\delta \end{cases} \end{aligned} \tag{3.7}$$

with summarized moments of inertia $\Theta = \frac{J_1 R^2 + J_2}{J_1 J_2 R^2}$. The following state distinction is made in order to separate the internal dynamics of the system from the remaining:

$$\boldsymbol{\nu} = [z_1, z_2]^T, \quad \boldsymbol{\eta} = [z_3, z_4]^T. \tag{3.8}$$

The internal dynamics is often difficult to analyze, therefore the concept of zero dynamics is used. The definition of zero-dynamics is given as:

Definition 1 ([Isidori95])**.** *The zero-dynamics is defined as the internal dynamics of a system, such that the output y is zero for a particular initial condition $x(0)$ and input u.*

Applying

$$\nu(0) = 0, \quad \eta(0) = \eta_0 \in \mathbb{R}^2, \quad u = J_1 R \left[\Theta c \nu_1 + \Theta d \nu_2 - \frac{1}{J_2} \delta \right] \tag{3.9}$$

for system (3.7), then it holds

$$y(t) = 0, \quad \forall t \tag{3.10}$$

and the zero-dynamics is given as

$$\begin{aligned} \dot{\eta}_1 &= \eta_2 \\ \dot{\eta}_2 &= 0, \end{aligned} \tag{3.11}$$

with $\eta(0) = \eta_0$.

The zero-dynamics (3.11) represents the rigid body mode and is not further considered in control design. Therefore, further investigations on the torsional dynamics and control design are based on the reduced state $\boldsymbol{x} = \boldsymbol{\nu} = [\Delta\varphi, \Delta\omega]^T$ and the reduced dynamics

$$\begin{aligned} \Delta\dot{\varphi} &= \Delta\omega \\ \Delta\dot{\omega} &= -\Theta c \Delta\varphi - \Theta d \Delta\omega + \frac{1}{J_1 R} u + \frac{1}{J_2} \delta \end{aligned} \tag{3.12}$$

with $\boldsymbol{x}(0) = \boldsymbol{x}_0$ and $\Theta = \frac{J_1 R^2 + J_2}{J_1 J_2 R^2}$. The reduced dynamics is used for control design of a two-mass system.

Remark

The transformation matrix $\boldsymbol{\phi}$ from Eq. (3.6) is not a modal transformation matrix. The following simple example illustrates that the transformation to torsion rotation angle and angular velocity is a usual coordinate transformation. Let us define $J_1 = J_2 = R = 1$, zero damping $d = 0$, and zero input and disturbance $u = \delta = 0$. The spring stiffness is defined as c. Then the equations of motion of the two-mass model with minimal coordinates $\boldsymbol{p} = [\varphi_1, \varphi_2]^T$ reads

$$\underbrace{\begin{bmatrix} 1 & 0 \\ 0 & 1 \end{bmatrix}}_{=:\boldsymbol{M}} \ddot{\boldsymbol{p}} + \underbrace{\begin{bmatrix} c & -c \\ -c & c \end{bmatrix}}_{=:\boldsymbol{K}} \boldsymbol{p} = 0. \tag{3.13}$$

Eigenvalues, eigenvectors and the modal transformation matrix are calculated for this system. The eigenvalue problem can be set up with the Ansatz

$$\boldsymbol{p} = \hat{\boldsymbol{p}} \sin(\omega t) \tag{3.14}$$

as for instance shown in [SchiehlenEberhard14], and [MagnusPoppSextro13]. This gives

$$\left(\boldsymbol{K} - \omega^2 \boldsymbol{M}\right) \hat{\boldsymbol{p}} = 0. \tag{3.15}$$

There exists non-trivial solutions, if the characteristic matrix $(\boldsymbol{K} - \omega^2 \boldsymbol{M})$ is singular. Hence, it must hold

$$\det\left(\boldsymbol{K} - \omega^2 \boldsymbol{M}\right) = 0 \tag{3.16}$$

and thus the eigenfrequencies of the system are

$$\omega_1 = 0, \quad \omega_2 = \sqrt{2c}. \tag{3.17}$$

The eigenvector of ω_1 reads

$$\hat{\boldsymbol{p}}_1 = \begin{bmatrix} 1 \\ 1 \end{bmatrix} \tag{3.18}$$

and of ω_2

$$\hat{\boldsymbol{p}}_2 = \begin{bmatrix} 1 \\ -1 \end{bmatrix}. \tag{3.19}$$

Finally, the modal matrix is given as

$$\hat{\boldsymbol{X}} = \begin{bmatrix} \hat{\boldsymbol{p}}_1 & \hat{\boldsymbol{p}}_2 \end{bmatrix} = \begin{bmatrix} 1 & 1 \\ 1 & -1 \end{bmatrix} \tag{3.20}$$

and defines the transformation of states $\boldsymbol{p}$ and modal coordinates $\boldsymbol{q}$ with

$$\boldsymbol{p} = \hat{X} \boldsymbol{q}. \tag{3.21}$$

Furthermore, the following orthogonality relations hold for the eigenvectors

$$\begin{aligned} i \neq k: &\quad \hat{\boldsymbol{p}}_i^T \boldsymbol{M} \hat{\boldsymbol{p}}_k = 0, \\ i \neq k: &\quad \hat{\boldsymbol{p}}_i^T \boldsymbol{K} \hat{\boldsymbol{p}}_k = 0, \\ i = k: &\quad \hat{\boldsymbol{p}}_i^T \boldsymbol{M} \hat{\boldsymbol{p}}_k = 1, \\ i = k: &\quad \hat{\boldsymbol{p}}_i^T \boldsymbol{K} \hat{\boldsymbol{p}}_k = \omega_i^2. \end{aligned} \tag{3.22}$$

Derivation for these relations are given for instance in [DresigRockhausenHolzweißig13].

Now, the Byrnes-Isidori transformation can be compared with the modal transformation matrix $\hat{\boldsymbol{X}}$ from Eq. (3.20). For system (3.13) with state $\boldsymbol{p} = [\varphi_1, \varphi_2]^T$ the Byrnes-Isidori transformation matrix to the new state $\bar{\boldsymbol{z}} = [\Delta\varphi, \varphi_2]^T$ is given as

$$\bar{\boldsymbol{\phi}} = \begin{bmatrix} 1 & -1 \\ 0 & 1 \end{bmatrix}, \tag{3.23}$$

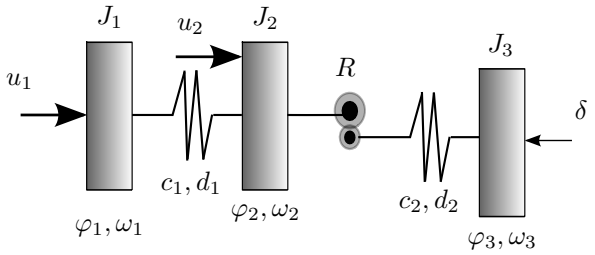

Figure 3.3: Three-mass control model.

with transformation

$$\boldsymbol{p} = \bar{\boldsymbol{\phi}}\bar{\boldsymbol{z}}. \tag{3.24}$$

It follows that the transformation matrix $\bar{\boldsymbol{\phi}}$ in (3.23) does not correspond to the modal transformation matrix $\hat{\boldsymbol{X}}$ from Eq. (3.20). Additionally the transformation matrix $\bar{\boldsymbol{\phi}}$ in (3.23) does not fulfill the relations in (3.22) and is therefore not a modal matrix.

□

Three-Mass Model

The same separation approach applies to the three-mass model. The general equations of motion of a three-mass model, as illustrated in Fig. 3.3, are

$$\begin{aligned}
\dot{\varphi}_1 &= \omega_1 \\
\dot{\varphi}_2 &= \omega_2 \\
\dot{\varphi}_3 &= \omega_3 \\
J_1\dot{\omega}_1 &= -c_1\left(\varphi_1 - \varphi_2\right) - d_1\left(\omega_1 - \omega_2\right) + u_1 \\
J_2\dot{\omega}_2 &= c_1\left(\varphi_1 - \varphi_2\right) + d_1\left(\omega_1 - \omega_2\right) \\
&\quad - \frac{1}{R}c_2\left(\frac{1}{R}\varphi_2 - \varphi_3\right) - \frac{1}{R}d_2\left(\frac{1}{R}\omega_2 - \omega_3\right) + u_2 \\
J_3\dot{\omega}_3 &= c_2\left(\frac{1}{R}\varphi_2 - \varphi_3\right) + d_2\left(\frac{1}{R}\omega_2 - \omega_3\right) - \delta,
\end{aligned} \tag{3.25}$$

see also (2.25). The system state vector $\boldsymbol{x}_{ext} = [\varphi_1, \varphi_2, \varphi_3, \omega_1, \omega_2, \omega_3]^T$ is reduced to the new state vector $\boldsymbol{x} = [\Delta\varphi_1, \Delta\varphi_2, \Delta\omega_1, \Delta\omega_2]^T$ with

$$\Delta\varphi_1 = \varphi_1 - \varphi_2, \quad \Delta\varphi_2 = \frac{1}{R}\varphi_2 - \varphi_3, \quad \Delta\omega_1 = \omega_1 - \omega_2, \quad \Delta\omega_2 = \frac{1}{R}\omega_2 - \omega_3, \tag{3.26}$$

which represent torsion rotation angles and torsion angular velocities. The reduced dynamics equations read

$$\begin{aligned}
\Delta\dot{\varphi}_1 &= \Delta\omega_1 \\
\Delta\dot{\varphi}_2 &= \Delta\omega_2 \\
\Delta\dot{\omega}_1 &= -\Theta_1 c_1 \Delta\varphi_1 - \Theta_1 d_1 \Delta\omega_1 + \frac{1}{J_2 R} c_2 \Delta\varphi_2 + \frac{1}{J_2 R} d_2 \Delta\omega_2 + \frac{1}{J_1} u_1 - \frac{1}{J_2} u_2 \\
\Delta\dot{\omega}_2 &= \frac{1}{J_2 R} c_1 \Delta\varphi_1 + \frac{1}{J_2 R} d_1 \Delta\omega_1 - \Theta_2 c_2 \Delta\varphi_2 - \Theta_2 d_2 \Delta\omega_2 + \frac{1}{J_2 R} u_2 + \frac{1}{J_3}\delta
\end{aligned} \tag{3.27}$$

with $\boldsymbol{x}(0) = \boldsymbol{x}_0$ and $\Theta_1 = \frac{J_1+J_2}{J_1 J_2}$ and $\Theta_2 = \frac{J_2 R^2 + J_3}{J_2 J_3 R^2}$. The internal dynamics, which describes the rigid body mode, is neglected for vibration damping control as in the case of the two-mass model. The reduced model is used for control design of a three-mass system.

3.2 Uncontrolled Damping Behavior

The present damping behavior of the derived control systems (2.13), (2.21), (2.25), (2.29) of conventional, hybrid electric and battery electric powertrains are investigated. The systems describe stable damped harmonic oscillators, since the damping coefficients are all greater than zero. However, a further distinction can be made. Damped harmonic oscillators with n states can be distinguished between undamped, underdamped, critically damped and overdamped systems, see [WilliamsLawrence07]. In order to make the distinction, the eigenvalues λ_i with $i \in \{1, 2, \ldots, n\}$ of the systems have to be calculated.

The conditions for undamped, underdamped and overdamped depending on the eigenvalues λ_i are summarized in Tab. 3.1. The specific case of critically damped systems is defined

	real part	imaginary part
undamped	$\forall i \, \mathrm{Re}(\lambda_i) = 0$	$\exists \, (\mathrm{Im}(\lambda_i), \mathrm{Im}(\lambda_j))$ complex conjugated
underdamped	$\forall i \, \mathrm{Re}(\lambda_i) \leq 0, \exists i \, \mathrm{Re}(\lambda_i) < 0$	$\exists \, (\mathrm{Im}(\lambda_i), \mathrm{Im}(\lambda_j))$ complex conjugated
overdamped	$\forall i \, \mathrm{Re}(\lambda_i) \leq 0, \exists i \, \mathrm{Re}(\lambda_i) < 0$	$\forall i \, \mathrm{Im}(\lambda_i) = 0$

Table 3.1: Distinction of oscillation behavior by eigenvalues.

as the condition between underdamped and overdamped. The imaginary parts of the eigenvalues become zero in this case.

In the following, eigenvalues for two-mass and three-mass models are calculated and the related damping behavior for the derived conventional, hybrid electric and battery electric powertrains are given.

Two-Mass Model

The unforced dynamics of the two-mass model in (3.12) can be described with a second order dynamic equation

$$\ddot{q} + \Theta d\dot{q} + \Theta c q = 0 \tag{3.28}$$

with minimal coordinate $q = \Delta\varphi$ and $u = \delta = 0$. Defining the natural frequency of the undamped system as

$$\omega_n = \sqrt{\Theta c}, \tag{3.29}$$

and the damping ratio as

$$\xi = \frac{\Theta d}{2\sqrt{c\Theta}}, \tag{3.30}$$

then dynamics equation (3.28) can be rewritten to

$$\ddot{x} + 2\xi\omega_n\dot{x} + \omega_n^2 x = 0. \tag{3.31}$$

Hence, the eigenvalues of system (3.31) are given as

$$\lambda_{1,2} = -\omega_n \left(\xi \pm \sqrt{\xi^2 - 1}\right). \tag{3.32}$$

Using Tab. 3.1 it can be distinguished between:

- $\xi < 0$: the system is unstable
- $\xi = 0$: the system is undamped
- $0 < \xi < 1$: the system is underdamped
- $\xi = 1$: the system is critically damped
- $\xi > 1$: the system is overdamped

For underdamped systems the eigenfrequency f reads

$$f = \omega_n\sqrt{1 - \xi^2}. \tag{3.33}$$

Damping ratios, frequencies, and periods of the powertrain two-mass control models from Chapter 2 with parameters from Tab. 2.2, Tab. 2.3, Tab. 2.7, respectively, are summarized in Tab. 3.2. From Tab. 3.2 it can be seen that the eigenfrequencies of the control models correspond to the dominant eigenfrequencies of the detailed simulation models in Chapter 2. Furthermore, the damping ratios show that the systems are underdamped and close to undamped. Usually, powertrains are designed as underdamped systems in order to reduce energy loss due to damping. These systems oscillates with an amplitude gradually decreasing to zero.

	ξ	f	T
conv. powertrain closed clutch	0.096	3.0 Hz	0.333 s
conv. powertrain open clutch	0.038	8.3 Hz	0.121 s
battery electric powertrain	0.055	6.7 Hz	0.150 s

Table 3.2: Damping ratio, frequency, and period of two-mass control models.

Three-Mass Model

The unforced reduced three-mass model (3.27) in state-space representation reads

$$\dot{\boldsymbol{x}} = \underbrace{\begin{bmatrix} 0 & 0 & 1 & 0 \\ 0 & 0 & 0 & 1 \\ -c_1\Theta_1 & \frac{c_2}{J_2 R} & -d_1\Theta_1 & \frac{d_2}{J_2 R} \\ \frac{c_1}{J_2 R} & -c_2\Theta_2 & \frac{d_1}{J_2 R} & -d_2\Theta_2 \end{bmatrix}}_{=:\boldsymbol{A}_3} \boldsymbol{x}. \tag{3.34}$$

The eigenvalues $\boldsymbol{\lambda}$ of the system can be found by solving the fourth order characteristic polynomial

$$det\left(\boldsymbol{A}_3 - \boldsymbol{\lambda}\boldsymbol{I}\right) = 0, \tag{3.35}$$

with fourth order identity matrix $\boldsymbol{I}$.

Unlike in the case of the two-mass model, the analytical calculation of the eigenvalues of the three-mass model is much more difficult. Therefore, eigenfrequency and damping ratio are derived on the basis of numerically calculated eigenvalues.

The eigenfrequency of the system is given as

$$f_{i,j} = \frac{|\operatorname{Im}(\lambda_{i,j})|}{2\pi}, \text{with } \operatorname{Im}(\lambda_i) \neq \operatorname{Im}(\lambda_i) \tag{3.36}$$

The natural frequency $\omega_{n,i,j}$ of the undamped system can be found by

$$\omega_{n,i,j} = |\lambda_{i,j}|. \tag{3.37}$$

Then the damping ratio $\xi_{i,j}$ is defined with $\omega_{n,i,j}$ as

$$\xi_{i,j} = -\frac{\operatorname{Re}(\lambda_{i,j})}{\omega_{n,i,j}}. \tag{3.38}$$

The damping ratios, frequencies and periods of the considered three-mass model (3.34) with parameters from Tab. 2.5 are summarized in Tab. 3.3.

The characteristic values show that the system is underdamped and the eigenfrequencies match the frequencies of the general hybrid electric powertrain model as in cases of the two-mass control models.

The investigated powertrain systems are all only lightly damped.

	ξ	f	T
mode 1	0.135	4.282 Hz	0.234 s
mode 2	0.026	29.23 Hz	0.034 s

Table 3.3: Damping ratio, frequency, and period of the three-mass control model.

3.3 Desired Dynamical Behavior

In this section specifications for feedforward and feedback control are presented. The desired damping behavior is defined, independent transition time for feedforward control is requested and the need of desired trajectories for feedback control is stated.

3.3.1 Critical Damping

The damping ratios of the investigated powertrains are all significantly smaller than one and thus the uncontrolled powertrains are underdamped. The undesired vibration behavior of underdamped systems can be observed in Fig. 3.4. The figure shows the step responses for an underdamped $\xi_1 = 0.1$, corresponds almost to Tab. 3.2, critically damped $\xi_2 = 1$ and overdamped $\xi_3 = 2$ two-mass control system. The system is parameterized by values of the conventional powertrain with closed clutch from Tab. 2.2. The damping parameter d_i is calculated by the chosen damping ratio ξ_i:

$$d_i = \frac{\xi_i 2\sqrt{c\theta}}{\theta}, \quad i \in \{1, 2, 3\}. \tag{3.39}$$

It can be identified from the figure that the underdamped system shows an undesired behavior due to many oscillations with high amplitudes. The overdamped system is vibration-free, but the step-response is very slow. However, the critically damped system has the desired step response, since it shows the best trade-off between fast convergent and vibration damping. A feedback controller can be used to reach the desired critically damped behavior.

3.3.2 Independent Transition Time

The vibration amplitudes of undamped or underdamped systems after load changes depend on how the torque of the excitation is built up. Thereby, the shape of the torque build-up is significant. If a ramp is chosen for the torque built up, then only the transition time can be varied. In [DresigFidlin14] the influence of the transition time of a ramp is investigated for an undamped two-mass model. It is shown that if the transition time is set to a multiple of the period T of the system, then no oscillations appear. The time simulation on the left in Fig. 3.5 shows this effect with parameters from Tab. 2.2 and damping parameter $d = 0$.

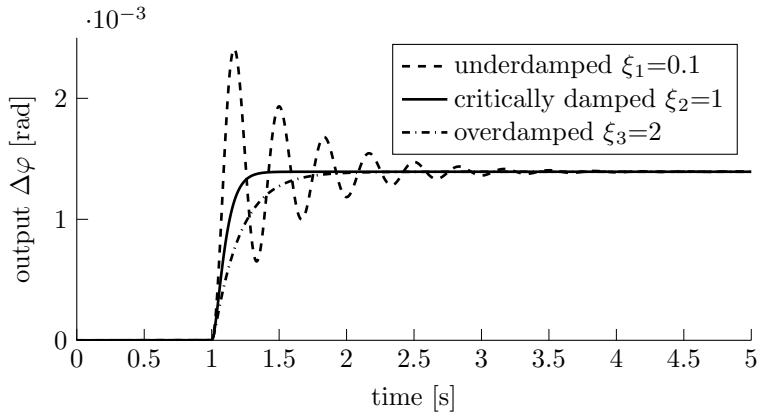

Figure 3.4: Step responses of an underdamped, critically damped and overdamped two-mass model.

The output of the system, which is excited by the ramp with the shortest transition time $T_1 = 0.5\ T$ have the highest amplitude.

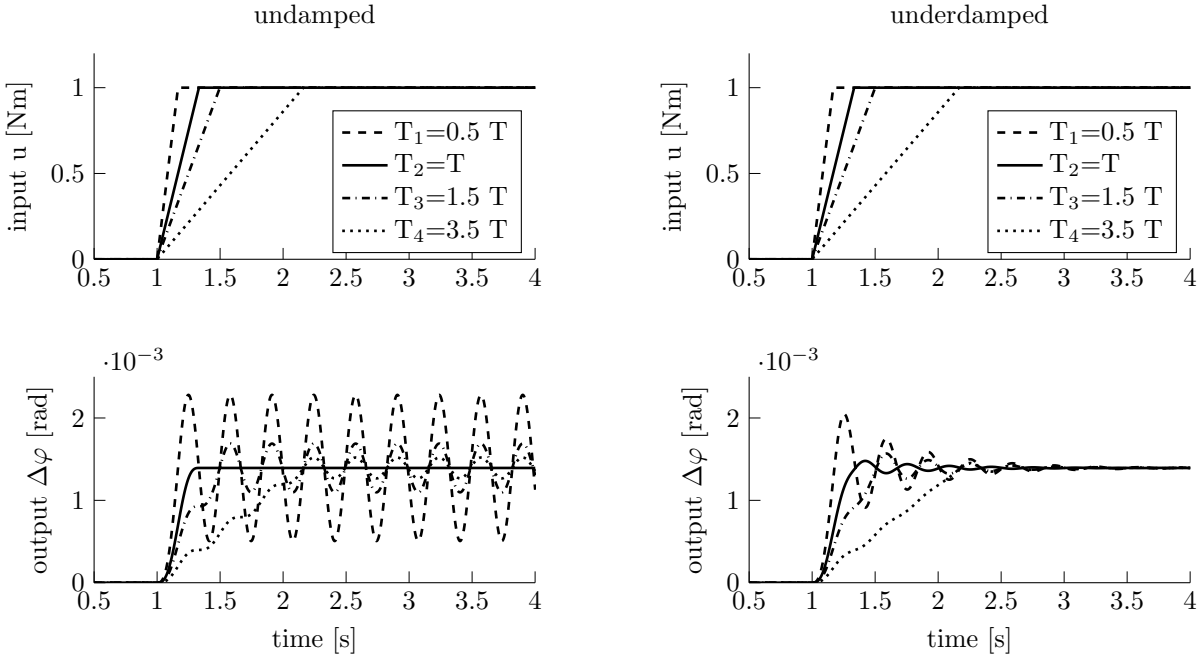

Figure 3.5: Load changes with ramps with varied transition time T_1, T_2, T_3, T_4 of an undamped (left) and underdamped (right) two-mass model.

Smaller amplitudes appear with transition time $T_3 = 1.5\ T$ and $T_4 = 3.5\ T$. However, the greater transition times T_3, T_4 have greater amplitudes as $T_2 = T$. The underdamped case with damping parameter $d = 350\ \frac{Nms}{rad}$ and damping ratio $\xi = 0.0096$ is shown on the right in Fig. 3.5. The effects are comparable with the effect of the undamped system. Nevertheless, there are small vibration amplitudes for transition time equal to the period as $T_2 = T$.

It follows from these investigations that if a ramp is applied for load changes, the transition time should be close to the multiple of the period of the uncontrolled system. However, this demand is very restrictive. Usually, the driver determines the transition time by depressing the accelerator pedal faster or slower. The vehicle has to accelerate vibration-free according to the time requirements of the driver. Therefore, load changes via ramps are not satisfactory and more advanced feedforward control methods with appropriate torque shapes offer more advantages.

3.3.3 Controlled Transient Behavior

Feedforward control strategies, as ramps with appropriate transition time or feedforward control methods, can enable vibration-free transient processes, when the system dynamics is fully known and there are no disturbances. However, these conditions can never be guaranteed. Therefore, an additional feedback controller is necessary to overcome the uncertainties and to get a better command response. However, steady-state feedback controllers are not suitable, since the feedback controller has to deal with transient processes. Thus, trajectory tracking is desired and reference trajectories are required for feedback control.

3.4 Model-Based Linear Transient Control

In this section a two-degree of freedom control scheme, as illustrated in Fig. 3.6, is derived to meet the demands presented in the previous section. The driver request is interpreted by the pedal moving and a desired input torque u_{des} is generated. A linear flatness-based feedforward controller is designed to prevent driveline oscillations due to load changes and launching. The transition time can be variably chosen. Furthermore, the flatness-based control approach provides desired trajectories. Thus, a proportional feedback controller can apply these references and therefore feedback control during the transient is possible. The control gain of the proportional feedback controller can then be chosen such that the closed loop system is critically damped. This approach of generally combining feedforward and feedback control to control the drive unit is protected in patent [PhamScholzRoulet16].

3.4.1 Differentially Flat Feedforward Control

The concept of differentially flatness was introduced in [FliessEtAl92] and [FliessEtAl95]. Applying this concept, system state $\boldsymbol{x}$, input u, and output y can be defined as functions of the so-called *flat output* z and its derivatives. The flat output z itself is a function of

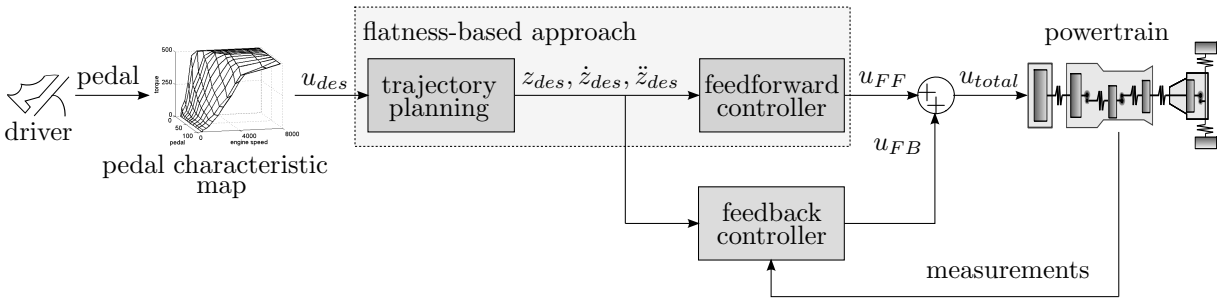

Figure 3.6: Control structure with driver, trajectory generation, feedforward and feedback controller.

the system state $\boldsymbol{x}$. In the following the i^{th} derivative of a function z is denoted as $z^{(i)}$. Flatness for a general nonlinear system is defined as follows:

Definition 2 ([FliessEtAl95])**.** *The nonlinear single-input/single-output (SISO) system*

$$\begin{aligned} \dot{\boldsymbol{x}} =& f\left(\boldsymbol{x}, u\right), \quad \boldsymbol{x}(0) = \boldsymbol{x}_0 \\ y =& h(\boldsymbol{x}) \end{aligned} \tag{3.40}$$

with $f(x)$ being a smooth vector field, $\boldsymbol{x} \in \mathbb{R}^n$ and $u, y \in \mathbb{R}$ is said to be differentially flat, if and only if there exists a flat output $z \in \mathbb{R}$, such that

- *the flat output z is a function of the state variables $\boldsymbol{x}$: $z = a(\boldsymbol{x})$,*
- *the system state, input and output can be parametrized with z and a final number of its derivatives:*

$$\begin{aligned} \boldsymbol{x} =& \Phi_x\left(z, \dot{z}, \ldots, z^{(n-1)}\right), \quad u = \Phi_u\left(z, \dot{z}, \ldots, z^{(n)}\right), \\ y =& \Phi_y\left(z, \dot{z}, \ldots, z^{(n-r)}\right), \end{aligned}$$

where r is the relative degree of the nonlinear SISO system (3.40)*.*

The whole system dynamics are given by the flat output and its derivatives. Thus, it follows that the system is inverted as the input u can be defined as a function of the flat output and its derivatives. Using differentially flatness theory and desired trajectories of the flat output and its derivatives $z_{des}, \dot{z}_{des}, \ldots, z_{des}^{(n)}$ set-point transitions can be designed with arbitrary transition time. The only restriction is the dynamics of the actuator.

As a load change is a set-point transition, a flatness based feedforward controller is derived for the linear two-mass control model in (3.12) and the three-mass control model in (3.27). For linear systems it is valid

Definition 3. *A linear system is a flat system if and only if the system is controllable.*

As shown for example in [Sira-RamírezAgrawal04] and [Zeitz10]. Therefore, in the following first controllability is demonstrated for the the two-mass and three-mass control models. Then, flat output, feedforward control law, and trajectory planning are derived.

3.4.1.1 Controllability

For a linear SISO time-invariant system defined by the state-space representation:

$$\dot{\boldsymbol{x}} = \boldsymbol{A}\boldsymbol{x}(t) + \boldsymbol{B}u(t), \quad y(t) = \boldsymbol{C}\boldsymbol{x}(t) + \boldsymbol{D}u(t), \quad \boldsymbol{x}(t) \in \mathbb{R}^n \tag{3.41}$$

the controllability matrix $\boldsymbol{P}$ is given as

$$\boldsymbol{P} = \begin{bmatrix} \boldsymbol{B} & \boldsymbol{A}\boldsymbol{B} & \boldsymbol{A}^2\boldsymbol{B} & \dots & \boldsymbol{A}^{n-1}\boldsymbol{B} \end{bmatrix}, \tag{3.42}$$

see for instance [Levine10] or [FranklinPowellEmami-Naeini15]. The linear system in (3.41) is controllable if and only if

$$\text{rank } \boldsymbol{P} = n. \tag{3.43}$$

Two-Mass Model

For the two-mass control model in (3.12), the system matrix $\boldsymbol{A}_2$ and input matrix $\boldsymbol{B}_2$ read

$$\boldsymbol{A}_2 = \begin{bmatrix} 0 & 1 \\ -\theta c & -\theta d \end{bmatrix}, \quad \boldsymbol{B}_2 = \begin{bmatrix} 0 \\ \frac{1}{J_1 R} \end{bmatrix}. \tag{3.44}$$

Therefore, the controllability matrix is given as

$$\boldsymbol{P}_2 = \begin{bmatrix} 0 & \frac{1}{J_1 R} \\ \frac{1}{J_1 R} & -\frac{\theta d}{J_1 R} \end{bmatrix}, \tag{3.45}$$

for $J_1, R \neq 0$. The two-mass control system is controllable if and only if

$$|\boldsymbol{P}_2| \neq 0, \tag{3.46}$$

which results in

$$-\frac{1}{J_1^2 R^2} \neq 0. \tag{3.47}$$

Therefore, for $J_1, R \neq 0$, which is always guaranteed, the controllability matrix $\boldsymbol{P}_2$ of the two-mass control system (3.12) is defined and the system is controllable.

Three-Mass Model

Next, the controllability of the three-mass system from Eq. 3.27 is verified. The system matrix $\boldsymbol{A}_3$ is given in Eq. (3.34). The control model of a hybrid electric powertrain has two control inputs, namely u_1 of the internal combustion engine and u_2 of the electric machine. The corresponding input matrices are

$$\boldsymbol{B}_{3,u_1} = \begin{bmatrix} 0 \\ 0 \\ \frac{1}{J_1} \\ 0 \end{bmatrix}, \tag{3.48}$$

and

$$\boldsymbol{B}_{3,u_2} = \begin{bmatrix} 0 \\ 0 \\ -\frac{1}{J_2} \\ \frac{1}{J_2 R} \end{bmatrix}. \tag{3.49}$$

The controllability matrices $\boldsymbol{P}_{3,u_1}$ and $\boldsymbol{P}_{3,u_2}$ of the three-mass model read

$$\boldsymbol{P}_{3,u_1} = \begin{bmatrix} \boldsymbol{B}_{3,u_1} & \boldsymbol{A}_3\boldsymbol{B}_{3,u_1} & \boldsymbol{A}_3^2\boldsymbol{B}_{3,u_1} & \boldsymbol{A}^3\boldsymbol{B}_{3,u_1} \end{bmatrix}, \tag{3.50}$$

and

$$\boldsymbol{P}_{3,u_2} = \begin{bmatrix} \boldsymbol{B}_{3,u_2} & \boldsymbol{A}_3\boldsymbol{B}_{3,u_2} & \boldsymbol{A}_3^2\boldsymbol{B}_{3,u_2} & \boldsymbol{A}^3\boldsymbol{B}_{3,u_2} \end{bmatrix}. \tag{3.51}$$

The full rank of the controllability matrix can be shown by the determinant of the matrix. If the determinant is unequal to zero, then the matrix has full rank. For input u_1 the determinant of controllability matrix $\boldsymbol{P}_{3,u_1}$ is given as

$$|\boldsymbol{P}_{3,u_1}| = -\frac{c_2\theta_2 d_1^2 - c_1 d_2 \theta_2 d_1 + c_1^2}{J_1^4 R^2 J_2^2}. \tag{3.52}$$

Hence, for

$$c_2\theta_2 d_1^2 - c_1 d_2 \theta_2 d_1 + c_1^2 \neq 0 \tag{3.53}$$

the three-mass control model is controllable with input u_1. For input u_2 the determinant of $\boldsymbol{P}_{3,u_2}$ is calculated numerically. Applying the parameters from Tab. 2.5 in controllability matrix (3.51), it follows $|\boldsymbol{P}_{3,u_2}| = -6.043e8$, which is unequal to zero. Thus, the investigated system is also controllable for input u_2 and therefore both inputs u_1 and u_2 can be used for control. However, for feedforward control design a SISO system is focused and the inputs are applied separately.

It follows that the linear two-mass and three-mass control models are controllable, therefore flat outputs for these systems exist and flatness-based feedforward control laws can be derived.

3.4.1.2 Flat Outputs and Feedforward Control Laws

The main challenge in flatness-based feedforward control design is to find a flat output z. When the flat output is found, the feedforward control law can be easily derived, as the flat output and its derivatives define system state, output and input completely.

In particular the concept of differentially flatness in the context of SISO linear time invariant systems is investigated for instance in [Sira-RamírezAgrawal04], [HagenmeyerZeitz09], and [Zeitz10].

For a linear SISO system as described in Eq. (3.41) the flat output z is given as a linear function of the system state

$$z = \boldsymbol{a}^T\boldsymbol{x}, \quad \boldsymbol{a} \in \mathbb{R}^n. \tag{3.54}$$

Further, the linear system (3.41) with flat output z necessarily needs to have relative degree $r = n$, which is equal to the system order. Therefore, the following equations must hold

$$\begin{aligned} z &= \boldsymbol{a}^T \boldsymbol{x} \\ \dot{z} &= \boldsymbol{a}^T \boldsymbol{A}\boldsymbol{x} + \underbrace{\boldsymbol{a}^T \boldsymbol{B}}_{=0} u \\ \ddot{z} &= \boldsymbol{a}^T \boldsymbol{A}^2 \boldsymbol{x} + \underbrace{\boldsymbol{a}^T \boldsymbol{A}\boldsymbol{B}}_{=0} u \\ z^{(3)} &= \boldsymbol{a}^T \boldsymbol{A}^3 \boldsymbol{x} + \underbrace{\boldsymbol{a}^T \boldsymbol{A}^2 \boldsymbol{B}}_{=0} u \\ &\vdots \\ z^{(n-1)} &= \boldsymbol{a}^T \boldsymbol{A}^{n-1} \boldsymbol{x} + \underbrace{\boldsymbol{a}^T \boldsymbol{A}^{n-2} \boldsymbol{B}}_{=0} u \\ z^{(n)} &= \boldsymbol{a}^T \boldsymbol{A}^n \boldsymbol{x} + \underbrace{\boldsymbol{a}^T \boldsymbol{A}^{n-1} \boldsymbol{B}}_{=\kappa \neq 0} u. \end{aligned} \tag{3.55}$$

It results in the condition

$$\boldsymbol{a}^T \underbrace{\begin{bmatrix} \boldsymbol{B} & \boldsymbol{A}\boldsymbol{B} & \boldsymbol{A}^2\boldsymbol{B} & \dots & \boldsymbol{A}^{n-2}\boldsymbol{B} & \boldsymbol{A}^{n-1}\boldsymbol{B} \end{bmatrix}}_{=\boldsymbol{P}} = \underbrace{\begin{bmatrix} 0 & 0 & 0 & \dots & 0 & \kappa \neq 0 \end{bmatrix}}_{=\boldsymbol{e}^T} \tag{3.56}$$

with $\kappa \in \mathbb{R}$ and unequal to zero.

Hence, the flat output can be constructed by the inverse controllability matrix $\boldsymbol{P}$ as

$$\boldsymbol{a}^T = \boldsymbol{e}^T \boldsymbol{P}^{-1}. \tag{3.57}$$

As a consequence the controllability matrix $\boldsymbol{P}$ must have full rank, which is equivalent to controllability.

The new coordinates $\boldsymbol{x}^*$ with the flat output and its derivatives are given by the transformation matrix $\boldsymbol{\phi}$ as

$$\underbrace{\begin{bmatrix} z \\ \dot{z} \\ \ddot{z} \\ \vdots \\ z^{(n-1)} \end{bmatrix}}_{=\boldsymbol{x}^*} = \underbrace{\begin{bmatrix} \boldsymbol{a}^T \\ \boldsymbol{a}^T\boldsymbol{A} \\ \boldsymbol{a}^T\boldsymbol{A}^2 \\ \vdots \\ \boldsymbol{a}^T\boldsymbol{A}^{n-1} \end{bmatrix}}_{=\boldsymbol{\phi}} \boldsymbol{x}. \tag{3.58}$$

From the last equation in (3.55) the feedforward control law is given as a function of the new coordinate $\boldsymbol{x}^*$:

$$u_{FF} = \frac{1}{\kappa} \left(z^{(n)} - \boldsymbol{a}^T \boldsymbol{A}^n \boldsymbol{\phi}^{-1} \boldsymbol{x}^* \right). \tag{3.59}$$

Using these general derivations, flat output and feedforward control law are calculated for the two-mass control model in (3.12) and three-mass control model in (3.27). In the following, it is assumed that the disturbance δ in these models is zero, for instance due to a disturbance compensation controller, which is further discussed in Sec. 3.4.3.

Two-Mass Model

For the two-mass control model in (3.12) the inverse controllability matrix reads

$$\boldsymbol{P}_2^{-1} = \begin{bmatrix} \theta J_1 dR & J_1 R \\ J_1 R & 0 \end{bmatrix}. \tag{3.60}$$

Choosing $\kappa_2 = \frac{1}{J_1 R}$ the flat output for the two-mass control model is given as

$$z_2 = x_1 = \Delta\varphi, \tag{3.61}$$

describing the torsion rotation angle between both inertias. The flat coordinates of the two-mass control model are

$$\boldsymbol{x}_2^* = \begin{bmatrix} z_2 \\ \dot{z}_2 \end{bmatrix} = \begin{bmatrix} \Delta\varphi \\ \Delta\omega \end{bmatrix}. \tag{3.62}$$

Hence, the coordinate transformation in section 3.1 already yields a flat system.

A feedforward control law of the two-mass control model in (3.12) reads

$$u_{FF,2}(t) = J_1 R \left(\ddot{z}_{2,des} + \theta c z_{2,des}(t) + \theta d \dot{z}_{2,des}(t) \right), \tag{3.63}$$

with desired trajectories $z_{2,des}(t), \dot{z}_{2,des}(t), \ddot{z}_{2,des}$.

Three-Mass Model

The same approach to find the flat output and derive a feedforward control law can be applied to the three-mass control model in (3.27). Only the last row of the inverse controllability matrix is relevant in order to construct the flat output. For input u_1, which is the torque of the internal combustion engine, the last row of the inverse controllability matrix of $\boldsymbol{P}_{3,u_1}$ reads

$$\boldsymbol{P}_{3,u_1}^{-1}(4,:) = \frac{1}{c_2 d_1^2 \theta_2 - c_1 d_1 d_2 \theta_2 + c_1^2} \begin{bmatrix} J_1 d_1^2, & J_1 J_2 R \left(c_1 - d_1 d_2 \theta_2 \right), & 0, & -J_1 J_2 d_1 R \end{bmatrix}. \tag{3.64}$$

The last row (4^{th}-row) is denoted as $(4,:)$.

Choosing

$$\kappa_{3,u1} = c_2 d_1^2 \theta_2 - c_1 d_1 d_2 \theta_2 + c_1^2, \tag{3.65}$$

the flat output for input u_1 is given as

$$z_{3,u1} = \boldsymbol{a}_{3,u1}^T \boldsymbol{x} = \boldsymbol{a}_{3,u1}^T \begin{bmatrix} \Delta\varphi_1, & \Delta\varphi_2, & \Delta\omega_1, & \Delta\omega_2 \end{bmatrix}^T \tag{3.66}$$

with

$$\boldsymbol{a}_{3,u1}^T = \begin{bmatrix} J_1 d_1^2, & J_1 J_2 R \left(c_1 - d_1 d_2 \theta_2 \right), & 0, & -J_1 J_2 d_1 R \end{bmatrix}, \tag{3.67}$$

as also derived in [PhamScholzSeifried17]. Therefore, the flat output is a linear combination of the torsion rotation angles and the torsion angular velocity of the two last moments of inertia.

The flat coordinates are

$$\boldsymbol{x}^*_{3,u1} = \begin{bmatrix} z_{3,u1} \\ \dot{z}_{3,u1} \\ \ddot{z}_{3,u1} \\ \dddot{z}_{3,u1} \end{bmatrix} \tag{3.68}$$

The transformation matrix $\boldsymbol{\phi}_{3,u1}$ can be calculated as given in Eq. (3.58). Hence, the feedforward control law of the three-mass control model with input u_1 is:

A feedforward control law for input u_1 of the three-mass control model in (3.27) reads

$$u_{FF,3,u1}(t) = \frac{1}{\kappa_{3,u1}} \left(z^{(4)}_{3,u1,des}(t) - \boldsymbol{a}^T_{3,u1} \boldsymbol{A}^4_3 \boldsymbol{\phi}^{-1}_{3,u1} \boldsymbol{x}^*_{\boldsymbol{3,u1,des}}(t) \right) \tag{3.69}$$

with desired trajectories $z^{(4)}_{3,u1,des}(t)$ and $\boldsymbol{x}^*_{\boldsymbol{3,u1,des}}(t)$.

The second input of the three-mass system is the torque of the electric machine. For this input a flat output and a feedforward control law can be also calculated. Compared to the first input vector $\boldsymbol{B}_{3,u1}$, the second input vector $\boldsymbol{B}_{3,u2}$ as given in Eq. (3.49) has one more element unequal to zero. Therefore, the analytical solution of the controllability matrix $\boldsymbol{P}_{3,u_2}$ is much more complex and the analytical derivation of the flat output and the feedforward control law is difficult. Thus, a numerical approach is more reasonable. Applying the parameters of the three-mass control model in Tab. 2.5, the flat output can be found using the law in (3.57). The resulting flat output is a linear combination of all four states $\Delta\varphi_1, \Delta\varphi_2, \Delta\omega_1, \Delta\omega_2$. Then, the feedforward control law can be calculated using the general feedforward control law in (3.59).

Remark

If the damping coefficients are neglected for feedforward control design $d_1 = d_2 = 0$, then the flat output can be constructed much easier. In general for a system with n mass-spring elements, input u_1 at the first mass and without damping the torsion rotation angle of the last two inertias $\Delta\varphi_{n-1}$ is always a flat output as shown in [PhamBushnell15]. Hence, for the three-mass control system with input u_1 it is valid that the torsion rotation angle of the last two inertias $z_3 = \Delta\varphi_2$ is a flat output. A further positive effect is that the transformation matrix of the undamped system can be much easier calculated. However, model uncertainty is introduced due to the simplification, but the error is relatively small as the original system is underdamped and the influence of damping is small, see the discussion in Sec. 3.2.

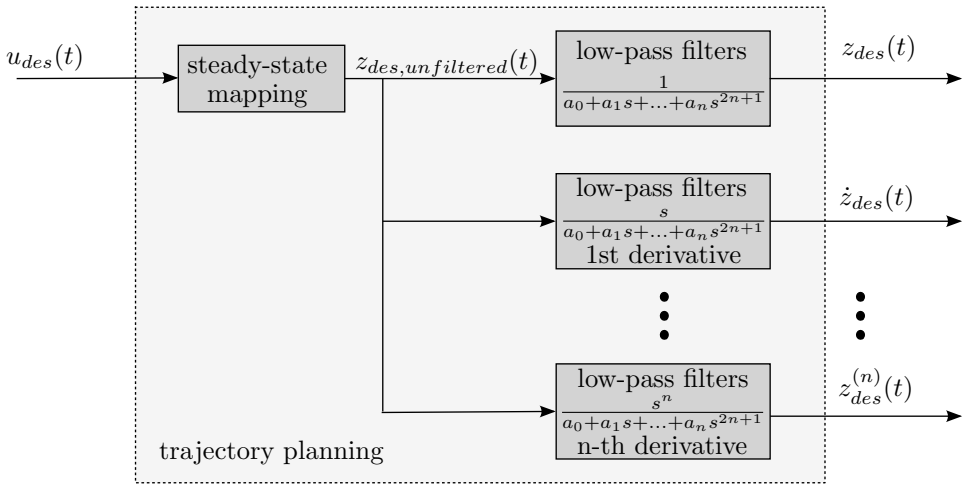

Figure 3.7: Trajectory planning of desired flat trajectories $z_{des}(t), \dot{z}_{des}(t), \ldots, z_{des}^{(n)}(t)$ generated by desired driver torque $u_{des}(t)$.

3.4.1.3 Trajectory Planning

The driver requests by the pedal position a desired drive torque u_{des} as illustrated in Fig. 3.6. When the desired torque u_{des} is applied directly to the powertrain, then driveline oscillations can occur, since the powertrain is underdamped. Hence, the desired torque is adapted by the flatness-based approach. The feedforward control laws derived in the previous section requires desired trajectories in coordinates of the flat output

$$\boldsymbol{x}_{des}^{*}(t) = \left[\begin{array}{cccc} z_{des}(t) & \dot{z}_{des}(t) & \ldots & z_{des}^{(n-1)}(t) \end{array} \right]^T, \tag{3.70}$$

and $z_{des}^{(n)}(t)$, see Eq. (3.58). Requirements on the desired trajectory $z_{des}(t)$ generation are

- real-time capability,
- n-times differentiable, as the feedforward control law, see Eq. (3.59) applies the n^{th} derivative of the flat output,
- start point t_0 and end point t_T of the desired trajectory must correspond to the desired steady-states of the system and all n derivatives have to be zero at the start and end point to get a smooth transition: $z_{des}^{(i)}(t)|_{t=\{t_0,t_T\}} = 0, \quad \text{for } i = 1, 2, \ldots, n.$

Figure 3.7 shows a trajectory planning approach with steady-state mapping and several low-pass derivative filters to obtain appropriate derivatives of the desired flat output trajectory. The unfiltered desired torque $u_{des}(t)$ of the driver is mapped on-line to the corresponding steady-state flat output $z_{des,unfiltered}(t) = z_{ss}$. This mapping ensures that start and end point are correct. The mapping depends on the system dynamic equations.

The steady-state mapping can be generally found using Eq. (3.59). In steady-state the flat coordinates are defined as

$$\boldsymbol{x}_{ss}^{*} = \begin{bmatrix} z_{ss} \\ 0 \\ \vdots \\ 0 \end{bmatrix} \tag{3.71}$$

with $z_{ss}^{(n)} = 0$. Therefore, it follows from Eq. (3.59)

$$u_{des} = -\frac{1}{\kappa}\boldsymbol{a}^{T}\boldsymbol{A}^{n}\phi^{-1}\boldsymbol{x}_{ss}^{*}. \tag{3.72}$$

As only the first entry of $\boldsymbol{x}_{ss}^{*}$ is interested, the first column of $\boldsymbol{\phi}^{-1}$ is relevant, which is denoted as $\phi^{-1}(:,1)$. Hence, it is

$$u_{des} = -\frac{1}{\kappa}\underbrace{\boldsymbol{a}^{T}\boldsymbol{A}^{n}\boldsymbol{\phi}^{-1}(:,1)}_{=:\gamma} z_{ss} \tag{3.73}$$

and thus the steady-state desired trajectory can be generally calculated by

$$z_{des,unfiltered}(t) = z_{ss} = -\frac{\kappa}{\gamma}u_{des}. \tag{3.74}$$

For the two-mass control model from Eq. (3.63) the steady state mapping from desired driver torque u_{des} to steady-state flat output $z_{ss} = z_{des,unfiltered}(t)$ is given trivially as

$$z_{des,unfiltered,2}(t) = \Delta\varphi_{ss} = \frac{1}{J_1 R\theta c}u_{des}, \quad \text{with } \Delta\dot{\varphi}_{ss} = \Delta\ddot{\varphi}_{ss} = 0. \tag{3.75}$$

For the three-mass control model from Eq. (3.27) there is a steady state mapping for the engine torque input u_1 as well as for the electric machine torque input u_2, which can be calculated in each case by applying Eq. (3.74).

After the steady-state mapping there are several low-pass filters. The low-pass filters $(2n+1)$-th order realize the numerical calculation of the derivatives of the desired trajectory and a smooth transition. There exist various types of low-pass filters. For instance a first-order low-pass filter can be connected in series, a Bessel filter with constant group delay or other filter types as Butterworth or Chebyshev filters can be applied. The appropriate filter type depends on the specification how the desired flat output trajectory $z_{des}(t)$ should be filtered. An alternative to the derivative filters are planned trajectories as for example discussed in [PiazziVisioli01] or [GraichenHagenmeyerZeitz05]. The trajectories can be designed, for instance by polynomials, such that the conditions n-times differentiable and feasible start and end points are fulfilled. In this thesis low-pass filters connected in a series are applied, due to the simple realization of the filters and the low requirements on the trajectory shape.

3.4.2 Feedback Control

The flatness-based feedforward controllers require accurate model parameters and no disturbances. The more inexact the parameters are and larger the disturbances, the worse the damping behavior is. Therefore, a feedback controller is necessary to deal with these uncertainties. The overall control loop shown in Fig. 3.8 illustrates the additional feedback controller u_{FB}. The goal of a feedback controller is to ensure a behavior closely to critically damped and to control both transient and steady-state behavior, as discussed in Sec. 3.3. A significant advantage of the flatness-based control approach is that reference trajectories for all states are generated by the feedforward controller and can be used in feedback control.

3.4.2.1 Pole-Placement

A pole-placement or an optimal control approach can be applied to regulate the whole error state vector

$$\boldsymbol{e} = \boldsymbol{x}^* - \boldsymbol{x}^*_{des}, \tag{3.76}$$

as discussed for instance in [Sira-RamírezAgrawal04]. The pole-placement approach allows to choose the closed loop poles of the error dynamics directly such that the damping behavior is critically damped. In the following the error dynamics is derived. For the undisturbed linear system from Eq. (3.41) it is valid

$$\dot{\boldsymbol{x}}^*_{des} = \boldsymbol{A}\boldsymbol{x}^*_{des} + \boldsymbol{B}u_{FF}, \tag{3.77}$$

as the system is fully inverted by the flatness-based approach. Secondly, the closed loop system dynamics is given as

$$\dot{\boldsymbol{x}} = \boldsymbol{A}\boldsymbol{x} + \boldsymbol{B}\left(u_{FF} + u_{FB}\right). \tag{3.78}$$

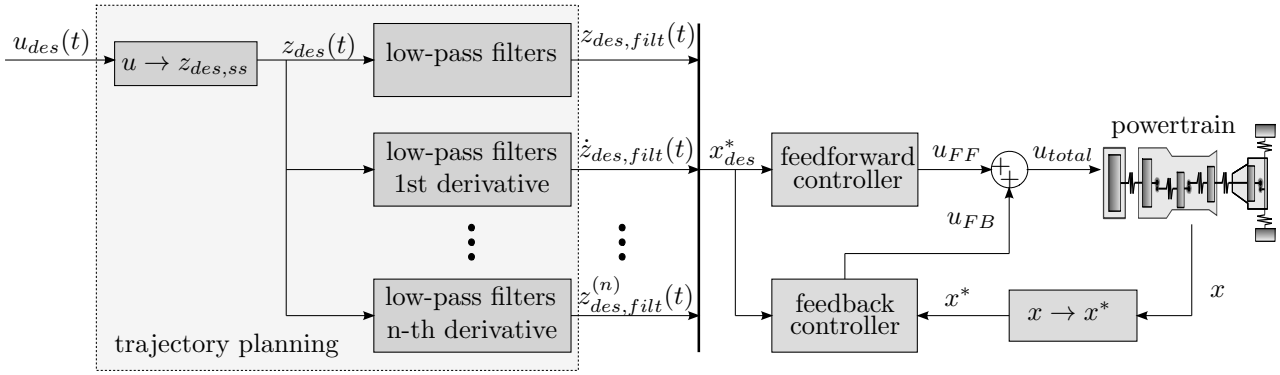

Figure 3.8: Overall control loop with trajectory planning, feedforward controller, and state feedback controller.

Furthermore, the state feedback controller of the error state is defined as

$$u_{FB} = -\boldsymbol{k}^T \left(\boldsymbol{x}^* - \boldsymbol{x}^*_{des}\right) \tag{3.79}$$

with control gain $\boldsymbol{k}^T$. The flat state vector $\boldsymbol{x}^*$ can be obtained by the transformation in (3.58). Applying (3.79) in (3.78), it follows

$$\dot{\boldsymbol{x}} = \boldsymbol{A}\boldsymbol{x} + \boldsymbol{B}\left(u_{FF} - \boldsymbol{k}^T \left(\boldsymbol{x}^* - \boldsymbol{x}^*_{des}\right)\right). \tag{3.80}$$

Finally, the error dynamics is obtained by subtracting Eq. (3.77) from Eq. (3.80):

$$\dot{\boldsymbol{x}} - \dot{\boldsymbol{x}}^*_{des} = \left(\boldsymbol{A} - \boldsymbol{B}\boldsymbol{k}^T\right)\left(\boldsymbol{x}^* - \boldsymbol{x}^*_{des}\right), \tag{3.81}$$

which yields

$$\dot{\boldsymbol{e}} = \left(\boldsymbol{A} - \boldsymbol{B}\boldsymbol{k}^T\right)\boldsymbol{e}. \tag{3.82}$$

Hence, the control gain $\boldsymbol{k}^T$ has to be chosen for the closed loop matrix $\left(\boldsymbol{A} - \boldsymbol{B}\boldsymbol{k}^T\right)$ to guarantee that the state trajectories $\boldsymbol{x}^*$ exponentially converges towards the reference trajectories $\boldsymbol{x}^*_{des}$. There are several methods to calculate the control gain $\boldsymbol{k}^T$. Pole-placement and optimal control methods are for instance presented in [WilliamsLawrence07], and [Kirk12].

3.4.2.2 Output Controller

On the other hand an output controller as a proportional–integral–derivative controller can be applied to control just the output y. Applying a proportional controller, the damping behavior can be directly influenced with proportional gain k_p. The proportional control law reads

$$u_{FB} = -k_p \left(y - y_{des}\right). \tag{3.83}$$

The desired output y_{des} is given by the transformation matrix in (3.58). In general it is

$$\boldsymbol{x}_{des} = \phi^{-1}\boldsymbol{x}^*_{des}. \tag{3.84}$$

Hence, for the desired output it is valid

$$y_{des} = c^T\phi^{-1}\boldsymbol{x}^*_{des}. \tag{3.85}$$

It is reasonable to choose the torsion angular velocity as system output as it is desired to influence the damping behavior of the system. Additionally, the rotation speeds of the powertrain are often available in measurements.

Two-Mass Model

For the two-mass control model in (3.12) the output

$$y = \Delta\omega = \frac{1}{R}\omega_1 - \omega_2 \tag{3.86}$$

is chosen. The closed loop dynamics of the two-mass control model (3.12) with feedback controller (3.83) and output (3.86) is given as

$$\Delta\dot{\omega} + \Theta c \Delta\varphi + \Theta d \Delta\omega + \frac{1}{J_1 R} k_p \left(y - y_{des}\right) - \frac{1}{J_2}\delta = 0. \tag{3.87}$$

As the disturbance δ is assumed as nearly constant and not as a function of the system states and the reference trajectory y_{des} is also not a function of the system states the closed loop dynamics is described by

$$\Delta\dot{\omega} + \Theta c \Delta\varphi + \underbrace{\left(\Theta d + \frac{1}{J_1 R} k_p\right)}_{=d_{total}} \Delta\omega = 0. \tag{3.88}$$

Therefore, the total damping parameter d_{total} of the two-mass control model can be increased by a proportional gain $k_p > 0$. Furthermore, if the desired damping ratio is set to critically damped, the resulting control gain $k_{p,crit}$ can be derived. The damping ratio of the controlled system ξ_p is defined by

$$\xi_p = \frac{\Theta d + \frac{1}{J_1 R} k_p}{2\sqrt{c\Theta}} \tag{3.89}$$

and for $\xi = 1$ the required proportional gain reads

$$k_{p,crit} = J_1 R \left(2\sqrt{c\Theta} - \Theta d\right). \tag{3.90}$$

Three-Mass Model

For the three-mass control model in (3.27) the output

$$y = \Delta\omega_2 = \frac{1}{R}\omega_2 - \omega_3 \tag{3.91}$$

is selected. Thus, the output is motivated by the maximal displacement of the first eigenvector with the lowest eigenfrequency of the detailed hybrid electric powertrain model as illustrated in Fig. 2.18.

The three-mass system has two inputs u_1 and u_2. In order to show which input is more suitable for feedback control, the closed loop system of each input is calculated. The feedback controller u_{FB} in (3.83) with output $\Delta\omega_2$ from (3.91) is applied to the system

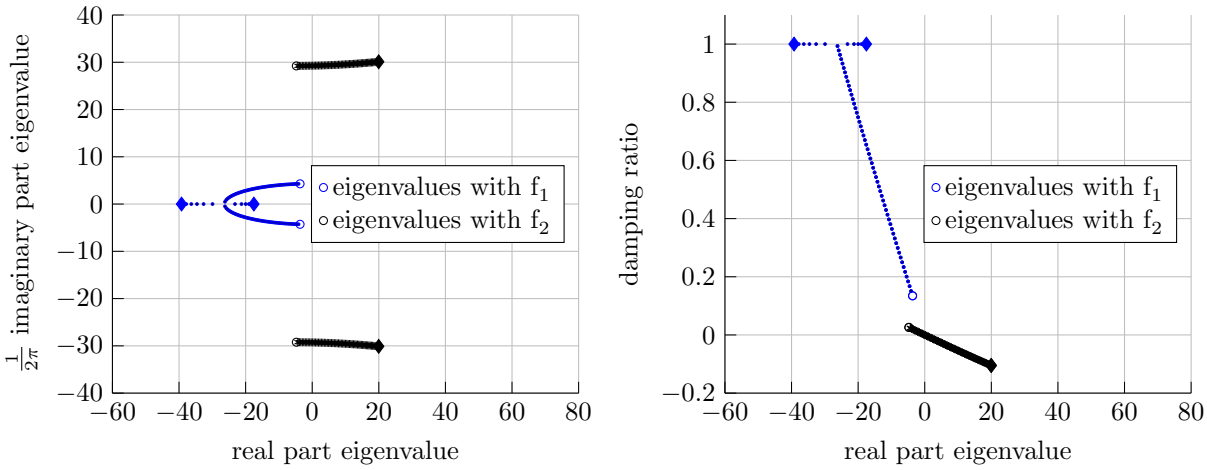

Figure 3.9: Pole locations and damping behavior of closed loop matrix $\boldsymbol{A}_{3,cl,u_1}$ with input u_1 and varying proportional gain k_p from 0 to 300.

and the input vectors $\boldsymbol{B}_{3,u_1}$ and $\boldsymbol{B}_{3,u_2}$ from (3.48) and (3.49) are used. For the first input u_1 the closed loop system matrix $\boldsymbol{A}_{3,cl,u_1}$ reads

$$\boldsymbol{A}_{3,cl,u_1} = \begin{bmatrix} 0 & 0 & 1 & 0 \\ 0 & 0 & 0 & 1 \\ -c_1\Theta_1 & \frac{c_2}{J_2R} & -d_1\Theta_1 & \frac{d_2}{J_2R} - \frac{k_p}{J_1} \\ \frac{c_1}{J_2R} & -c_2\Theta_2 & \frac{d_1}{J_2R} & -d_2\Theta_2 \end{bmatrix}. \tag{3.92}$$

Further, the closed loop system matrix $\boldsymbol{A}_{3,cl,u_2}$ of input u_2 is given as

$$\boldsymbol{A}_{3,cl,u_2} = \begin{bmatrix} 0 & 0 & 1 & 0 \\ 0 & 0 & 0 & 1 \\ -c_1\Theta_1 & \frac{c_2}{J_2R} & -d_1\Theta_1 & \frac{d_2}{J_2R} + \frac{k_p}{J_2} \\ \frac{c_1}{J_2R} & -c_2\Theta_2 & \frac{d_1}{J_2R} & -d_2\Theta_2 - \frac{k_p}{J_2R} \end{bmatrix}. \tag{3.93}$$

The impact of each feedback controller can be clarified by varying the proportional gain k_p. Here, the proportional gain is varied from 0 to 300 for each input u_1, u_2. The resulting locations of the closed loop poles and the damping characteristics are calculated. The three-mass system is simulated with parameters from Tab. 2.5. Figure 3.9 shows the locations of the poles of closed loop matrix $\boldsymbol{A}_{3,cl,u_1}$. The same applies to Fig. 3.10 with input u_2 and closed loop matrix $\boldsymbol{A}_{3,cl,u_2}$.

The locations of the eigenvalues with proportional gain $k_p = 0$ are marked with a circle and the eigenvalues with proportional gain $k_p = 300$ are marked with a filled diamond. On the left the imaginary parts of the eigenvalues are factorized by $\frac{1}{2\pi}$ in order to visualize the frequencies of the eigenvalues. On the x-axis the real parts of the eigenvalues are displayed to show the stability of the eigenvalues. On the right side the damping ratios as defined in (3.38) are illustrated against the real parts of the eigenvalues.

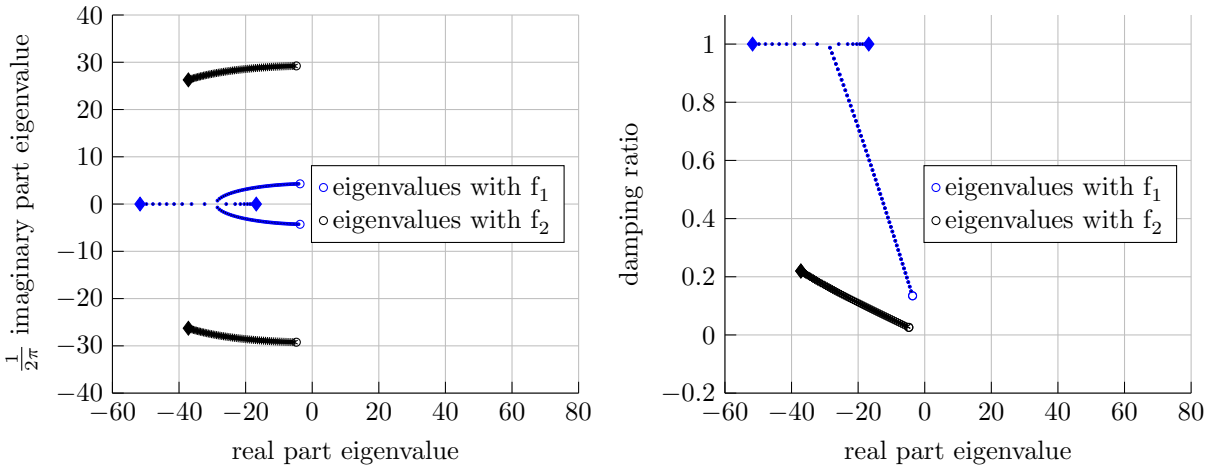

Figure 3.10: Pole locations and damping behavior of closed loop matrix $\boldsymbol{A}_{3,cl,u_2}$ with input u_2 and varying proportional gain k_p from 0 to 300.

As shown in Fig. 3.9 the poles of the frequency f_2 can become unstable for large proportional gains k_p. For this system proportional gains $k_p \geq 53.6$ makes the system unstable. On the other hand the damping ratio of the lowest frequency f_1 increases for larger proportional gains. Therefore, the damping behavior of the poles with f_1 cannot be independently increased with respect to a stable system using input u_1 and output $\Delta\omega_2$.

Contrary, when input u_2 is used. Figure 3.10 shows that the eigenvalues do not become unstable for large proportional gain k_p to 300. Therefore, increasing the proportional gain the damping ratio of the eigenvalues with f_1 becomes 1 for $k_p = 260$ and the system damping is critically damped. For greater k_p the system is overdamped. In the following, input u_2 is used for feedback control of a three-mass system.

In general, using an output controller as a proportional controller can be restrictive and it is possible that the desired damping behavior cannot be fulfilled. However, the method is simple to apply and only measurable states are used. On the other hand more advanced methods as pole-placement or optimal control approaches allows to better meet the desired damping behavior. The disadvantage here is that the whole system state has to be available, for example by state estimation. Furthermore, the control design is not as intuitive as it is for output controller. Therefore, an output controller is applied hereafter.

3.4.3 Disturbance Rejection

The two-mass control model in (3.12) and three-mass control model in (3.27) include a disturbance term with disturbance δ. The feedforward and feedback control design in the previous sections assume this disturbance to be zero or compensated to zero. In the following the estimation and compensation of the disturbance is discussed.

3.4.3.1 Disturbance Estimation

The disturbance, which act on the powertrain, consists usually of rolling resistance, road inclination and air resistance. Usually, the main part of the disturbance is the road inclination especially for low vehicle velocity, since rolling and wind disturbance are a function of the velocity. Therefore, for disturbance estimation the assumption is made that the disturbance is constant. The constant disturbance dynamics is described by

$$\dot{\delta} = 0, \quad \delta(0) = \delta_0. \tag{3.94}$$

The disturbance dynamics equations can be added to the dynamics equations of the two-mass control model in (3.12) and the three-mass control model in (3.27). The system states are augmented to $\boldsymbol{x}_{2,augm} = [\Delta\varphi, \Delta\omega, \delta]^T$, and $\boldsymbol{x}_{3,augm} = [\Delta\varphi_1, \Delta\varphi_2, \Delta\omega_1, \Delta\omega_2, \delta]^T$, respectively. The augmented system matrices read

$$\boldsymbol{A}_{2,augm} = \begin{bmatrix} 0 & 1 & 0 \\ -c\Theta & -d\Theta & \frac{1}{J_2} \\ 0 & 0 & 0 \end{bmatrix}, \tag{3.95}$$

and

$$\boldsymbol{A}_{3,augm} = \begin{bmatrix} 0 & 0 & 1 & 0 & 0 \\ 0 & 0 & 0 & 1 & 0 \\ -c_1\Theta_1 & \frac{c_2}{J_2 R} & -d_1\Theta_1 & \frac{d_2}{J_2 R} & 0 \\ \frac{c_1}{J_2 R} & -c_2\Theta_2 & \frac{d_1}{J_2 R} & -d_2\Theta_2 & \frac{1}{J_3} \\ 0 & 0 & 0 & 0 & 0 \end{bmatrix}. \tag{3.96}$$

However, when the torsion angular velocity $\Delta\omega$ of the two-mass model and the velocities $\Delta\omega_1, \Delta\omega_2$ of the three-mass model are measured, the output matrices read

$$\boldsymbol{C}_{2,augm} = \begin{bmatrix} 0 & 1 & 0 \end{bmatrix}, \tag{3.97}$$

and

$$\boldsymbol{C}_{3,augm} = \begin{bmatrix} 0 & 0 & 1 & 0 & 0 \\ 0 & 0 & 0 & 1 & 0 \end{bmatrix}. \tag{3.98}$$

It follows that the systems are not observable, when the pairs $(\boldsymbol{A}_{2,augm}, \boldsymbol{C}_{2,augm})$ and $(\boldsymbol{A}_{3,augm}, \boldsymbol{C}_{3,augm})$ are investigated. Hence, another system representation is needed.

In [JoachimHorwathReuss08] a modified two-mass powertrain model without elasticity is divided into a primary and secondary part as depicted in Fig. 3.11. In a first step the drive shaft torque $T_{ds,R}$ with ratio is estimated. The drive shaft torque is assumed to be nearly constant. The dynamics equations of the first primary part read

$$\begin{bmatrix} \dot{\omega}_1 \\ \dot{T}_{ds,R} \end{bmatrix} = \underbrace{\begin{bmatrix} 0 & -\frac{1}{J_1} \\ 0 & 0 \end{bmatrix}}_{=:\boldsymbol{A}_{2,prim}} \begin{bmatrix} \omega_1 \\ T_{ds,R} \end{bmatrix} + \begin{bmatrix} \frac{1}{J_1} \\ 0 \end{bmatrix} u \tag{3.99}$$

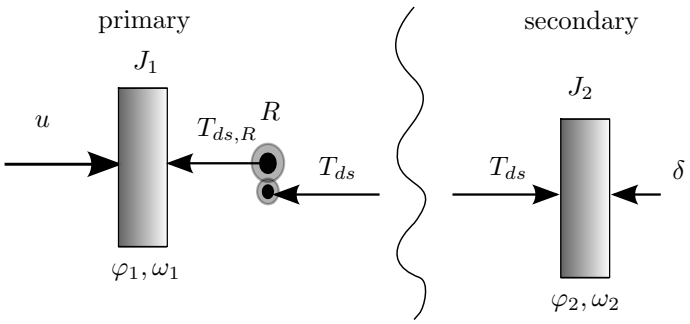

Figure 3.11: Divided two-mass control model into primary and secondary part with drive shaft torque T_{ds}.

with system state $\boldsymbol{x}_{prim} = \begin{bmatrix} \omega_1, & T_{ds,R} \end{bmatrix}^T$. The corresponding output matrix is given as $\boldsymbol{C}_{2,prim} = \begin{bmatrix} 1, & 0 \end{bmatrix}^T$. The pair $(\boldsymbol{A}_{2,prim}, \boldsymbol{C}_{2,prim})$ is observable. Therefore, for example a Luenberger observer, as used here, can be designed to estimate the drive shaft state $T_{ds,R}$. Then, the corresponding drive shaft torque with considered gear ratio is given as

$$T_{ds} = RT_{ds,R}. \tag{3.100}$$

Now, the secondary part is used to estimate the disturbance δ. The dynamics is given as

$$\begin{bmatrix} \dot{\omega}_2 \\ \dot{\delta} \end{bmatrix} = \underbrace{\begin{bmatrix} 0 & -\frac{1}{J_2} \\ 0 & 0 \end{bmatrix}}_{=:\boldsymbol{A}_{2,sec}} \begin{bmatrix} \omega_2 \\ \delta \end{bmatrix} + \begin{bmatrix} \frac{1}{J_2} \\ 0 \end{bmatrix} T_{ds}. \tag{3.101}$$

The system state is defined as $\boldsymbol{x}_{sec} = \begin{bmatrix} \omega_2, & \delta \end{bmatrix}^T$ and the output matrix is similar to the primary part $\boldsymbol{C}_{2,sec} = \boldsymbol{C}_{2,prim}$. Similar to the primary part, an observer can be designed for the secondary part to predict the disturbance δ.

The prediction method of [JoachimHorwathReuss08] can also be transferred to a three-mass control model. For this, the three-mass control model is simplified to a static two-mass control model as illustrated in Fig. 3.12. The first and second moment of inertia are summarized to $J_1 + J_2$ and the input torque to $u_1 + u_2$. It is assumed that the rotation angles φ_1, φ_2, and angular velocities ω_1, ω_2 are equal. Then, the same Eq. (3.99) and (3.101) can be stated for the three-mass static control model in order to estimate the disturbance δ.

3.4.3.2 Disturbance Compensation

A compensation torque input u_c can be designed, when the disturbance δ is known. The objective is to ensure that the acceleration of the vehicle is not affected by disturbances, for example road inclination, using a compensation torque. Therefore, the detailed two-mass

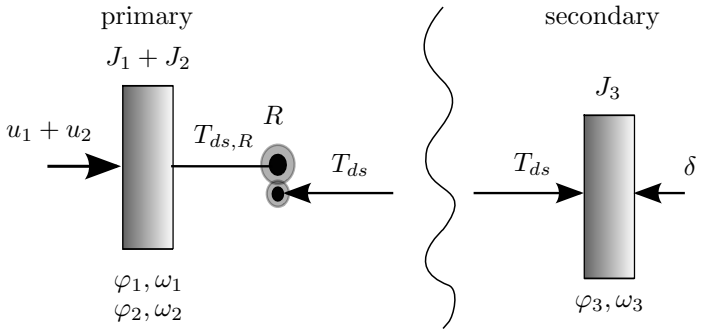

Figure 3.12: Separated three-mass control model in primary and secondary part with drive shaft torque T_{ds}.

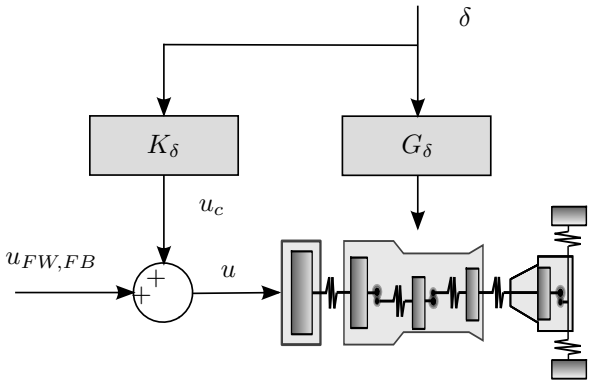

Figure 3.13: Feedforward disturbance compensation.

and three-mass control models representations defined in (3.1) and (2.25) are suitable for disturbance compensation as they represent velocities explicitly in the system states. In Remark 1 it is shown why the reduced models are not appropriate.

A feedforward disturbance compensation controller as discussed for instance in [Lunze12] is designed to compensate disturbance δ such that wheel velocity ω_2 of the two-mass control model (3.1) and wheel velocity ω_3 of three-mass control model (2.25), respectively, are not affected by the disturbance. Figure 3.13 illustrates the feedforward compensation approach with additive disturbance correction input u_c.

Following for instance [Lunze12], the calculation of the compensation controller K_δ is derived for the two-mass and three-mass control models. The system output is defined as the wheel velocity, since the goal of the disturbance compensator is to ensure that this velocity is not affected. For the two-mass model the system output is given as

$$y = \omega_2, \tag{3.102}$$

and for the three-mass model it is

$$y = \omega_3. \tag{3.103}$$

Furthermore, the required transfer functions from input u to output y $G_{\delta \to y}$ and from

disturbance δ to output y $G_{u\to y}$ are calculated using the linear system equations (3.1), and (3.25), respectively.

It is valid

$$y = G_{u\to y}\left(u_{FW,FB} + u_c\right) + G_\delta \delta, \tag{3.104}$$

which is

$$y = G_{u\to y} u_{FW,FB} + G_{u\to y} K_\delta \delta + G_\delta \delta. \tag{3.105}$$

Hence, for

$$K_\delta = -G_{u\to y}^{-1} G_\delta \tag{3.106}$$

the disturbance δ is canceled.

The difficulty is that K_δ is usually not causal. Therefore a low-pass filter with appropriate system order can be added in series to make K_δ realizable or the steady-state gain

$$K_{\delta,ss} = -G_{u\to y}^{-1}(0) G_\delta(0) \tag{3.107}$$

is applied.

Remark 1

In the following it is shown, why the reduced control models (3.12) and (3.27) are not appropriate for disturbance rejection.

First, the compensation control inputs u_c for the two-mass and three-mass control model are derived. The dynamics equations of the two-mass control model read

$$\begin{aligned} \Delta\dot{\varphi} &= \Delta\omega \\ \Delta\dot{\omega} &= -\Theta c \Delta\varphi - \Theta d \Delta\omega + \frac{1}{J_1 R} u_c + \frac{1}{J_2}\delta \end{aligned} \tag{3.108}$$

with $\Theta = \frac{J_1 R^2 + J_2}{J_1 J_2 R^2}$. Applying the compensation input

$$u_c = -\frac{J_1 R}{J_2}\delta \tag{3.109}$$

the disturbance δ would be canceled.

The three-mass control model has two inputs u_1 and u_2. Both inputs are used for compensation. Hence, the dynamics equations of the three-mass control model with compensation inputs $u_{c,1}$ and $u_{c,2}$ read

$$\begin{aligned} \Delta\dot{\varphi}_1 &= \Delta\omega_1 \\ \Delta\dot{\varphi}_2 &= \Delta\omega_2 \\ \Delta\dot{\omega}_1 &= -\Theta_1 c_1 \Delta\varphi_1 - \Theta_1 d_1 \Delta\omega_1 + \frac{1}{J_2 R} c_2 \Delta\varphi_2 + \frac{1}{J_2 R} d_2 \Delta\omega_2 + \frac{1}{J_1} u_{c,1} - \frac{1}{J_2} u_{c,2} \\ \Delta\dot{\omega}_2 &= \frac{1}{J_2 R} c_1 \Delta\varphi_1 + \frac{1}{J_2 R} d_1 \Delta\omega_1 - \Theta_2 c_2 \Delta\varphi_2 - \Theta_2 d_2 \Delta\omega_2 + \frac{1}{J_2 R} u_{c,2} + \frac{1}{J_3}\delta \end{aligned} \tag{3.110}$$

with $\Theta_1 = \frac{J_1+J_2}{J_1 J_2}$ and $\Theta_2 = \frac{J_2 R^2+J_3}{J_2 J_3 R^2}$. The compensation inputs

$$u_{c,1} = -\frac{J_1 R}{J_3}\delta, \quad u_{c,2} = -\frac{J_2 R}{J_3}\delta \tag{3.111}$$

would compensate disturbance δ.

Now, it can be shown that the compensation inputs reduce the vehicle acceleration for $\delta > 0$. When the compensation laws Eq. (3.109) and (3.111) are examined in detail, it follows that for positive disturbance $\delta > 0$, the necessary compensation torque u_c and $u_{c,1}, u_{c,2}$, respectively, are negative. Hence, the total input torque is reduced, and therefore also the acceleration of the vehicle. This follows from the effect that the compensation laws Eq. (3.109) and (3.111) of the reduced models ensure that the torsion rotation angles and angular velocities are not affected by the disturbance. Thus, this behavior is not suitable.

Remark 2

There are situations in which disturbance cannot be compensated. For instance, when the drive unit is driving at the full-load curve and no compensation torque is available. Then the steady-state calculation of the flatness-based feedforward controller (3.74) is not right anymore and the approach has to consider the disturbance. However, in this work it is assumed that the disturbance can be compensated.

3.5 Applications

In this section simulation and experimental results are shown. The simulations are run with the control and detailed powertrain models of conventional, hybrid electric, and battery electric powertrains, presented in Chapter 2. The experimental results are done with a conventional test vehicle and with a battery electric test vehicle with electric front and rear axle. The applications demonstrate the uncontrolled oscillation behavior by measurements and that by the developed control strategy all desired specifications

- critically damped,
- independent transition time,
- and controlled transient behavior

can be reached.

Measurement: Uncontrolled Behavior

Figure 3.14 shows measurement data of an uncontrolled race-start, which is an extreme launching, of a conventional powertrain. In the beginning the engine torque T_{ICE} increases and decreases in order to hold a desired high engine rotation speed to enable a race-start. At time t_0 the clutch is closed by increasing the torque clutch T_{clutch}. On the right in Fig. 3.15, measurement data of an uncontrolled load change of a battery electric test vehicle is depicted. The torque of the electric machine T_{EM} increases to a desired torque.

Based on the fact that no controller is applied, in both figures high driveline oscillation amplitudes and a long decay time in the vehicle acceleration signal a_{VEH} are present. Furthermore, in Fig. 3.15 the wheels start to spin due to the excitation of the high electric machine torque, as it can be identified by an amplifying vehicle acceleration signal. These measurements show clearly the need for driveline control.

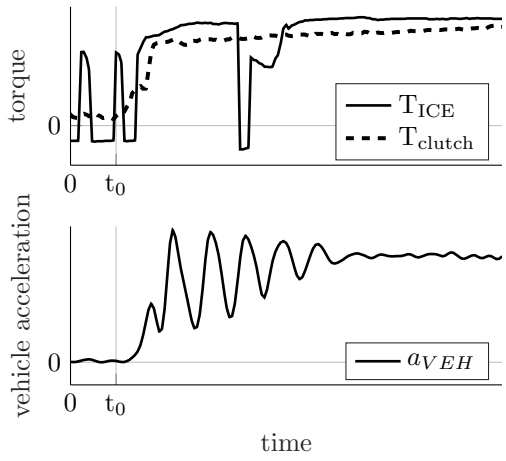

Figure 3.14: Measurement of an uncontrolled launching.

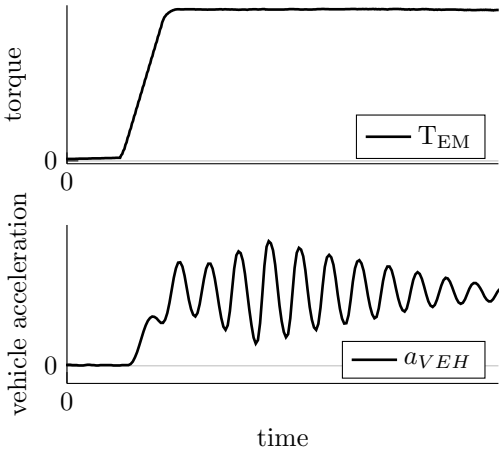

Figure 3.15: Measurement of an uncontrolled load change via an electric rear axle.

Simulation Using Control Models: Flatness-Based Feedforward Controller

The feedforward control approach as presented in Sec. 3.4.1 enables a set-point transition, as launching and load change, without oscillations, if the system dynamics is fully known. Therefore set-point transitions with various transition times $\Delta t = \{0.05\ s, 0.1\ s, 0.2\ s\}$ are simulated using the battery electric powertrain two-mass control model as described in (2.29) with parameters from Tab. 2.7 to validate the approach. For trajectory generation five low-pass filters in a row, each with a time constant of $T = 0.002$, are applied.

Figure 3.16 shows when the feedforward controller is applied, absolutely no driveline

oscillations occur regardless of the transition time. Hence, a significant better command response is given compared to the uncontrolled simulation or the ramps with varied transition time shown in Fig. 3.5. The feedforward control input requires larger absolute torques and high gradients, when the transition time is smaller. Therefore, the minimum feasible transition time depends on the available maximum absolute torque and the possible torque rate.

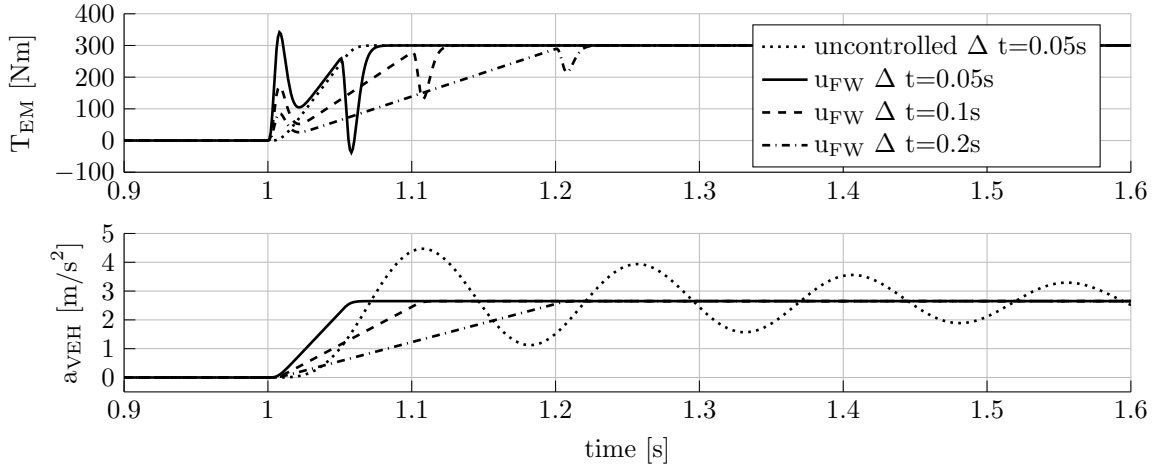

Figure 3.16: Simulation of load changes of the battery electric powertrain two-mass control model using flatness-based feedforward controllers with various transition times.

Simulation Using Detailed Model: Feedforward and Feedback Controller

The described detailed simulation models in Chapter 2 differ from the control models as they consider more degrees of freedom, nonlinear characteristics, and disturbances. A flatness-based feedforward controller designed by a control model cannot guarantee vibration free set-point transitions using the detailed simulation model. A feedback controller has to be applied to compensate these model uncertainties and disturbances.

The detailed hybrid electric powertrain model from Sec. 2.3.1 is applied to simulate a set-point transition via the first input u_1, the internal combustion engine, with flatness-based feedforward control based on the three-mass control model in Eq. (3.27). The second input u_2, the electric machine, is used for proportional feedback control. A road inclination of 5 % is additionally added to rolling and air resistance. The following control methods are simulated to illustrate the effects of the different feedback control methods:

- a) flatness-based feedforward controller as described in Sec. 3.4.1 without feedback control

- b) flatness-based feedforward controller as described in Sec. 3.4.1 and proportional output feedback controller with steady-state reference $y_{des} = 0$ as described in Sec. 3.4.2

- c) flatness-based feedforward controller as described in Sec. 3.4.1 and proportional output feedback controller with desired trajectory $y_{des}(t)$ as described in Sec. 3.4.2

The results are depicted in Fig. 3.17.

The simulated set-point transition using method a) shows some small remaining driveline oscillations in the vehicle acceleration signal a_{VEH} due to unmodeled dynamics and uncertainties. On the other hand, method b) has no driveline oscillations, but the dynamics is significantly reduced because of the steady-state feedback controller. Method c) shows no driveline oscillations and at the same time no performance reduction. The proportional feedback control gain is calculated such that the system is critically damped. Furthermore, the advantage of method c) using feedback control with a desired trajectory appears clearly in Fig. 3.18 showing actual and desired torsion angular velocity $\Delta\omega_2$ and $\Delta\omega_{2,des}$. The desired trajectory $\Delta\omega_{2,des}$ during the transition time ($1\ s \leq t \leq 1.15\ s$) is not zero, as it can be seen in the signal of method c). It is calculated in the flatness-based approach using the desired flat output from Eq. (3.74), its derivatives and the transformation matrix (3.58). Then, the feedback control method of c) is given as

$$u_{FB} = -k_p \left(\Delta\omega_2 - \Delta\omega_{2,des}\right) \tag{3.112}$$

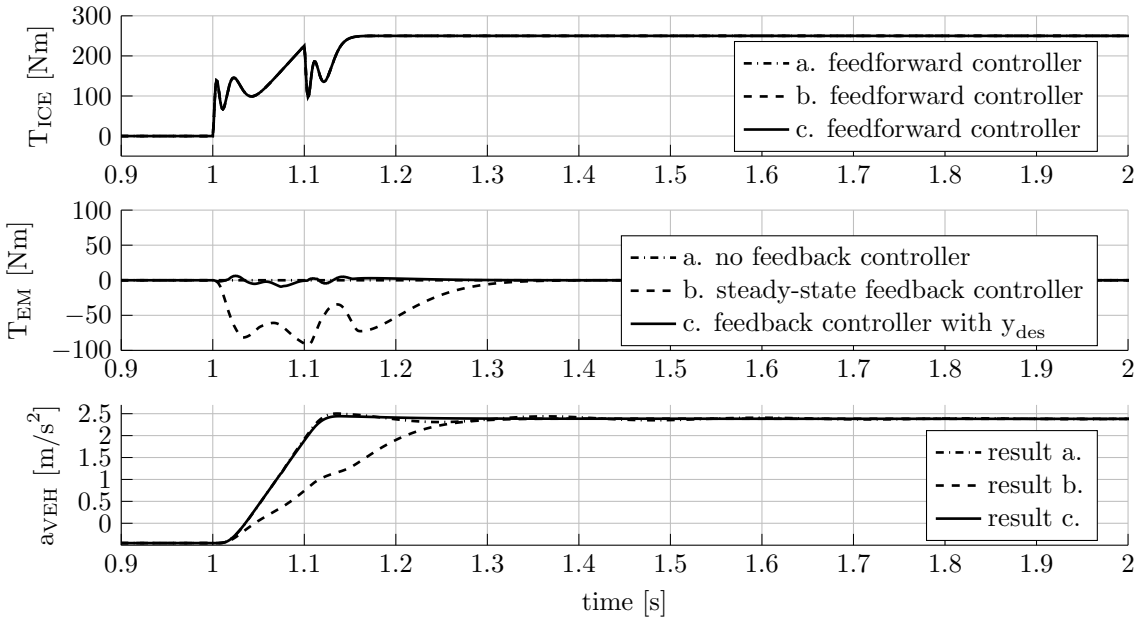

Figure 3.17: Simulation of load changes of the detailed hybrid electric powertrain model using flatness-based feedforward controllers and various feedback controller.

and therefore considers the transient behavior with $\Delta\omega_{2,des}$ in contrast to the steady-state controller method b. with

$$u_{FB,ss} = -k_p \left(\Delta\omega_2 - 0\right). \tag{3.113}$$

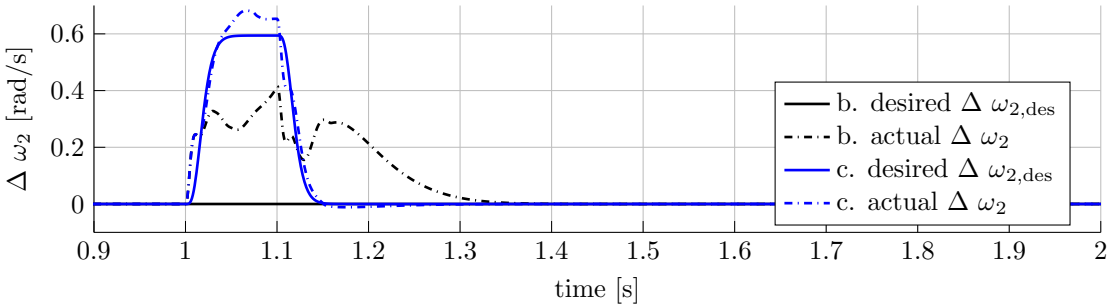

Figure 3.18: Simulation of desired and actual values of the torsion angular velocity between electric machine and wheels.

Measurement: Feedforward and Feedback Controller

Two control methods are implemented to a battery electric test vehicle with electric front and rear axles. The first method is the previously presented method c) and the second method is a proportional steady-state feedback controller without feedforward controller, which is defined as method d). Method d) is a simple controller and common in driveline control. The feedforward controller and the proportional feedback controller with desired trajectory of method c) are implemented to each axle of the electric vehicle. Figure 3.19 shows the better performance and higher comfort in the vehicle acceleration signal using method c) in contrast to using method d) by less vehicle vibration and faster transition. Furthermore, the experiment demonstrate that method c) is also suitable for an electric four-wheel drive vehicle.

Simulation Using Detailed Model: Disturbance Rejection

The simulations in Sec. 3.5 using the detailed hybrid electric powertrain model include disturbances. The sum of these disturbances, rolling resistance, air resistance and road inclination, reduces the vehicle acceleration in these simulations. Therefore, the compensation approach from Sec. 3.4.3 with two-step estimation method and compensation input is applied. Thereby, the first input u_1, internal combustion engine, is used here for flatness-based feedforward control as well as for disturbance compensation u_c. Moreover, the second input u_2, electric machine, is further used for feedback control.

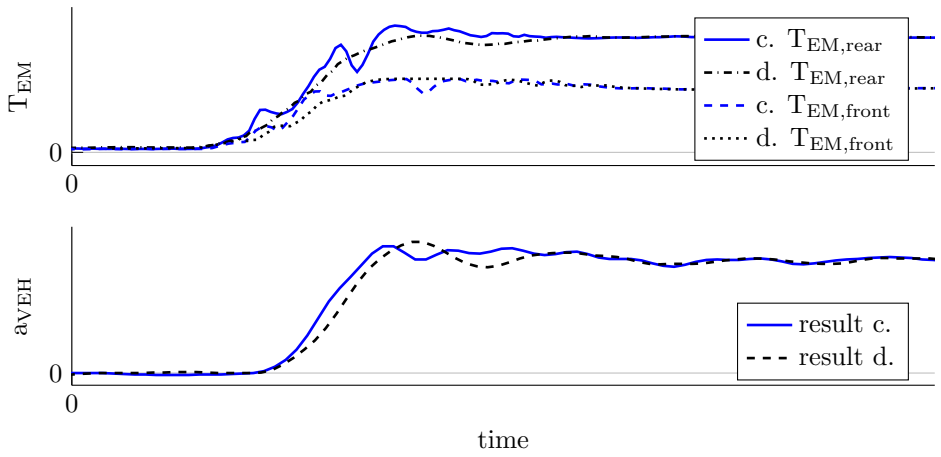

Figure 3.19: Measurements of load changes of a battery electric test vehicle with control method c) and d) for front and rear axle.

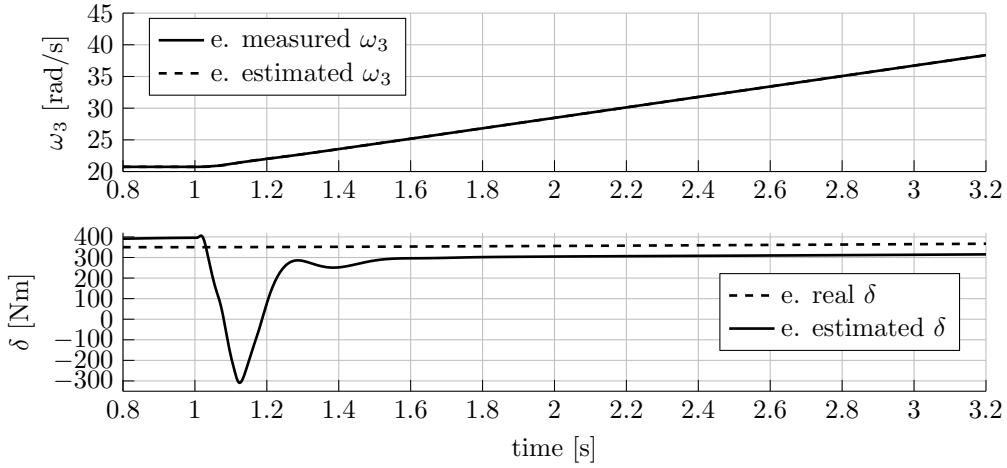

Figure 3.20: Estimation of wheel angular velocity and disturbance.

Figure 3.20 shows that the estimation method can estimate the measured wheel angular velocity ω_3 very accurate. Furthermore, the disturbance δ can be predicted fairly accurately in steady-state. During the transition time ($1\ s \leq t \leq 1.4\ s$) the estimation has to settle. The strong overshoot is due to the zeros on the left half plane of the estimation system, which result from the inverse of the control system transfer function, see therefore Eq. (3.106).

In Fig. 3.21 the control method without disturbance compensation c) from the previous section is compared with the control method with disturbance compensation e). In steady-state the compensation torque u_c of method e) is greater than zero and therefore compensate the estimated disturbance such that the vehicle acceleration a_{VEH} of method e) is not affected by the disturbance is therefore higher than of method c).

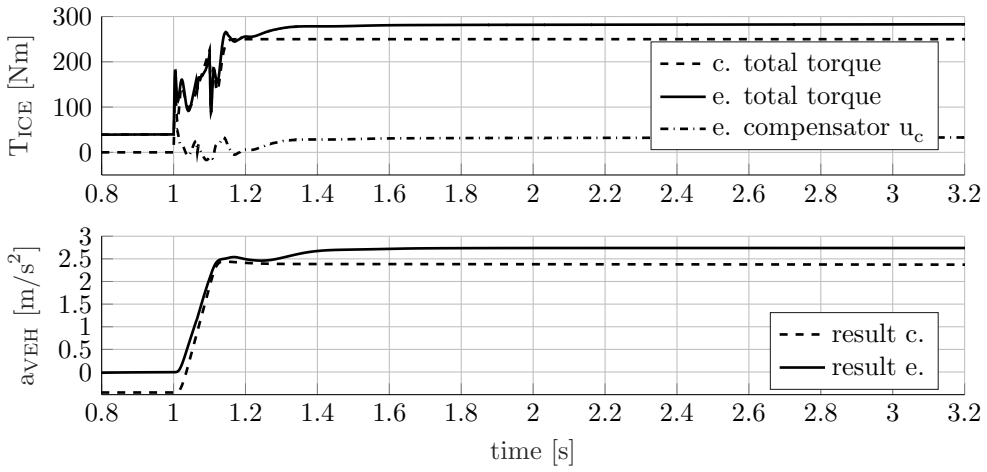

Figure 3.21: Simulation of method c) without disturbance compensation and method e) with disturbance compensation.

Chapter 4

Powertrain Control with Backlash

This chapter focuses on control of load changes from pull to thrust condition and vice versa. The main challenge in this maneuver is that backlash is traversed. Figure. 4.1 illustrates backlash between a driving and a driven gear tooth. Thereby, the gap between the teeth is defined as the backlash gap 2α. Backlash is necessary in mechanical systems due to elongation properties of components and to ensure mounting, but represents a hard nonlinearity. When backlash is traversed no torque is transmitted by the shafts, however when the first contact is achieved, torque is abruptly induced to the system. As a result linear control methods from Chapter 3 may not be sufficient, since they do not consider backlash. Therefore, nonlinear control methods are necessary for this specific drive scenario. First, the effect of backlash on the system dynamics is investigated. Then the dynamics of backlash is modeled as a dead-zone. This dead-zone model is used for the detailed simulation models. Then, for control design a smooth backlash model is derived and the control approaches from the previous chapter are adapted using the new nonlinear control model such that a smooth backlash traversing is enabled. Finally, the proposed approach is validated in simulation study.

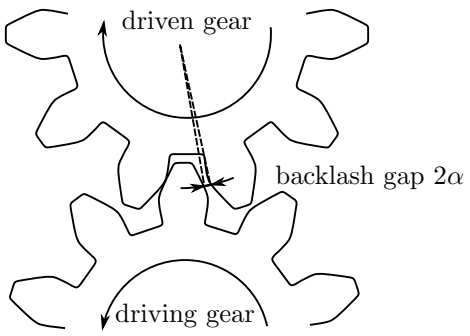

Figure 4.1: Illustration of the backlash gap 2α as depicted in [Speidel17].

4.1 Effects of Backlash

In literature the undesired effects of backlash are well described. When backlash is traversed and the opposite tooth flank is not hit appropriately, then an uncomfortable "shunt and shuffle phenomena" may appear, as described for instance in [LagerbergEgardt05] and [TemplinEgardt11]. The reason is a high derivative of the vehicle longitudinal acceleration (jerk), when the tooth flank is hit. Furthermore, acoustically an undesired "clonk" can appear, see [TemplinEgardt09]. This problem affects especially battery electric vehicles, since electric motors have a very low noise level compared to an internal combustion engine, as described in [Karle16]. Hence, the noise of hitting tooth flanks becomes even more apparent and the driver can recognize this as a substandard noise. Finally, driving and driven parts of the vehicle are separated within backlash. Therefore, the torque from the driving part does not affect the driven part and no drive of the remaining powertrain is possible in backlash. The driver can feel the resulting loss of the vehicle acceleration.

Overall, the effects of shunt, shuffle, clonk, and no torque transmission are particularly striking in the case of low load changes with driving torques about zero, since in this scenario backlash can be traversed several times. In Figure 4.2 a measurement of a tip-in and tip-out maneuver of a battery electric vehicle is shown. At time t_0 the torque of the electric machine T_{EM} changes its sign from negative to positive and at time t_T the reverse maneuver from positive to negative torque is driven. Backlash is traversed once at the tip-in maneuver, however backlash is traversed several time after the tip-out maneuver. The reasons are the small value of the negative drive torque T_{EM} after tip-out. Then, due to driveline oscillations backlash can be re-entered several times. According to the

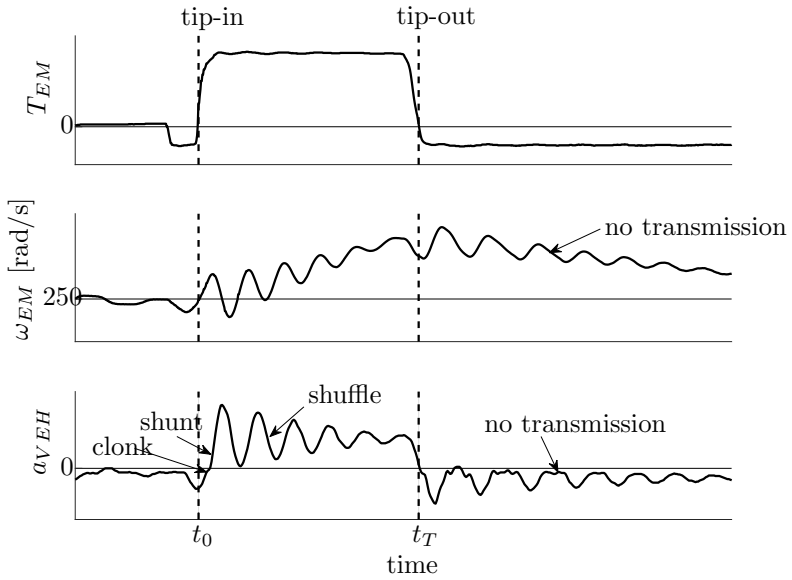

Figure 4.2: Measurement of an uncontrolled load change with backlash traversing.

nearly zero vehicle acceleration a_{VEH} after t_T, the angular velocity of the electric machine ω_{EM} behaves like a sawtooth pattern. This phenomenon occurs because the driven part of the vehicle is not connected with the driving part, which is here an electric machine. Therefore, a constant negative driving torque T_{EM} leads to a straight angular velocity of the electric machine with negative gradient.

The goal of a control approach is to enable a smooth transition, where backlash is traversed with a soft landing, such that the listed undesired effects do not occur.

4.2 Dead-Zone Backlash Models

The typical physical representation of a shaft with backlash gap as presented in [NordinGalic'Gutman97], [Lagerberg01], or [NordinGutman02], is illustrated in Fig. 4.3. Hereby, driving shaft torque T_{ds}, shaft stiffness c, shaft damping d, backlash gap 2α are shown. Furthermore, the rotation angles $\varphi_1, \varphi_2, \varphi_3$ and angular velocities $\omega_1, \omega_2, \omega_3$ are defined as the angles and velocities of the primary side, the location before the backlash gap, and the secondary side.

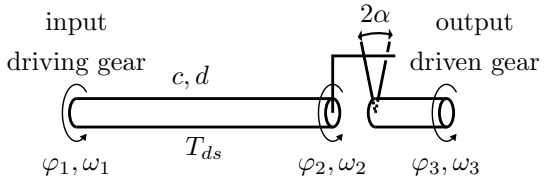

Figure 4.3: Physical representation of a shaft with backlash gap 2α.

Additionally, the following differences are introduced. The total displacements and angular velocities between driving gear and driven gear is

$$\varphi_d = \varphi_1 - \varphi_3, \quad \omega_d = \omega_1 - \omega_3.$$

The shaft twists and its velocities are

$$\varphi_s = \varphi_1 - \varphi_2, \quad \omega_s = \omega_1 - \omega_2,$$

and backlash angle and velocity are

$$\varphi_b = \varphi_2 - \varphi_3, \quad \omega_b = \omega_2 - \omega_3.$$

The backlash angle φ_b is a state, which can change over time, however the backlash gap 2α is a constant parameter.

In [NordinGalic'Gutman97], a dead-zone model for the drive shaft torque T_{ds} with physical backlash representation is derived. It is

$$T_{ds} = c\,(\varphi_d - \varphi_b) + d\,(\omega_d - \omega_b)\,, \tag{4.1}$$

whereby the backlash velocity is described as

$$\omega_b = \begin{cases} \max\left(0, \omega_d + \frac{c}{d}\left(\varphi_d - \varphi_b\right)\right), & \varphi_b = -\alpha \,(\text{left contact}, T_{ds} \leq 0) \\ \omega_d + \frac{c}{d}\left(\varphi_d - \varphi_b\right), & |\varphi_b| < \alpha \,(\text{backlash mode}) \\ \min\left(0, \omega_d + \frac{c}{d}\left(\varphi_d - \varphi_b\right)\right), & \varphi_b = \alpha \,(\text{right contact}, T_{ds} \geq 0)\,. \end{cases} \tag{4.2}$$

[NordinGutman02] describe these equations as a limited integrator with time derivative $\omega_d + \frac{c}{d}\left(\varphi_d - \varphi_b\right)$ and limit α. In backlash mode $|\varphi_b| = \alpha$ the drive shaft torque T_{ds} results to zero. On the other hand, in contact mode different cases can be distinguished. The maximum and minimum functions guarantee that if the backlash angle is in contact mode, for instance $\varphi_b = \alpha$, then the backlash angle is saturated by the half of the backlash gap $\pm\alpha$. Thus, the backlash angle can only change in the reverse direction, here $\omega_b \in [-\infty, 0]$. Moreover, when the system starts to change in the reverse direction, for instance into the backlash gap, then the drive shaft torque T_{ds} goes to zero again.

A difficulty of backlash model (4.1) with Eq. (4.2) is that usually the backlash angle φ_b is unknown and only the total displacement φ_d and velocity ω_d are available. Therefore, for applications a simplified distinction of Eq. (4.2) is made. The backlash angle φ_b is replaced by the half of the backlash gap $\pm\alpha$, as used for instance in [Haschka MarkusVolker07] and [AngeringerHornReichhartinger12]. Then, the simplified dead-zone backlash model reads

$$T_{ds,simple} = \begin{cases} c(\varphi_d + \alpha) + d\omega_d, & \varphi_d \leq -\alpha \\ 0, & |\varphi_d| < \alpha \\ c(\varphi_d - \alpha) + d\omega_d, & \varphi_d \geq \alpha. \end{cases} \tag{4.3}$$

In [Karlsson01] a further distinction is made for dead-zone model (4.3). The physically impossible effect of non-matching direction of the calculated drive shaft torque $T_{ds,simple}$ and the total displacement angle φ_d is prevented, by setting the drive shaft torque T_{ds} to zero in this case, yielding

$$T_{ds} = \begin{cases} 0, & \operatorname{sgn}\left(T_{ds,simple}\right) \neq \operatorname{sgn}\left(\varphi_d\right) \\ T_{ds,simple}, & \text{else} \end{cases} \tag{4.4}$$

with signum function sgn.

This backlash model (4.4) is used to augment the detailed simulation models from chapter 2 to represent the backlash effect. Each spring/damper connection is changed to a spring/damper connection with backlash, since backlash can occur between all components in the powertrain. For the purpose of generalization and illustration, the backlash gaps are parameterized uniformly with

$$2\alpha = 1^\circ = \frac{2\pi}{360}\ rad. \tag{4.5}$$

4.3 Control Using a Smooth Backlash Model

This section presents a nonlinear flatness-based control approach for powertrains with backlash. The approach is based on the model-based linear transient control structure shown in Fig. 3.6. Flatness-based control design requires smooth system dynamics equations. Therefore, the non-smooth dead-zone model (4.3) is approximated by a smooth backlash model. Then, feedforward and feedback controller are designed using this model. Disturbance rejection is not discussed explicitly for control with backlash. It is referred to the linear approach in Sec. 3.4.3, since the influence of backlash on disturbance is small.

4.3.1 Smooth Control Model with Backlash

The dead-zone model from Eq. (4.3) is not suitable for backlash representation in the system equations, since the function is not differentiable for $\Delta\varphi_d = \pm\alpha$. However, the concept of differentially flatness requires a system with smooth vector fields, as defined in (3.40). Therefore, a smooth approximation of the dead-zone model is derived for the two-mass and three-mass control models. Backlash with backlash gap 2α is included in the two-mass and three-mass control model at one position as illustrated in Fig. 4.4 and Fig. 4.5. Furthermore, the smooth drive shaft torque $T_{ds,smooth}$ is introduced.

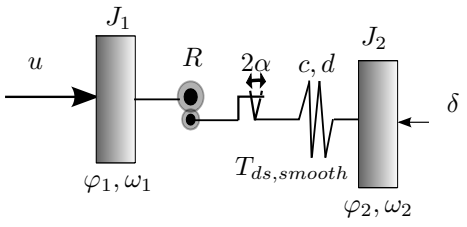

Figure 4.4: Two-mass control model with backlash.

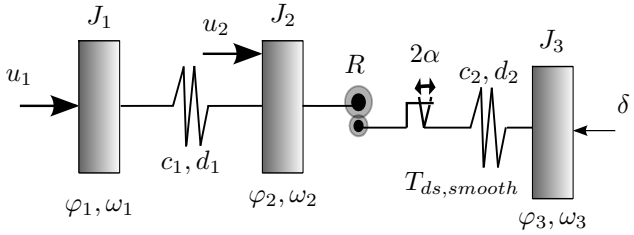

Figure 4.5: Three-mass control model with backlash.

Hence, the system equations (3.12), and (3.27) are adapted by the smooth function and are summarized in the following.

Two-Mass Backlash Model

$$\begin{aligned} \Delta\dot{\varphi} &= \Delta\omega \\ \Delta\dot{\omega} &= -\Theta T_{ds,smooth} + \frac{1}{J_1 R}u + \frac{1}{J_2}\delta \end{aligned} \tag{4.6}$$

with state $\boldsymbol{x} = [\Delta\varphi, \Delta\omega]^T$, $\Delta\varphi = \frac{\varphi_1}{R} - \varphi_2$, and $\Delta\omega = \frac{\omega_1}{R} - \omega_2$.

Three-Mass Backlash Model

$$\begin{aligned}
\Delta\dot{\varphi}_1 &= \Delta\omega_1 \\
\Delta\dot{\varphi}_2 &= \Delta\omega_2 \\
\Delta\dot{\omega}_1 &= -\Theta_1 c_1 \Delta\varphi_1 - \Theta_1 d_1 \Delta\omega_1 + \frac{1}{J_2 R} T_{ds,smooth} + \frac{1}{J_1} u_1 - \frac{1}{J_2} u_2 \\
\Delta\dot{\omega}_2 &= \frac{1}{J_2 R} c_1 \Delta\varphi_1 + \frac{1}{J_2 R} d_1 \Delta\omega_1 - \Theta_2 T_{ds,smooth} + \frac{1}{J_2 R} u_2 + \frac{1}{J_3} \delta
\end{aligned} \tag{4.7}$$

with state $\boldsymbol{x} = [\Delta\varphi_1, \Delta\varphi_2, \Delta\omega_1, \Delta\omega_2]^T$, $\Delta\varphi_1 = \varphi_1 - \varphi_2$, $\Delta\varphi_2 = \frac{\varphi_2}{R} - \varphi_3$, $\Delta\omega_1 = \omega_1 - \omega_2$, and $\Delta\omega_2 = \frac{\omega_2}{R} - \omega_3$. In the following, the modeling of the smooth drive shaft torque $T_{ds,smooth}$ is discussed.

In [PhamEtAl16] an approach to approximate the dead-zone model by a smooth hyperbolic tangent is presented. This approach uses the hyperbolic tangent function tanh in a fade-out function $\sigma(\Delta\varphi)$. When the torsion rotation angle is in the backlash gap, the fade-out function σ is practically zero to enable zero torque. When the torsion rotation angle is outside of the backlash gap, then the fade-out function is almost 1 and the usual drive shaft torque is applied.

There are several possibilities to design the fade-out function $\sigma(\Delta\varphi)$ using the hyperbolic tangent function. Therefore, appropriate functions are presented and analyzed in the following.

In [PhamEtAl16] the fade-out function

$$\sigma_1(\Delta\varphi) = \tanh(a_1|\Delta\varphi|) \tag{4.8}$$

is applied. The tuning parameter $a_1 \in \mathbb{R}$ can be used to fit the curve to the dead-zone model. Further suitable functions are

$$\sigma_2(\Delta\varphi) = \tanh((a_2\Delta\varphi)^k), \tag{4.9}$$

and

$$\sigma_3(\Delta\varphi) = \tanh^k(a_3\Delta\varphi), \tag{4.10}$$

with tuning parameters $a_2, a_3 \in \mathbb{R}$ and even $k \in \mathbb{N}$. All three tuning parameters can be approximated by

$$a_{1,2,3} \approx \frac{1}{\alpha}, \quad \text{with } \alpha > 0. \tag{4.11}$$

Figure 4.6 and Fig. 4.7 shows these fade-out functions $\sigma_1, \sigma_2, \sigma_3$ for half backlash gap $\alpha = 0.5°$ and $\alpha = 1°\}$, respectively.. The order of the fade-out functions σ_2 and σ_3 are varied with $k = \{2, 4\}$.

It can be seen that the fade-out function σ_2 shows the best results for both backlash angles. The reason is that the torsion angle is normalized by the backlash gap and due

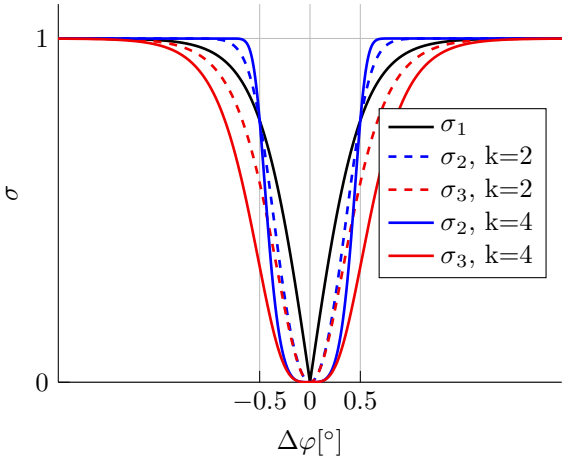

Figure 4.6: Fade-out functions for gap $\alpha = 0.5°$.

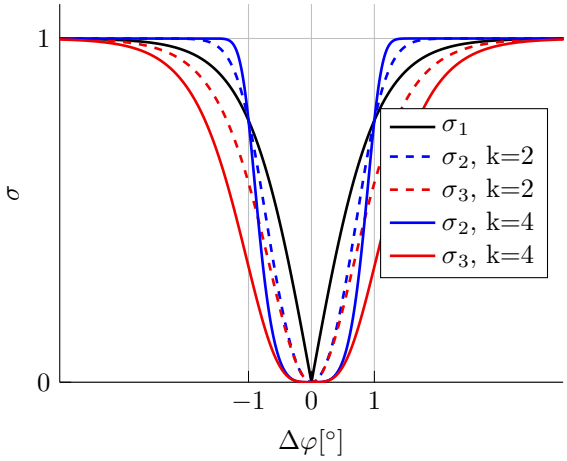

Figure 4.7: Fade-out functions for gap $\alpha = 1°$.

to the exponentiation of the normalized torsion angle, the values in the backlash gap are penalized more and zero torque can be better realized using σ_2. Therefore, fade-out function σ_2 is used in this work to approximate the dead-zone model.

Furthermore, the order of the fade-out function has an important influence on the fade-out shape. The influence of the order on the fade-out function σ_2 is shown in Fig. 4.8. The higher the order of the hyperbolic tangent function is, the more accurate the fade-out function is. However, the computational effort increases with higher order. For control design based on model (4.9), the following fade-out function is chosen

$$\sigma(\Delta\varphi) = \tanh\left(\left(\frac{1}{\alpha}\Delta\varphi\right)^8\right), \quad \text{with } \alpha > 0. \tag{4.12}$$

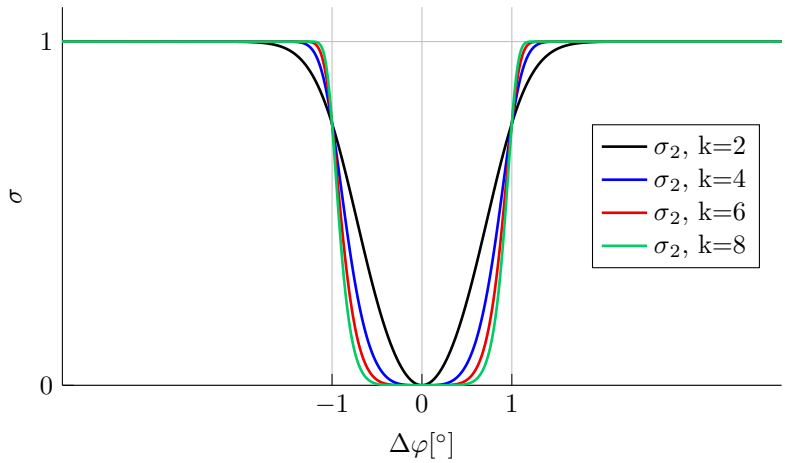

Figure 4.8: Fade-out functions σ_2 with different orders.

Besides, the fade-out function $\sigma(\Delta\varphi)$, the right sign of the axis intercept $\pm c\alpha$ of the drive shaft torque, see Eq. (4.3), has to be ensured. Therefore, the hyperbolic tangent function is again applied to calculate the sign of the axis intercept with $\tanh\left(\frac{1}{\alpha}\Delta\varphi\right)$.

Overall, the smooth drive shaft torque using fade-out function σ and the hyperbolic tangent function for sign definition is given as

$$T_{ds,smooth} = \sigma(\Delta\varphi)\left[c\left(\Delta\varphi - \alpha\tanh\left(\frac{1}{\alpha}\Delta\varphi\right)\right) + d\Delta\omega\right], \tag{4.13}$$

with torsion rotation angle $\Delta\varphi$, torsion angular velocity $\Delta\omega$, stiffness c, damping d, and half backlash gap $\alpha > 0$.

The comparison of the drive shaft torque using the dead-zone model from Eq. (4.3) and the smooth function $T_{ds,smooth}$ from Eq. (4.13) with Eq. (4.12) is shown in Fig. 4.9. The simulation is with stiffness parameter $c = 1.146e4\ \frac{Nm}{rad}$, see Tab. 2.7, damping $d = 0$, and half backlash gap $\alpha = 0.5°$. There is hardly any difference between these two models, however the transition at $\Delta\varphi = \pm 0.5$ is smooth, when using the hyperbolic tangent function.

The smooth function from Eq. (4.13) with (4.12) is applied to the two-mass and three-mass control model. In the detailed simulation model there are several backlashes, however the control models represent only one backlash. Hence, the backlash gaps in the control models have to be parameterized such that the effect of several backlashes in the detailed simulation model is represented.

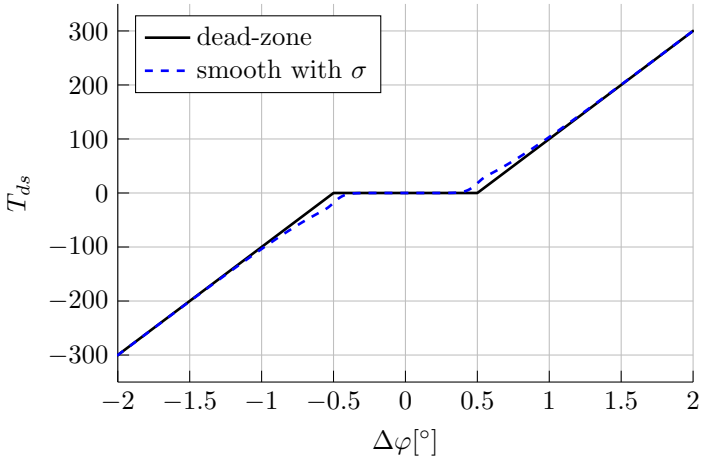

Figure 4.9: Comparison drive shaft torque with dead-zone model vs. smooth function.

4.3.2 Differentially Flat Feedforward Control

First, flat outputs of the nonlinear two-mass and three-mass control model with smooth backlash functions from Eq. (4.13) are given and the differential parameterization of

the control models using the flat output and its derivatives are presented. Then, the corresponding feedforward control law is derived and trajectory planning with nonlinear steady-state calculation is discussed.

4.3.2.1 Flat Outputs and Feedforward Control Laws

In the following, flat output and feedforward control law are calculated in each case for the nonlinear two-mass and three-mass backlash control model.

Two-Mass Backlash Model

The two-mass control model with smooth backlash function reads

$$\begin{aligned}\dot{x}_1 &= \Delta\dot{\varphi} = \Delta\omega \\ \dot{x}_2 &= \Delta\dot{\omega} = -\Theta \underbrace{\tanh\left(\left(\frac{1}{\alpha}\Delta\varphi\right)^8\right)\left[c\left(\Delta\varphi - \alpha\tanh\left(\frac{1}{\alpha}\Delta\varphi\right)\right) + d\Delta\omega\right]}_{=T_{ds,smooth}} \\ &\quad + \frac{1}{J_1 R}u + \frac{1}{J_2}\delta\end{aligned} \tag{4.14}$$

with state $\boldsymbol{x} = [\Delta\varphi, \Delta\omega]^T$ and half backlash gap $\alpha > 0$. It is assumed that the disturbance δ can be compensated by the disturbance rejection approach from Sec. 3.4.3 and is neglected in the following. Hence, it can be shown that

$$z_2 = x_1 = \Delta\varphi, \tag{4.15}$$

is a flat output of the nonlinear system Eq. (4.14), as it is also in the linear case, see Eq. (3.61). Then, the differential parameterization is given as

$$\boldsymbol{x}_2^* = \begin{bmatrix} z_2 \\ \dot{z}_2 \end{bmatrix} = \begin{bmatrix} x_1 \\ x_2 \end{bmatrix}, \tag{4.16}$$

with flatness coordinates $\boldsymbol{x}_2^*$. This transformation is also the inverse transformation from flatness coordinates $\boldsymbol{x}_2^*$ to state vector $\boldsymbol{x}$.

The input parameterization is given by the second derivative of the flat output and therefore the feedforward control law reads

$$\begin{aligned}u_{FF,2,bklsh}(t) &= J_1 R\ddot{z}_{2,des}(t) \\ &\quad + J_1 R\Theta\tanh\left(\left(\frac{1}{\alpha}z_{2,des}(t)\right)^8\right)\left[c\left(z_{2,des}(t) - \alpha\tanh\left(\frac{1}{\alpha}z_{2,des}(t)\right)\right) + d\dot{z}_{2,des}(t)\right],\end{aligned} \tag{4.17}$$

with desired trajectories $z_{2,des}(t)$, $\dot{z}_{2,des}(t)$, and $\ddot{z}_{2,des}(t)$.

Three-Mass Backlash Model

The three-mass control model with smooth backlash function reads

$$\begin{aligned}
\Delta\dot{\varphi}_1 &= \Delta\omega_1 \\
\Delta\dot{\varphi}_2 &= \Delta\omega_2 \\
\Delta\dot{\omega}_1 &= -\Theta_1 c_1 \Delta\varphi_1 - \Theta_1 d_1 \Delta\omega_1 \\
&\quad + \frac{1}{J_2 R} \underbrace{\tanh\left(\left(\frac{1}{\alpha}\Delta\varphi_2\right)^8\right)\left[c_2\left(\Delta\varphi_2 - \alpha\tanh\left(\frac{1}{\alpha}\Delta\varphi_2\right)\right) + d_2\Delta\omega_2\right]}_{=T_{ds,smooth}} + \frac{1}{J_1}u_1 - \frac{1}{J_2}u_2 \\
\Delta\dot{\omega}_2 &= \frac{1}{J_2 R}c_1\Delta\varphi_1 + \frac{1}{J_2 R}d_1\Delta\omega_1 \\
&\quad - \Theta_2 \underbrace{\tanh\left(\left(\frac{1}{\alpha}\Delta\varphi_2\right)^8\right)\left[c_2\left(\Delta\varphi_2 - \alpha\tanh\left(\frac{1}{\alpha}\Delta\varphi_2\right)\right) + d_2\Delta\omega_2\right]}_{=T_{ds,smooth}} + \frac{1}{J_2 R}u_2
\end{aligned} \tag{4.18}$$

with $\boldsymbol{x} = [\Delta\varphi_1, \Delta\varphi_2, \Delta\omega_1, \Delta\omega_2]^T$, first input u_1, second input u_2 and half backlash gap $\alpha > 0$. As in the case of the two-mass model, the disturbance δ is neglected.

Furthermore, damping is neglected in order to make it easier to find a flat output. This procedure is discussed in the remark of Sec. 3.4.1.2. Then, the undamped model equations read

$$\begin{aligned}
\Delta\dot{\varphi}_1 &= \Delta\omega_1 \\
\Delta\dot{\varphi}_2 &= \Delta\omega_2 \\
\Delta\dot{\omega}_1 &= -\Theta_1 c_1 \Delta\varphi_1 \\
&\quad + \frac{1}{J_2 R} \underbrace{\tanh\left(\left(\frac{1}{\alpha}\Delta\varphi_2\right)^8\right)\left[c_2\left(\Delta\varphi_2 - \alpha\tanh\left(\frac{1}{\alpha}\Delta\varphi_2\right)\right)\right]}_{=T_{ds,smooth,red}} + \frac{1}{J_1}u_1 - \frac{1}{J_2}u_2 \\
\Delta\dot{\omega}_2 &= \frac{1}{J_2 R}c_1\Delta\varphi_1 - \Theta_2 \underbrace{\tanh\left(\left(\frac{1}{\alpha}\Delta\varphi_2\right)^8\right)\left[c_2\left(\Delta\varphi_2 - \alpha\tanh\left(\frac{1}{\alpha}\Delta\varphi_2\right)\right)\right]}_{=T_{ds,smooth,red}} + \frac{1}{J_2 R}u_2
\end{aligned} \tag{4.19}$$

with state $\boldsymbol{x} = [\Delta\varphi_1, \Delta\varphi_2, \Delta\omega_1, \Delta\omega_2]^T$. It can be shown that

$$z_3 = x_2 = \Delta\varphi_2 \tag{4.20}$$

is a flat output for the first input u_1 of the simplified undamped nonlinear system (4.19), as also discussed in the remark of Sec. 3.4.1.2 for the linear case.

The differential parameterization for the first input u_1 and without considering second

input u_2 is given as

$$\boldsymbol{x}_3^* = \begin{bmatrix} z_3 \\ \dot{z}_3 \\ \ddot{z}_3 \\ \dddot{z}_3 \end{bmatrix} = \begin{bmatrix} x_2 \\ x_4 \\ \frac{1}{J_2 R} c_1 x_1 - \Theta_2 T_{ds,smooth,red}(x_2) \\ \frac{1}{J_2 R} c_1 x_3 - \Theta_2 \frac{d}{dt} T_{ds,smooth,red}(x_2) \end{bmatrix}. \tag{4.21}$$

Hereby, $\boldsymbol{x}_3^*$ are flat coordinates and the inverse transformation from flat coordinates $\boldsymbol{x}_3^*$ to state vector $\boldsymbol{x}$ reads

$$\boldsymbol{x} = \begin{bmatrix} x_1 \\ x_2 \\ x_3 \\ x_4 \end{bmatrix} = \begin{bmatrix} \frac{J_2 R}{c_1} \left(\ddot{z}_3 + \Theta_2 T_{ds,smooth,red}(z_3) \right) \\ z_3 \\ \frac{J_2 R}{c_1} \left(\dddot{z}_3 + \Theta_2 \frac{d}{dt} T_{ds,smooth,red}(z_3) \right) \\ \dot{z}_3 \end{bmatrix}, \tag{4.22}$$

with the smooth drive shaft torque given as

$$T_{ds,smooth,red}(\chi) = \underbrace{\tanh\left(\left(\frac{1}{\alpha}\chi\right)^8\right)}_{=\nu} c_2 \chi - \underbrace{\tanh\left(\left(\frac{1}{\alpha}\chi\right)^8\right)}_{=\nu} c_2 \alpha \tanh\left(\frac{1}{\alpha}\chi\right). \tag{4.23}$$

Thus, the abbreviations ν and χ are introduced as

$$\nu = \tanh\left(\left(\frac{1}{\alpha}\chi\right)^8\right), \tag{4.24}$$

and

$$\chi = \Delta\varphi_2 = x_2 = z_3, \quad \text{and} \quad \dot{\chi} = \Delta\omega_2 = x_4 = \dot{z}_3. \tag{4.25}$$

Then, the time derivative of the smooth drive shaft torque is

$$\frac{d}{dt} T_{ds,smooth,red}(\chi, \dot{\chi}) = \dot{\nu} c_2 \chi + \nu c_2 \dot{\chi} - \dot{\nu} c_2 \alpha \tanh\left(\frac{1}{\alpha}\chi\right) - \nu c_2 \alpha \left(1 - \tanh^2\left(\frac{1}{\alpha}\chi\right)\right) \frac{1}{\alpha}\dot{\chi} \tag{4.26}$$

with

$$\dot{\nu} = -8 \left(\frac{1}{\alpha}\chi\right)^7 \frac{1}{\alpha}\dot{\chi} \left(\tanh^2\left(\left(\frac{1}{\alpha}\chi\right)^8\right) - 1\right). \tag{4.27}$$

The input parameterization and therefore the feedforward control law can be derived by the fourth derivative of the flat output z_3. It is valid

$$z_3^{(4)} = \frac{1}{J_2 R} c_1 \dot{x}_3 - \Theta_2 \frac{d^2}{dt} T_{ds,smooth,red}(x_2), \tag{4.28}$$

whereby $\dot{x}_3$ is a function of the first input. Hence, it is

$$\begin{aligned} z_3^{(4)} &= \frac{1}{J_2 R} c_1 \left(-\Theta_1 c_1 x_1 + \frac{1}{J_2 R} T_{ds,smooth,red}(x_2) + \frac{1}{J_1} u_1 \right) - \Theta_2 \frac{d^2}{dt} T_{ds,smooth,red}(x_2) \\ &= -\frac{\Theta_1 c_1^2}{J_2 R} x_1 + \frac{c_1}{J_2^2 R^2} T_{ds,smooth,red}(x_2) + \frac{c_1}{J_1 J_2 R} u_1 - \Theta_2 \frac{d^2}{dt} T_{ds,smooth,red}(x_2) \end{aligned} \tag{4.29}$$

Thus, the feedforward control law for the three-mass model using input u_1 and considering backlash reads

$$\begin{aligned} u_{FF,3,u1,bklsh}(t) = u_1 = J_1 \frac{J_2 R}{c_1} \left(z^{(4)}_{3,u1,des}(t) + \Theta_2 \frac{d^2}{dt} T_{ds,smooth,red}(z_{3,u1,des}(t)) \right) \\ + J_1 J_2 \Theta_1 R \left(\ddot{z}_{3,u1,des}(t) + \Theta_2 T_{ds,smooth,red} \left(z_{3,u1,des}(t) \right) \right) \\ - \frac{J_1}{J_2 R} T_{ds,smooth,red} \left(z_{3,u1,des}(t) \right), \end{aligned} \tag{4.30}$$

with the second derivative of the smooth drive shaft torque given as

$$\begin{aligned} \frac{d^2}{dt} T_{ds,smooth,red}(\chi, \dot{\chi}, \ddot{\chi}) = \frac{d^2}{dt} T_{ds,smooth,red}(\chi) \ddot{\nu} c_2 \chi + 2 \dot{\nu} c_2 \dot{\chi} + \nu c_2 \ddot{\chi} \\ - \ddot{\nu} c_2 \alpha \tanh\left(\frac{1}{\alpha} \chi \right) - \dot{\nu} c_2 \alpha \left(1 - \tanh^2 \left(\frac{1}{\alpha} \chi \right) \right) \frac{1}{\alpha} \dot{\chi} \\ - \left(\dot{\nu} c_2 \dot{\chi} + \nu c_2 \ddot{\chi} \right) \left(1 - \tanh^2 \left(\frac{1}{\alpha} \chi \right) \right) \\ - \left(\nu c_2 \dot{\chi} \right) \left(2 \tanh\left(\frac{1}{\alpha} \chi \right) \right) \left(1 - \tanh^2 \left(\frac{1}{\alpha} \chi \right) \right) \frac{1}{\alpha} \dot{\chi} \end{aligned} \tag{4.31}$$

and

$$\begin{aligned} \ddot{\nu} = \left(-56 \left(\frac{1}{\alpha} \chi \right)^6 \frac{2}{\alpha} \ddot{\chi} - 8 \left(\frac{1}{\alpha} \chi \right)^7 \frac{1}{\alpha} \ddot{\chi} \right) \left(\tanh^2 \left(\left(\frac{1}{\alpha} \chi \right)^8 \right) - 1 \right) \\ + \left(-8 \left(\frac{1}{\alpha} \chi \right)^7 \frac{1}{\alpha} \dot{\chi} \right) \left(2 \tanh \left(\left(\frac{1}{\alpha} \chi \right)^8 \right) \dot{\nu} \right). \end{aligned} \tag{4.32}$$

As it can be seen for the derivation of the first input $u_{FF,3,u1,bklsh}(t)$, the calculation of the nonlinear feedforward control law is much more complex than in the linear case, see (3.69). Furthermore, the derivation of a feedforward control law for the second input u_2 is even more difficult in comparison to first input u_1. The reason is that the flat output of the second input has to be a function of the whole system state in order to enable a relative degree of four and is not only a function of one system state as in the case of the first input. Therefore, an analytical derivation of the flatness-based feedforward control law of the second input u_2 is not given here.

4.3.2.2 Trajectory Planning

The feedforward control laws (4.17) and (4.30) requires desired trajectories $z_{2,des}(t)$ and $z_{3,u1,des}(t)$, as discussed in the linear case in Sec. 3.4.1.3. The same approach as described in Sec. 3.4.1.3 and illustrated in Fig. 3.7 for the linear case, is applied here for the nonlinear backlash systems with two main differences.

First, torque hold levels are introduced to the desired drive torque $u_{des}(t)$ to enable soft backlash gap landings. After a zero-crossing of the desired drive torque $u_{des}(t)$, the desired

drive torque is hold for a predefined small time interval at a small positive (negative) torque value for a positive (negative) torque step. Then, a soft backlash gap landing is enabled, since the torque is constant at the hold level and this leads to a steady-state with a vanishing torsion angular velocity. Therefore, an undesired "clonk" noise is prevented. Figure 4.10 illustrates the modified desired drive torque $u_{des}(t)$ with torque hold level.

Second, the calculation of the steady-state of the flat output differs, since the calculation depends on the system dynamics equations. In steady-state the derivatives of the flat output are zero as described in Eq. (3.71). Using this information and the feedforward control laws (4.17) and (4.30), respectively, the steady-states of the two-mass and three-mass backlash models, respectively, are derived.

Two-Mass Backlash Model

In steady-state it is $\dot{z}_2 = \ddot{z}_2 = 0$ and the desired input u_{des} is applied in (4.17). Hence, the steady-state of the flat output $z_{2,ss}$ can be found by solving the nonlinear equation

$$u_{des} = J_1 R\Theta \tanh\left(\left(\frac{1}{\alpha} z_{2,ss}\right)^8\right) c\left(z_{2,ss} - \alpha \tanh\left(\frac{1}{\alpha} z_{2,ss}\right)\right). \tag{4.33}$$

Three-Mass Backlash Model

Furthermore, for the three-mass model it is $\dot{z}_{3,u1} = \ddot{z}_3 = \dddot{z}_{3,u1} = z^{(4)}_{3,u1} = 0$ and the desired input u_{des} is applied in (4.30). Hence, the steady-state of the flat output $z_{3,u1,ss}$ can be found by solving the nonlinear equation

$$u_{des} = J_1 J_2 \Theta_1 \Theta_2 R T_{ds,smooth,red}(z_{3,u1,ss}) - \frac{J_1}{J_2 R} T_{ds,smooth,red}(z_{3,u1,ss}). \tag{4.34}$$

Remark

Solving the nonlinear equations (4.33) and (4.34) can be expensive in the control unit. Therefore, it is beneficial to pre-calculate the equations for different drive torques u_{des} and

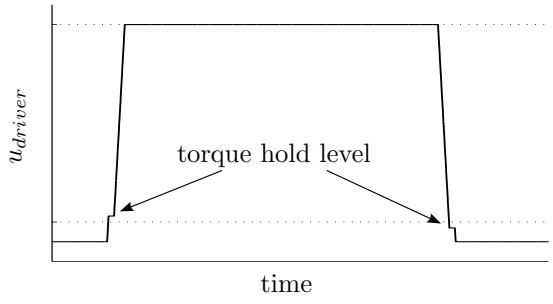

Figure 4.10: Desired drive torque with torque hold level.

save the results in a look-up table. Hence, during drive mode the necessary steady-states are approximated.

4.3.3 Output Feedback Control

The overall control loop shown in Fig. 3.8 is applied to the backlash systems. However, no linear state feedback controller is implemented, since pole placement cannot be designed for the nonlinear backlash systems in comparison to the linear case in Sec. 3.4.2.1. Therefore, output controllers using the desired trajectories of the flat outputs are derived. The desired trajectories consider backlash as they are calculated using the nonlinear backlash steady-state model.

The torsion angular velocities of the systems are controlled in order to affect the damping behavior of the systems, as discussed in Sec. 3.4.2.2. Usefully, the flat outputs of the two-mass and three-mass backlash control models are the torsion rotation angle. Hence, the first derivative of the flat outputs $\dot{z}$ are used for output control. The control law for a proportional controller reads

$$u_{FB} = -k_p \left(\dot{z} - \dot{z}_{des} \right). \tag{4.35}$$

For the two-mass backlash control model the feedback control law is given as

$$u_{FB,2,bklsh} = -k_p \left(\Delta\omega - \Delta\omega_{des} \right), \tag{4.36}$$

and for the three-mass backlash control model the feedback control law

$$u_{FB,3,bklsh} = -k_p \left(\Delta\omega_2 - \Delta\omega_{2,des} \right) \tag{4.37}$$

can be applied using the first input u_1 or second input u_2. However, the second input u_2 is preferred as discussed in the linear case in Sec. 3.4.2.2. Furthermore, this aforementioned section gives approximations for the proportional gain k_p.

4.4 Simulation Applications

This section presents simulation results of the nonlinear control approach using a smooth backlash model. For simulation the powertrain models of hybrid electric and battery electric vehicles from Chapter 2 are used to validate and analyze the proposed method. Goal of the simulation study is

- to show that the nonlinear control models with one backlash can represent the main effects of detailed simulation models with several backlashes sufficiently,
- to validate the nonlinear flatness-based feedforward control approach with backlash and to show the improvement compared to the linear approach without considering backlash explicitly,

- to analyze the desired trajectories, generated by the nonlinear flatness-based approach,
- to show the performance of the overall nonlinear control approach compared to the linear approach.

Comparison of Detailed Simulation Model and Control Model with Backlash

The detailed battery electric powertrain model, described in Sec. 2.4.1, is augmented by backlash. Backlash is implemented at each spring/damping element with $2\alpha = 1^\circ = \frac{2\pi}{360}\ rad$. Furthermore, the two-mass control model of the battery electric powertrain is also augmented by one backlash. The parameters of the control model with smooth backlash using Eq. (4.13) and Eq. (4.12) are summarized in Tab. 4.1. The stiffness parameter c is reduced by 5% in comparison to Tab. 2.7 and damping is reduced to 10 Nms/rad to better fit the detailed simulation model. The backlash gap is parameterized with $2\alpha = 1.8^\circ$. The backlash gap of the control model is greater than the backlash gaps in the detailed simulation model, since one backlash gap of the control model has to represent several backlashes in the detailed simulation model.

Figure 4.11 shows a load change by the engine torque T_{EM} with backlash traversing during a tip-in and tip-out maneuver. The effects of backlash as schematically shown in Fig. 4.2, namely, clonk, shunt, shuffle, and no transmission, can be represented in both models. Moreover, the control model matches the detailed model very precisely.

J_1	0.103	kgm^2
J_2	310.25	kgm^2
c	1.089e4	Nm/rad
d	10	Nms/rad
R	8	1
2α	1.8	$^\circ$

Table 4.1: Parameters of the control model of a battery electric powertrain with backlash.

Validation of Feedforward Controller

First, the nonlinear flatness-based feedforward controller, described in Eq. (4.30), is validated by applying this controller to the nonlinear undamped three-mass backlash control model (4.19), which is also used for control design. The first input of the model u_1 is applied and the second input u_2 is zero during the simulation. The parameters of the

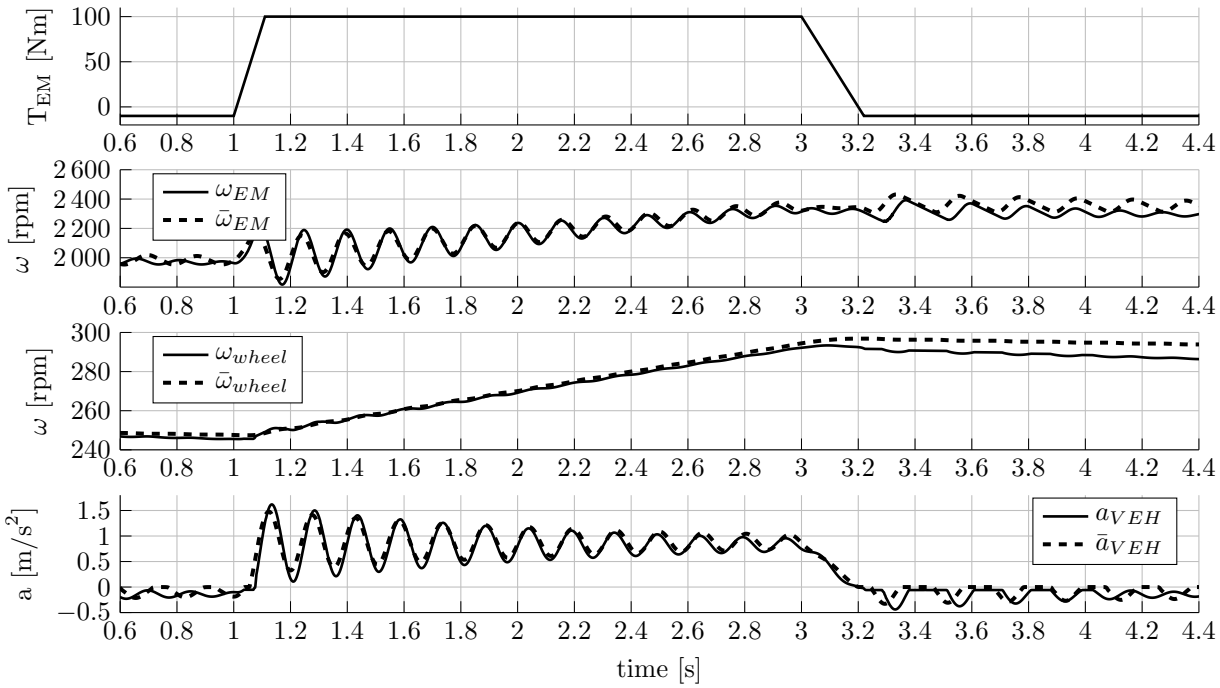

Figure 4.11: Simulation of load changes with backlash traversing by detailed and control battery electric models. States of the control model are marked with a bar.

nonlinear three-mass backlash control model are similar to Tab. 2.5, but the backlash gap $2\alpha = 1.5°$ is added using the smooth drive shaft torque function.

The simulation results of Fig. 4.12 evidents that the nonlinear feedforward controller enables a vibration-free set-point transition of the undamped control model even in the presence of backlash, since no vibrations can be observed in the vehicle acceleration. On the other hand, the uncontrolled method by a ramp shows vibrations with high amplitude.

Second, linear and nonlinear flatness-based feedforward controller $u_{FF,3,u1}$ and $u_{FF,3,u1,bklsh}$ are applied to the detailed hybrid electric powertrain model described in Sec. 2.3.1. Backlashes are implemented at each spring/damping element of the detailed model with backlash gap $2\alpha = 1° = \frac{2\pi}{360}\ rad$. Figure 4.13 shows the results. The nonlinear feedforward controller $u_{FF,3,u1,bklsh}$ causes significantly less driveline oscillations compared to the linear feedforward controller $u_{FF,3,u1}$, which does not consider backlash. Especially the tip-in maneuver is much more comfortable using the nonlinear control approach. However, there are small remaining driveline oscillations for both methods due to unmodeled dynamics.

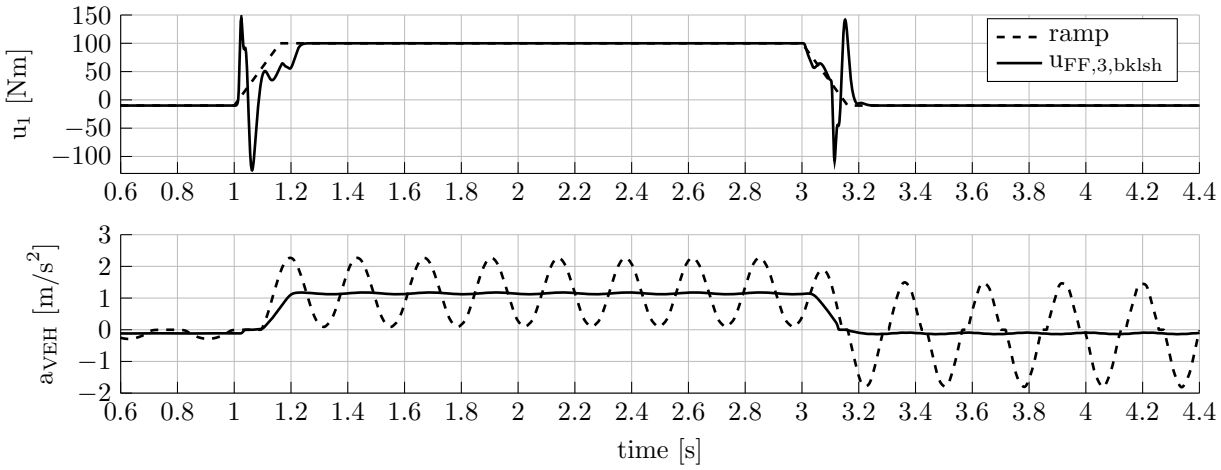

Figure 4.12: Simulation of load changes with the undamped nonlinear three-mass backlash control model using a ramp and the nonlinear flatness-based feedforward controller.

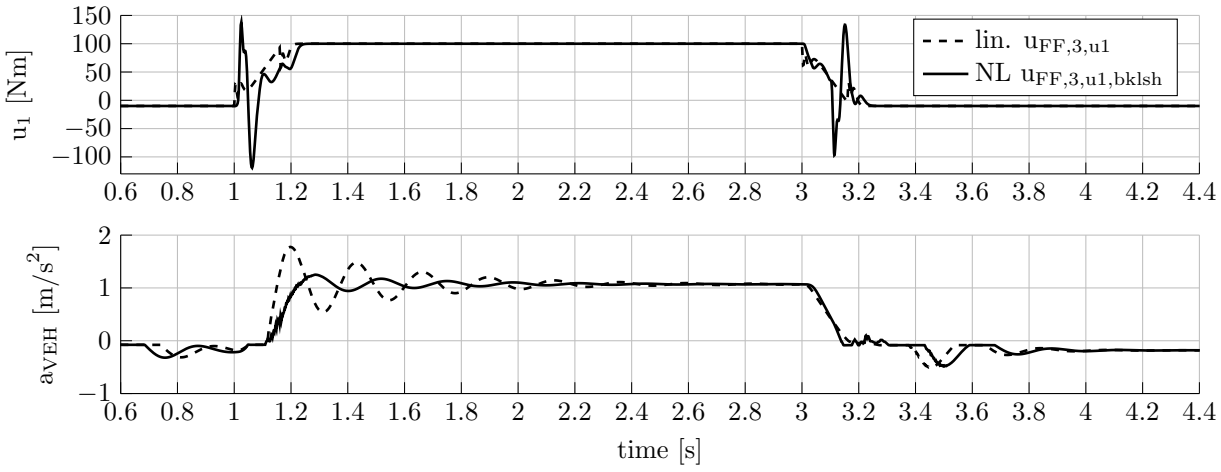

Figure 4.13: Simulation of load changes with the detailed hybrid electric powertrain model using the linear and the nonlinear feedforward controller.

Desired Trajectories

The desired trajectories of the linear and nonlinear flatness-based control approaches differ, since the nonlinear approach introduces torque hold levels and the system dynamics equations consider backlash explicitly. The advantages of the nonlinear approach are shown in Fig. 4.14. The desired trajectories for the torsion rotation angle $\Delta\varphi_{2,des}(t)$ and torsion angular velocity $\Delta\omega_{2,des}(t)$ are depicted. Furthermore, start and end of the backlash gap $\alpha = \pm 0.5° = \pm 0.9e-2\ rad$ are illustrated as dashed lines in the upper figure. When the backlash gap is traversed, the desired trajectory $\Delta\varphi_{2,des}$ introduces a hold level and hence, the desired torsion angular velocity $\Delta\omega_{2,des}$ is zero at this point. Therefore, undesired

noises can be prevented. These desired trajectories are used in feedback control design.

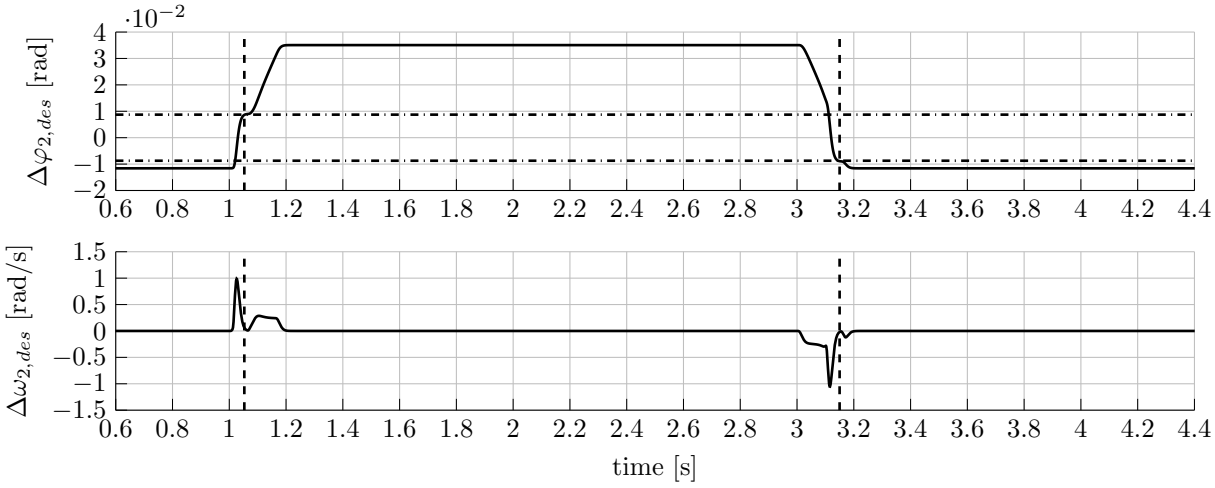

Figure 4.14: Simulation of desired trajectories for torsion rotation angle $\Delta\varphi_{2,des}(t)$ and torsion angular velocity $\Delta\omega_{2,des}(t)$ using the nonlinear backlash control approach.

Comparison of Linear and Nonlinear Overall Control Approach

A feedforward controller cannot guarantee vibration free set-point transitions in real systems, since disturbances and model uncertainties are always present. Hence, a feedback controller is added, as discussed in the linear chapter in Sec. 3.4.2 or in the nonlinear backlash chapter in Sec. 4.3.3. The overall approach, containing feedforward and feedback controller, is applied to the detailed hybrid electric powertrain model and to the battery electric powertrain model, both with backlash gaps.

The results of the linear and nonlinear control approaches using the detailed hybrid electric powertrain model are presented in Fig. 4.15. The feedforward controller is applied to the first input u_1 and the feedback controller is applied to the second input u_2. Both strategies can enable vibration free set-point transitions using the detailed simulation model. However, the nonlinear backlash control approach allows faster backlash traversing compared to the linear approach during tip-out maneuver, which can be seen in the vehicle acceleration a_{VEH} between 2.1 s and 3.1 s.

Furthermore, the overall approaches are compared using the battery electric detailed powertrain model with backlash gaps. Figure 4.16 shows the results. The sum of feedforward and feedback controller are applied to input u, which is supplied by the electric machine. The nonlinear approach has much higher torque interventions, as the desired angular velocity trajectories $\Delta\omega_{des}$ has also much higher gradients. Both methods can control the actual torsion angular velocity and moreover, the vehicle acceleration has no driveline

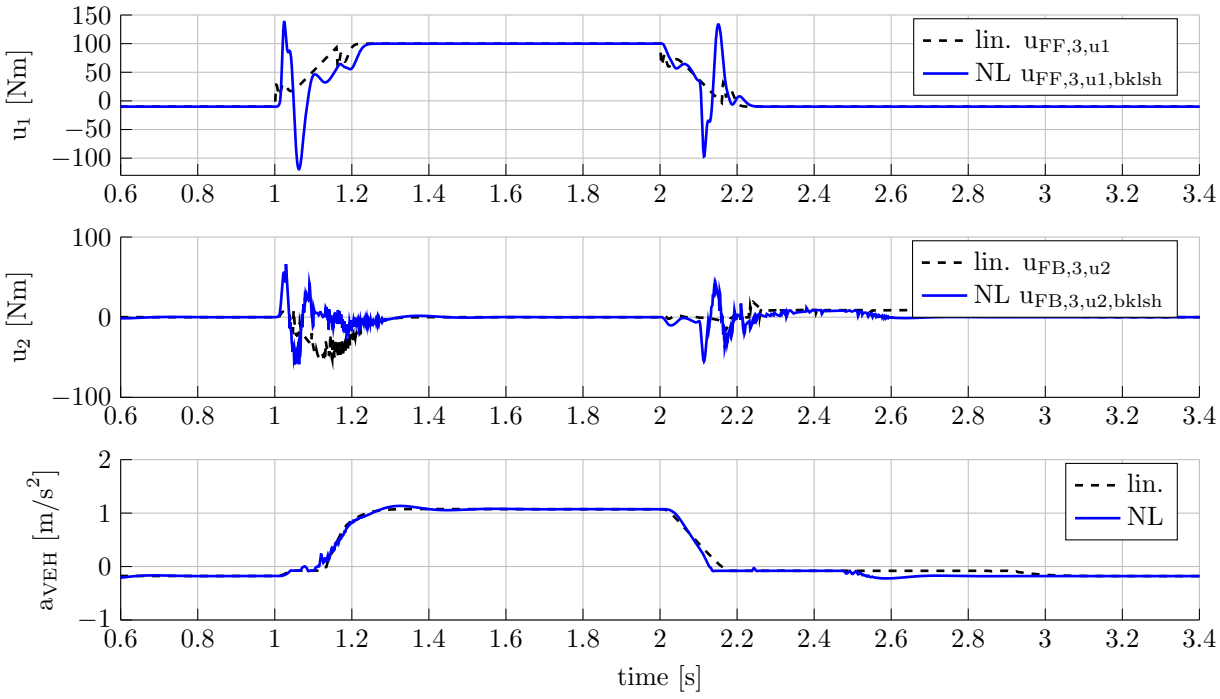

Figure 4.15: Simulation of load changes with the detailed hybrid electric powertrain model using the linear and nonlinear overall control approach.

oscillations. Similar to the simulation using the detailed hybrid electric powertrain model, the nonlinear backlash control approach allows faster backlash traversing compared to the linear approach, especially during tip-out maneuver, shown between 2.1 s to 2.4 s.

Overall, the simulations show that the nonlinear flatness-based feedforward controller with backlash outperforms the linear feedforward controller. However, the linear and nonlinear feedback controllers have an important influence to vibration reduction due to model uncertainties caused by several backlashes and the not exactly known backlash gap size in the detailed simulation model.

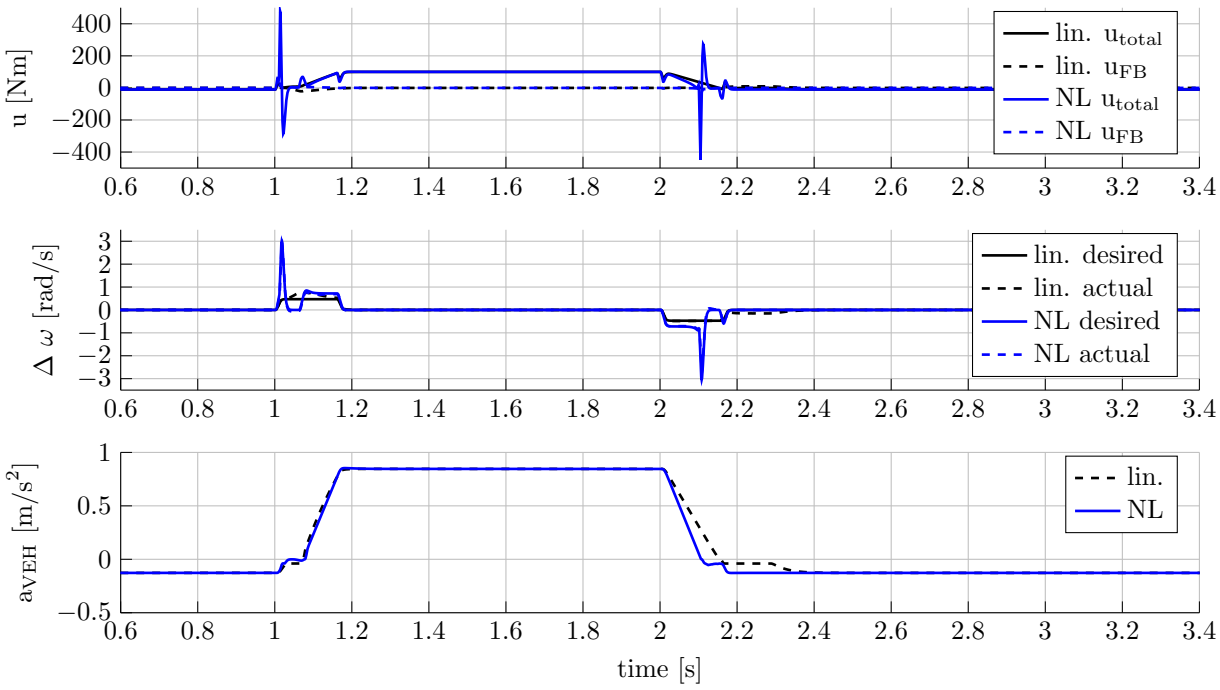

Figure 4.16: Simulation of load changes with the detailed battery electric powertrain model using the linear and nonlinear overall control approach.

Chapter 5

Powertrain Control with Time Delay

Besides backlash, another dominant effect in powertrain systems is time delay. The effect of time delay may not only degrade the tracking performance, as in the case of backlash, but it can also destabilize the closed loop system. This chapter investigates the sources of time delay in powertrain systems and analyzes the effect of time delay to the closed loop stability. Then, different time delay compensation methods, namely Smith predictor, observer based method, and state prediction are applied. Furthermore, a method to visualize stability regions of systems with time delay is derived and is used to compare the derived compensation methods. Simulation results demonstrate the stabilizing and damping effect of the proposed methods.

5.1 Problem Setup

This section discusses the main reasons for time delay in powertrain systems, namely physical delays due to actuator dynamics and electrical delays due to sampling rate or communication between control units. Sampling rates of the control units are considered in this chapter. This necessitates the introduction of digital control systems, since continuous and discrete elements are part of the system.

5.1.1 Reasons for Time Delay in Powertrain Systems

Time delay may occur in the control system due to mechanical or electric reasons. For instance the torque build-up dynamics of an actuator can imply delay, as discussed in [VadamaluBeidl16], and [BaumannEtAl06]. In powertrain systems the dynamics of the actuators, namely combustion engine, electric machine, and clutch, include time delay. Figure 5.1 shows exemplary the torque build-up dynamics of an unit step. The actuator dead time $\tau_{act} = t_\tau - t_0$ is part of the actuator dynamics.

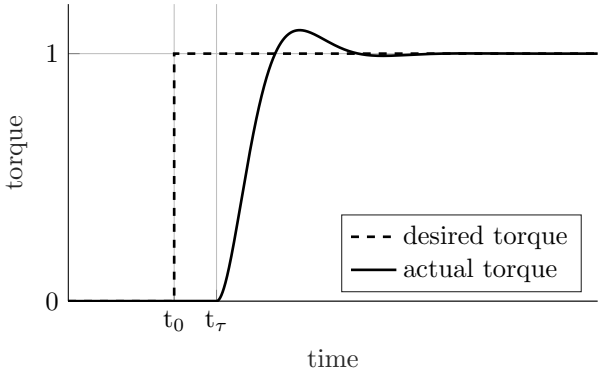

Figure 5.1: Physical delay of an actuator.

Furthermore, electric control units (ECU) are working with a sampling rate and communication between control units or signal filtering contributes further time delays. It follows that measurements can be delayed, if the control algorithm is not placed at the same place as the sensor. The increasing number of electric control units in vehicles, see [BayindirGözüküçükTeke11], amplifies this effect. Measurement and control input signals are delayed as a consequence.

For instance hybrid electric vehicles have several electric control units due to two drive units. The interplay between ICE, EM and driving dynamics control unit is illustrated in Fig. 5.2. Time delays τ_1, τ_2, and τ_3 exist between ICE, EM, and driving dynamics control unit and have to be considered in control design. Overall, for further investigations an actuator dead time τ_{act} and measurement dead time τ_{ms} are considered in powertrain control.

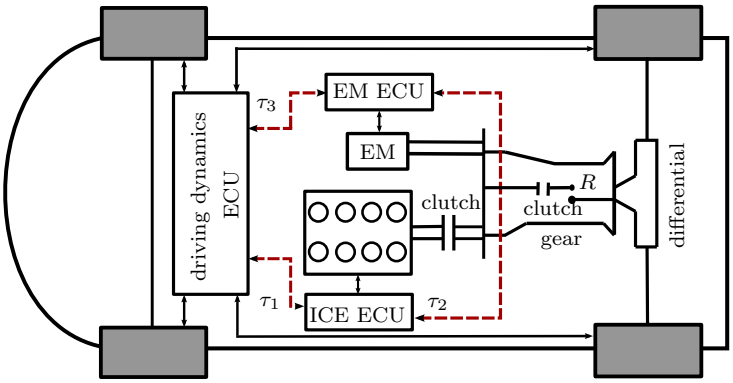

Figure 5.2: ECUs in a rear driven hybrid electric vehicle with time delays τ_1, τ_2, and τ_3 between the control units.

5.1.2 Digital Control System

Control algorithms are implemented in control units. The sampling time of the control unit is defined as T_0. In order to investigate the interaction between the discrete controller and a continuous powertrain system a digital control system is modeled.

Introductions to digital control systems are given for example in [FranklinPowellWorkman98], and [Levine10]. The principal structure of a digital control system is shown in Fig. 5.3. The continuous powertrain system is depicted as $G_p(s)$ and the discrete controller is given as $G_c(z)$. Discrete signals depend on the sampling step k and continuous signals on time t. The calculated control input $u_c(k)$ is a discrete signal based on a discrete reference $r(k)$, discrete measurement $y(k)$ and therefore on a discrete control error $e(k)$.

Additional systems are necessary to interconnect continuous and discrete systems. A zero order hold system $G_{ZOH}(s)$, denoted as D/A (digital to analog), and a sampler, denoted as A/D (analog to digital), are required parts of the overall system.

Furthermore, the digital control structure can be rearranged to a control loop with discretized plant $G_p(z)$, as shown in Fig. 5.4, see [Levine10]. Thereby, the D/A and A/D blocks are moved from control to plant. This rearranged control loop is easier to analyzed and is used in the following. Transfer functions of the zero order hold system, sampler, and the overall system are derived in the subsequent sections.

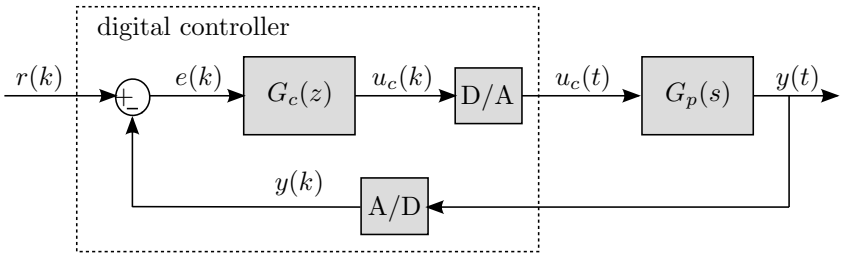

Figure 5.3: General digital control loop.

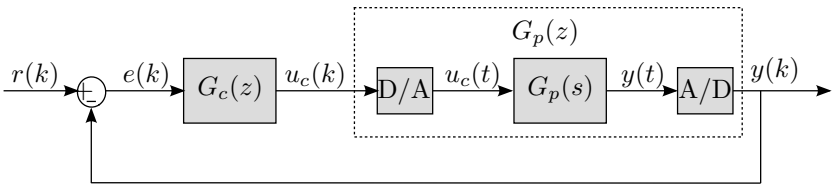

Figure 5.4: Rearranged digital control loop with discretized plant $G_p(z)$.

5.1.2.1 Zero Order Hold

The D/A converter zero order hold reconstructs a continuous signal from a sequence of discrete signals. The incoming discrete signal is hold constant until the next sample is

available. This is realized by the following transfer function in time domain

$$g_{ZOH}(t) = \sigma(t) - \sigma(t - T_0), \tag{5.1}$$

with Heaviside step function σ and sampling time T_0.

Its Laplace transformation is given as

$$G_{ZOH}(s) = \frac{1 - e^{-sT_0}}{s}, \tag{5.2}$$

with $s = j\omega$.

In order to to show the time delay characteristic of $G_{ZOH}(s)$, the transfer function is reformulated to

$$\begin{aligned} G_{ZOH}(s) &= e^{-j\omega\frac{T_0}{2}} \left(\frac{e^{j\omega\frac{T_0}{2}} - e^{-j\omega\frac{T_0}{2}}}{2j} \right) \frac{2j}{j\omega} = e^{-j\omega\frac{T_0}{2}} sin\left(\omega\frac{T_0}{2}\right) \frac{2j}{j\omega} \\ &= T_0 e^{-j\omega\frac{T_0}{2}} \frac{sin\left(\omega\frac{T_0}{2}\right)}{\omega\frac{T_0}{2}} = T_0 e^{-j\omega\frac{T_0}{2}} sinc\left(\omega\frac{T_0}{2}\right). \end{aligned} \tag{5.3}$$

It can be seen that the zero-order hold transfer function introduces a phase shift of

$$arg\left(G_{ZOH}(s)\right) = -\omega\frac{T_0}{2}, \tag{5.4}$$

and a gain of

$$|G_{ZOH}(s)| = T_0 \left| sinc\left(\omega\frac{T_0}{2}\right) \right|. \tag{5.5}$$

5.1.2.2 Sampler

The A/D sampler transforms a continuous signal to a discretized signal. The continuous signal $y(t)$ can be represented as a string of impulses

$$y^*(t) = \sum_{k=-\infty}^{\infty} y(t)\delta\left(t - kT_0\right), \tag{5.6}$$

with Dirac delta function $\delta(t)$. The asterisk * denotes a sampled signal. Due to the sampler, only the measurements at specific sampling instants are available for feedback control. However, the measurements between sampling instants can be important for the closed loop dynamics. For instance, the maximum overshoot may not occur at a sampling point, but at some intermediate point. These responses between sampling points are called as "ripple". The effect of ripple can be examined by simulation and the sampling time T_0 has to be chosen small enough to keep the effect of ripple within limits.

5.1.2.3 Block Diagram Analysis of the Digital Control Loop

The transfer function of the digital control loop with zero order hold and sampler is formulated. Using the zero order hold transfer function $G_{ZOH}(s)$, the discretized plant is given as

$$G_p(z) = Z\left[\underbrace{\frac{1-e^{-sT_0}}{s}}_{G_{ZOH}(s)} G_p(s)\right], \tag{5.7}$$

where Z denotes the z-transformation with A/D sampler. It can be rewritten to

$$G_p(z) = \left(1-z^{-1}\right) Z\left[\frac{G_p(s)}{s}\right]. \tag{5.8}$$

Then, the overall digital control loop with feedback controller $G_c(z)$, as shown in Figure 5.4, reads

$$y(k) = \frac{G_p(z)G_c(z)}{1+G_p(z)G_c(z)} r(k). \tag{5.9}$$

The zero order hold block introduces a delay of $-\omega\frac{T_0}{2}$ to the closed loop system, as shown in Eq. (5.3).

5.1.2.4 Appropriate Choice of Sampling Time

An appropriate sampling time T_0 for the control scheme, shown in Figure 5.4, have to be chosen to avoid aliasing. The lower bound for the sampling rate $f_0 = \frac{1}{T_0}$ is given by the sampling theorem, as for instance discussed in [FranklinPowellEmami-Naeini15]. It is

$$f_0 > 2f_{max}, \tag{5.10}$$

where f_0 is the sampling rate and f_{max} is the maximal frequency of the system. If a lower sampling rate is chosen, the signals would be aliased and the system response could be unstable.

The lower bound may be in practice too slow for an acceptable time response. Therefore, for a reasonably smooth time response

$$10\omega_b < \omega_0 < 40\omega_b, \tag{5.11}$$

with $\omega_0 = 2\pi f_0$ and closed-loop bandwidth ω_b is suggested in [Levine10]. The closed loop bandwidth ω_b describes the frequency at which the closed-loop magnitude drops 3 dB, see for instance [Levine10].

5.2 Powertrain System with Time Delay

The continuous two-mass model from Eq. (3.12) with matrices (3.44) and three-mass model from Eq. (3.27) with matrices (3.48) and (3.49) are discretized such that the closed loop dynamics of a digital control system can be analyzed. Subsequently, the discretized systems are augmented by input and output dead times.

5.2.1 Discretized Control Models

The general transformation of continuous-time systems to discrete-time models, as for instance given in [FranklinPowellWorkman98] or [Levine10], is derived. Consider an n^{th}-order discrete system described by the equations

$$\boldsymbol{x}_{k+1} = \boldsymbol{A}_d \boldsymbol{x}_k + \boldsymbol{B}_d u_k, \quad y_k = \boldsymbol{C}_d \boldsymbol{x}_k + \boldsymbol{D}_k u_k, \quad \boldsymbol{x}_k \in \mathbb{R}^n, \tag{5.12}$$

whereby, discrete matrices and states are denoted by the index d.

The discrete system matrix $\boldsymbol{A}_d$ can be calculated by

$$\boldsymbol{A}_d = e^{\boldsymbol{A}T_0}, \tag{5.13}$$

where $\boldsymbol{A}$ is the continuous system matrix and T_0 the sampling time. Further, due to the zero-order hold, it is assumed that the control input is piecewise constant over the sample time. Furthermore, the discrete input matrix is given as

$$\boldsymbol{B}_d = \int_0^{T_0} e^{\boldsymbol{A}q} \boldsymbol{A} dq = \boldsymbol{A}^{-1} \left(\boldsymbol{A}_d - \boldsymbol{I} \right) \boldsymbol{B}, \tag{5.14}$$

for $\boldsymbol{A}$ nonsingular and with identity matrix $\boldsymbol{I}$. Moreover, it is

$$\boldsymbol{C}_d = \boldsymbol{C}, \quad \boldsymbol{D}_d = \boldsymbol{D}. \tag{5.15}$$

Equations (5.13) and (5.14) are now applied to the two-mass system (3.12) and three-mass control system (3.27).

5.2.1.1 Discrete Two-Mass Control Model

The discrete two-mass control model with discrete states $\boldsymbol{x}_k = [\Delta\varphi_k, \Delta\omega_k]^T$ can be derived analytically by applying Cayley–Hamilton theorem. The transition matrix can be rewritten as a power series

$$e^{\boldsymbol{A}T_0} = \mu_0 \boldsymbol{I} + \mu_1 \boldsymbol{A} + \mu_2 \boldsymbol{A}^2 + \ldots + \mu_{n-1} \boldsymbol{A}^{n-1}. \tag{5.16}$$

The coefficients $\mu_0, \mu_1, \ldots, \mu_{n-1}$ can be calculated using the Cayley–Hamilton theorem. The theorem stated that the following n equations

$$e^{\lambda_i t} = \mu_0 + \mu_1 \lambda_i + \mu_2 \lambda_i^2 + \ldots + \mu_{n-1} \lambda_i^{n-1}, \tag{5.17}$$

with λ_i as the eigenvalue of $\boldsymbol{A}$ for $i = 1, 2 \ldots, n$ are valid, see for instance [Unbehauen07]. For the two-mass system (3.12) we have a pair of complex conjugate eigenvalues

$$\lambda_1 = -a_0 + \omega_0 i, \quad \lambda_2 = -a_0 - \omega_o i. \tag{5.18}$$

Thus, the following linear system of equations has to be solved

$$\begin{bmatrix} 1 & \lambda_1 \\ 1 & \lambda_2 \end{bmatrix} \begin{bmatrix} \mu_0 \\ \mu_1 \end{bmatrix} = \begin{bmatrix} e^{\lambda_1 T_0} \\ e^{\lambda_2 T_0} \end{bmatrix}. \tag{5.19}$$

Then, it is

$$\mu_0 = e^{\lambda_1 T_0} - \lambda_1 \mu_1, \tag{5.20}$$

and

$$\mu_1 = \frac{1}{\lambda_1 - \lambda_2} \left(e^{\lambda_1 T_0} - e^{\lambda_2 T_0} \right). \tag{5.21}$$

The equations can be reformulated to

$$\mu_1 = \frac{1}{\omega_0} e^{-a_0 T_0} \sin(\omega_0 T_0), \tag{5.22}$$

and

$$\mu_0 = e^{-a_0 T_0} \left(\cos(\omega_0 T_0) + a_0 \frac{\sin(\omega_0 T_0)}{\omega_0} \right). \tag{5.23}$$

Using (5.16), then the discrete system matrix is analytically given as

$$\boldsymbol{A}_{2,d} = \mu_0 \boldsymbol{I} + \mu_1 \boldsymbol{A}_2 = \begin{bmatrix} \mu_0 & \mu_1 \\ -\mu_1 \Theta c & \mu_0 - \mu_1 \theta d \end{bmatrix}, \tag{5.24}$$

and the discrete input matrix reads

$$\boldsymbol{B}_{2,d} = \boldsymbol{A}_2^{-1} \left(\boldsymbol{A}_{2,d} - \boldsymbol{I} \right) \boldsymbol{B}_2 = \begin{bmatrix} \frac{1}{J_1 R} \left(-\frac{\mu_0}{\Theta c} + \frac{1}{\Theta c} \right) \\ \frac{1}{\Theta R} \mu_1 \end{bmatrix}. \tag{5.25}$$

Once the discrete system is derived, the corresponding sampling times can be calculated using Eq. (5.11) for the two-mass control models of conventional powertrain, and battery electric powertrain, respectively. The closed-loop bandwidth ω_b is calculated with output controller from Eq. (3.83) and critical proportional gain from Eq. (3.90). The critical gain k_p is chosen in order to calculate the closed loop with the fastest system response. Closed-loop bandwidth ω_b of the system, appropriate sampling frequency $\omega_0 = 10\omega_b$ and appropriate sampling time T_0 are summarized in Tab. 5.1. For further investigations the sampling time $T_0 = 5\ ms$ is chosen, which is appropriate for all three two-mass control models.

	k_p	ω_b	ω_0	T_0
conv. powertrain closed clutch	296.4	39.6 rad/s	396 rad/s	15.9 ms
conv. powertrain open clutch	74.5	112 rad/s	1120 rad/s	5.6 ms
battery electric powertrain	65.6	91 rad/s	910 rad/s	6.9 ms

Table 5.1: Calculated parameters for two-mass models.

5.2.1.2 Discrete Three-Mass Control Model

The analytical derivation of the discrete three-mass control model with discrete states $\boldsymbol{x}_k = [\Delta\varphi_{1,k}, \Delta\varphi_{2,k}, \Delta\omega_{1,k}, \Delta\omega_{2,k}]^T$ is more difficult, since the system order is higher than of the two-mass model. However, the discrete system matrix $\boldsymbol{A}_{3,d}$ and input matrices $\boldsymbol{B}_{3,u1,d}, \boldsymbol{B}_{3,u2,d}$ can be calculated numerically using Eq. (5.13) and Eq. (5.14). Thereby, the continuous matrices from Eq. (3.34), Eq. (3.48), and Eq. (3.49) are applied with an appropriate sampling time T_0. The appropriate sampling time for the three-mass model is calculate analogous to the two-mass control models. For feedback control the critical control gain $k_p = 260$ is applied to the output feedback controller from Eq. (3.91) using the second input u_2. The bandwidth of this closed loop system is calculated and is used to derive an appropriate sampling time. Table 5.2 shows the values with minimum appropriate sampling time $T_0 = 13.1\ ms$. As in the case of the two-mass control models a sampling time of $T_0 = 5\ ms$ is chosen.

	k_p	ω_b	ω_0	T_0
hybrid electric powertrain	260	48 rad/s	480 rad/s	13.1 ms

Table 5.2: Calculated parameters for the hybrid electric three-mass model.

5.2.2 Augmentation of Time Delay

Actuator dead time τ_{act} and measurement dead time τ_{ms} are part of the control loop. In the following, it is assumed that actuator dead time τ_{act} and measurement dead time τ_{ms} are a multiple of the sampling time T_0. Then, it is valid

$$n_{act} = \frac{\tau_{act}}{T_0}, \quad n_{ms} = \frac{\tau_{ms}}{T_0}, \quad \text{with } n_{act}, n_{ms} \in \mathbb{N}, T_0 \neq 0 \tag{5.26}$$

and the discrete signals are delayed by n_{act} and n_{ms} steps, respectively. Figure 5.5 shows the digital control loop with continuous and discrete delayed signals.

The discrete system plant from Eq. (5.12) has to be augmented by the delayed states in order to analyze the closed loop stability and design compensation methods. The amount of delayed steps n_{total} depends on the total dead time. It is

$$n_{total} = n_{act} + n_{ms}. \tag{5.27}$$

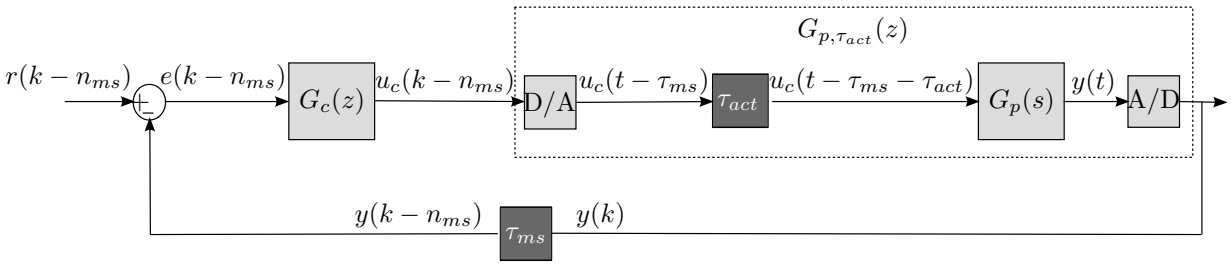

Figure 5.5: Digital control loop with discretized plant $G_{p,\tau_{act}}(z)$, actuator dead time τ_{act} and measurement dead time τ_{ms}.

Then, the augmented system of the n^{th}-order discrete system from Eq. (5.12) has

$$n_a = n + n_{ext} \tag{5.28}$$

states with the number of extended states

$$n_{ext} = n \cdot n_{total}. \tag{5.29}$$

The augmented state vector reads

$$\boldsymbol{x}_{a,k} = [x_k, x_{k-1}, \ldots, x_{k-n_{total}}]^T \in \mathbb{R}^{n_a}, \tag{5.30}$$

where x_{k-i} denote delayed states at time step $(k-i)$ with $i = 1, 2, \ldots n_{total}$.

The general augmented discrete system matrix is given as

$$\boldsymbol{A}_{d,a} = \begin{bmatrix} \boldsymbol{A}_d & \boldsymbol{0}_{n,n_{ext}} \\ \boldsymbol{I}_{n_{ext},n_{ext}} & \boldsymbol{0}_{n_{ext},n} \end{bmatrix} \in \mathbb{R}^{n_a \times n_a}, \tag{5.31}$$

where $\boldsymbol{0}_{n,n_{ext}}$ denotes the $n \times n_{ext}$ zero matrix and $\boldsymbol{0}_{n_{ext},n}$ denotes the $n_{ext} \times n$ zero matrix, respectively. Moreover, $\boldsymbol{I}_{n_{ext},n_{ext}}$ denotes the $n_{ext} \times n_{ext}$ identity matrix.

The augmented discrete input matrix reads

$$\boldsymbol{B}_{d,a} = \begin{bmatrix} \boldsymbol{B}_d \\ \boldsymbol{0}_{n_{ext},1} \end{bmatrix} \in \mathbb{R}^{n_a \times n_a}. \tag{5.32}$$

Two-Mass System

Applying the augmentation to the discrete two-mass control system, the augmented state vector

$$\boldsymbol{x}_{2,a,k} = [\Delta\varphi_k, \Delta\omega_k, \Delta\varphi_{k-1}, \Delta\omega_{k-1}, \ldots, \Delta\varphi_{k-n_{total}}, \Delta\omega_{k-n_{total}}]^T \tag{5.33}$$

results.

The augmented discrete system matrix is given as

$$\boldsymbol{A}_{2,d,a} = \begin{bmatrix} A_{2,d}(1,1) & A_{2,d}(1,2) & 0 & \dots & 0 & 0 & 0 \\ A_{2,d}(2,1) & A_{2,d}(2,2) & 0 & \dots & 0 & 0 & 0 \\ 1 & 0 & \dots & & & & \vdots \\ 0 & 1 & \dots & & & & \vdots \\ 0 & 0 & \ddots & & & & \vdots \\ 0 & 0 & \ddots & 1 & 0 & 0 & 0 \\ 0 & 0 & \ddots & 0 & 1 & 0 & 0 \end{bmatrix} \in \mathbb{R}^{n_a \times n_a}, \tag{5.34}$$

and the augmented discrete input matrix reads

$$\boldsymbol{B}_{2,d,a} = \begin{bmatrix} B_{2,d}(1) \\ B_{2,d}(2) \\ 0 \\ \vdots \\ 0 \end{bmatrix} \in \mathbb{R}^{n_a}. \tag{5.35}$$

Three-Mass System

The discrete three-mass control system can also be augmented by delayed states and the augmented state vector is given as

$$\boldsymbol{x}_{3,a,k} = \left[\Delta\varphi_{1,k}, \Delta\varphi_{2,k}, \Delta\omega_{1,k}, \Delta\omega_{2,k}, \Delta\varphi_{1,k-1}, \dots, \Delta\omega_{2,k-n_{total}}\right]^T. \tag{5.36}$$

The augmented discrete system matrix reads

$$\boldsymbol{A}_{3,d,a} = \begin{bmatrix} \boldsymbol{A}_{3,d} & 0 & \dots & \dots & \dots & \dots & \dots & \dots & \dots & 0 \\ \boldsymbol{I} & 0 & \dots & \dots & \dots & \dots & \dots & \dots & \dots & 0 \\ 0 & 1 & 0 & \dots & \dots & \dots & \dots & \dots & \dots & 0 \\ \vdots & 0 & 1 & 0 & \dots & \dots & \dots & \dots & \dots & 0 \\ \vdots & \vdots & \ddots & \ddots & \ddots & \dots & \dots & \dots & \dots & \vdots \\ \vdots & \vdots & & \ddots & \ddots & \ddots & \dots & \dots & \dots & \vdots \\ 0 & 0 & \dots & \dots & 0 & 1 & 0 & 0 & 0 & 0 \end{bmatrix} \in \mathbb{R}^{n_a \times n_a}, \tag{5.37}$$

with 4×4 identity matrix $\boldsymbol{I}$ and the augmented discrete input matrix is given as

$$\boldsymbol{B}_{2,d,a} = \begin{bmatrix} B_{2,d}(1) \\ B_{2,d}(2) \\ B_{2,d}(3) \\ B_{2,d}(4) \\ 0 \\ \vdots \\ 0 \end{bmatrix} \in \mathbb{R}^{n_a}. \tag{5.38}$$

5.3 Numerical Stability Analysis

An illustration of stability regions of control systems with dead times is presented in this section. First, a numerical discrete method to construct stability diagrams is derived for digital control systems. The derivation is shown using a mass-spring system as an academic example. The numerical method has the advantage over an analytical approach that the degree of stability and damping ratio of the system can be easily calculated additionally. Therefore, the numerical method is extended to illustrate the degree of stability by the maximum absolute eigenvalue and the damping ratio. Secondly, the numerical method is applied to the discrete two-mass powertrain control system from Eq. (2.29) with state-feedback and dead time. The stability diagrams are calculated for varying control gain and varying dead time.

5.3.1 Numerical Calculation of Stability Diagrams

In [HajduInsperger16] stability diagrams are analytically constructed for continuous systems with delayed state feedback and dead time compensation using a Smith Predictor. The analytical constructions are based on the D-subdivision method and Stepan's formulas, as presented in [Stépán89]. The D-subdivision method allows to calculate the stability boundaries by separating real and imaginary part of the characteristic equation. Moreover, Stepan's formula determines the number of unstable characteristic exponents in each domain of the stability chart, see [Stépán89].

In the following, this method of illustrating stability regions is transferred to the analysis of digital control systems. Therefore, the analytical construction of the stability charts are replaced by a numerically calculation of eigenvalues of the discrete system augmented by delayed states as derived in Eq. (5.34) and Eq. (5.37). Similar numerical methods, as semi-discretization, are presented in [InspergerStépán02] and [InspergerStépán11]. The analytical and numerical stability charts are calculated and compared in the following for a mass-spring system.

Example: Mass-Spring System With Delayed Feedback

The objective is to calculate numerically a stability chart as considered in [HajduInsperger16], where the chart is derived analytically. The system matrix of the mass-spring system is given as

$$\boldsymbol{A} = \begin{bmatrix} 0 & 1 \\ -a & 0 \end{bmatrix}, \tag{5.39}$$

with $a = 0.5$ and hence, the system matrix is stable. The input matrix is given as

$$\boldsymbol{B} = \begin{bmatrix} 0 \\ -1 \end{bmatrix}. \tag{5.40}$$

A state feedback is used and defined as

$$u = \boldsymbol{k}^T \boldsymbol{x}\left(t - \tau\right), \tag{5.41}$$

with delayed state $\boldsymbol{x}\left(t - \tau\right)$, time delay τ and control gain $\boldsymbol{k} = [p, d]^T \in \mathbb{R}^2$. Hence, the closed loop system dynamics reads

$$\dot{\boldsymbol{x}} = \boldsymbol{A}\boldsymbol{x}(t) + \boldsymbol{B}\boldsymbol{k}^T \boldsymbol{x}\left(t - \tau\right). \tag{5.42}$$

The analytically calculated stability chart from [HajduInsperger16] for the continuous system (5.42) is shown on the left in Fig. 5.6 for time delay $\tau = 1$ and varying control gain $p \in [-1, 1]$ and $d \in [-1, 2]$. The stable regions are shaded in gray and the system is only stable for proportional gain $p \geq -a$. In the following, the steps for the numerical calculation of the stability charts are given.

1. Discretization

The continuous system is discretized using Eq. (5.13) and Eq. (5.14). The sampling time $T_0 = 0.05\ s$ is chosen. Then, the discrete system matrix and input vector read

$$\boldsymbol{A}_d = \begin{bmatrix} 0.99 & 0.05 \\ -0.025 & 0.99 \end{bmatrix}, \quad \boldsymbol{B}_d = \begin{bmatrix} -0.001 \\ -0.05 \end{bmatrix}. \tag{5.43}$$

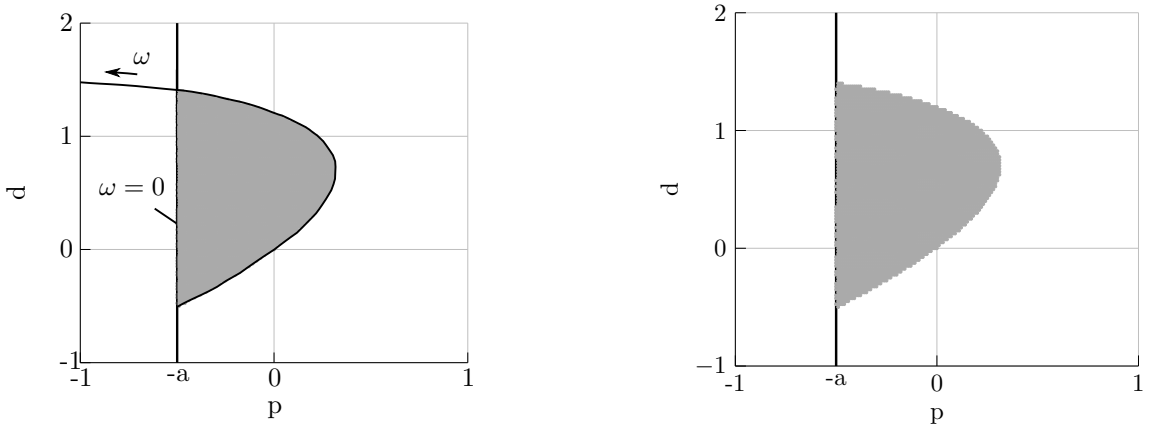

Figure 5.6: Comparison of analytical stability chart according to [HajduInsperger16] (left) and numerically calculated chart (right).

2. Augmentation Time Delay

The discrete system is augmented by delayed states. The number of delayed steps is given as $n_{total} = \frac{\tau_{total}}{T_0} = 20$, see Eq. (5.26). Hence, the augmented system order yields $n_a = 2 + 2 \cdot 20 = 42$, as given in (5.28). The augmented state vector at time point k reads

$$\boldsymbol{x}_{a,k} = \left[x_{1,k}, x_{2,k}, x_{1,k-1}, x_{2,k-1}, \ldots, x_{1,k-20}, x_{2,k-20}\right]^T \in \mathbb{R}^{42}. \tag{5.44}$$

The augmented discrete matrices are

$$\boldsymbol{A}_{d,a} = \begin{bmatrix} \boldsymbol{A}_d & \boldsymbol{0}_{2,40} \\ \boldsymbol{I}_{40,40} & \boldsymbol{0}_{40,2} \end{bmatrix}, \quad \boldsymbol{B}_{d,a} = \begin{bmatrix} \boldsymbol{B}_d \\ \boldsymbol{0}_{40,1} \end{bmatrix}, \tag{5.45}$$

as derived in (5.31) and (5.32).

3. Delayed Augmented Feedback

The state feedback controller is stated with delayed discrete states. Using the augmented delayed state, the delayed discrete state feedback controller reads

$$u_k = \boldsymbol{k}^T \boldsymbol{x}_{k-20}. \tag{5.46}$$

Then, the control gain vector $\boldsymbol{k}^T$ is augmented to

$$\boldsymbol{k}_a^T = \left[\boldsymbol{0}_{1,n_{ext}}, p, d\right], \tag{5.47}$$

with zero matrix $\boldsymbol{0}_{1,n_{ext}}$ and dimension $1 \times n_{ext}$. It follows that the augmented feedback controller can be rewritten to a function of the augmented state vector from Eq. (5.44) with

$$u_k = \boldsymbol{k}_a^T \boldsymbol{x}_{a,k}. \tag{5.48}$$

Finally, the delayed discrete closed loop system reads

$$\boldsymbol{x}_{a,k+1} = \boldsymbol{A}_{d,a}\boldsymbol{x}_{a,k} + \boldsymbol{B}_{d,a}\boldsymbol{k}_a^T\boldsymbol{x}_{a,k} = \underbrace{\left(\boldsymbol{A}_{d,a} + \boldsymbol{B}_{d,a}\boldsymbol{k}_a^T\right)}_{=\boldsymbol{A}_{d,a,cl}} \boldsymbol{x}_{a,k}, \tag{5.49}$$

with discrete augmented closed loop system matrix $\boldsymbol{A}_{d,a,cl}$.

4. Evaluation Eigenvalues

Now, the eigenvalues of the closed loop system matrix $\boldsymbol{A}_{d,a,cl}$ can be evaluated over a grid of values of control gains p, d. The closed loop system is unstable, if there exists a discrete eigenvalue $z_{k,l}$ of $\boldsymbol{A}_{d,a,cl}$ for a parameter constellation p_k, d_l, with

$$|z_{k,l}| > 1. \tag{5.50}$$

Otherwise the closed loop system is stable and the point p_k, d_l is shaded grey in the stability chart to mark a stable region.

The stability chart on the right in Fig. 5.6 shows the numerical evaluation over a grid of $p_k \in [-1, 1]$ with step size 0.01 and $d_l \in [-1, 2]$ with step size 0.025. Hence, the discrete augmented closed loop system matrix $\boldsymbol{A}_{d,a,cl}$ is evaluated 24321 times.

The figure demonstrates that analytical (left) and numerical (right) stability charts are similar and therefore the numerical approach can generate stability diagrams with sufficient accuracy. However, the numerical approach cannot provide exact D-curves, which represent stability boundaries in the analytical chart. But on the other hand, the numerical method has other advantages. The stability charts can be easy calculated using numerically methods and further investigations on the eigenvalues are possible. In the following investigations regarding the maximum magnitude and damping ratio, are derived.

The maximum magnitude $|z_{max}|$ of the discrete eigenvalues z_i with $i \in \{1, 2, \ldots, n_a\}$ represents how far away the eigenvalues of the stable systems are from stability boundary. It is calculated by

$$|z_{max}| = \max\{|z_1|, |z_2|, \ldots, |z_{n_a}|\}. \tag{5.51}$$

Furthermore, the dominant damping ratio ξ_{dom} of the most dominant eigenvalue of the stable system is calculated, since it determines in large part the damping behavior. The most dominant eigenvalue is given as the continuous eigenvalue with the greatest stable real part. Therefore, the transformation from discrete to continuous eigenvalues is necessary. The transformation is given as

$$\lambda_i = \frac{\ln(z_i)}{T_0}, \tag{5.52}$$

as for instance discussed in [Lunze16].

Then, the dominant damping ratio ξ_{dom} can be calculated using Eq. (3.38).

Figure 5.7 shows the stability charts of the closed loop delayed system with maximum absolute eigenvalue on the left side and dominant damping ratio on the right side. The red regions are favored since they mark low maximum magnitudes of the discrete eigenvalues or high damping, respectively. Both favored properties can be considered separately. The regions with the largest intersection between stability and damping is desired. For instance a control gain with $p = -0.25, d = 0.4$ is a good choice for stability and damping.

Furthermore, time simulations using the continuous time system with delayed feedback from Eq. (5.42) are performed with various control gains in order to verify the calculated stability charts. The system is deflected by the initial condition $\boldsymbol{x}_0 = [1, 0]^T$. Figure 5.8 illustrates time simulations with the following control gains, chosen from the stability charts:

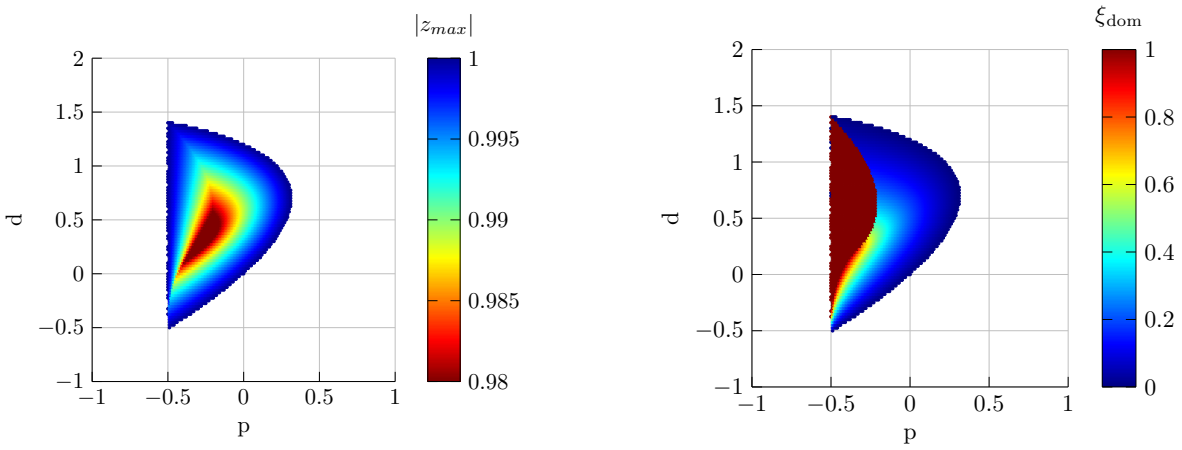

Figure 5.7: Numerically calculated stability charts with color coded maximum absolute eigenvalue of the discrete eigenvalues (left) and color coded damping ratio of the dominant eigenvalue (right).

- a) $p = -0.25, d = 0.4$, small maximum magnitude and high damping
- b) $p = -0.15, d = 0.4$, small maximum magnitude, average damping
- c) $p = 0.25, d = 0.4$, maximum magnitude 1, no damping, marginally stable

As the stability charts show, the simulation with control gain a) has the best damping behavior such that the steady-state $x_{1,ss} = 0$ can be reached fast. The simulation using control gain b) has average damping behavior and the simulation using gain c) has no damping and the system is stable but not asymptotically stable, as calculated in the stability chart.

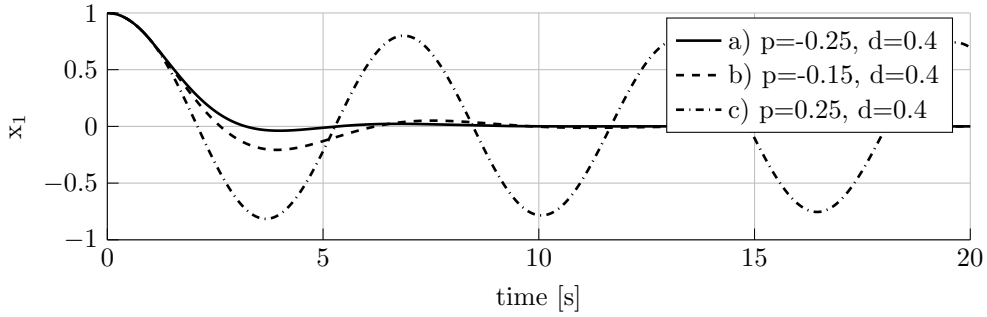

Figure 5.8: Time simulation of the first state x_1 of the continuous delayed closed loop mass-spring system with various control gains to check the stability charts.

5.3.2 Stability Diagrams of Two-Mass Control Systems

In the following, the numerical approach of constructing stability charts, as described in the previous Sec. 5.3.1, is applied to a powertrain control model. The stability charts are calculated for the linear two-mass control system (3.12) of a battery-electric powertrain with parameters from Tab. 2.7. A state feedback controller as described in Eq. (5.41) is applied. The time delays τ_{act} and τ_{ms}, as shown in Fig. 5.5, are summed up to one total time delay $\tau_{total} = \tau_{act} + \tau_{ms}$. First, the stability charts with varied control gains are calculated, as investigated in the previous section and in the examples presented in [HajduInsperger16]. Furthermore, the numerical method also allows to vary other parameters beside the control gain. In this work the influence of variation of the time delay itself is calculated.

5.3.2.1 Varying Control Gain

The series of stability diagrams for the battery-electric two-mass control model with color coded maximum absolute eigenvalue and damping ratio are shown in Fig. 5.9 and Fig. 5.10. They are calculated following the steps 1-4 as described in the previous Sec. 5.3.1. The two-mass control model (3.12) is discretized with an appropriate sampling time of $T_0 = 5\ ms$, as derived in Tab. 5.1. The charts are calculated for various fixed dead times $\tau_1 = 0\ ms, \tau_2 = 10\ ms, \tau_3 = 20\ ms$, and $\tau_4 = 30\ ms$, respectively.

For better assessing of the control parameters, the proportional gain $\boldsymbol{k} = [p, d]^T$ is reformulated to $\boldsymbol{k}_{rpm} = [p_{rpm}, d_{rpm}]^T$. It is common in automotive systems that angular velocities are calculated in rpm instead of rad/s. Moreover divisions are often avoided and therefore the total gear ratio R is not divided from the first mass of inertia φ_1, ω_1, but multiplied to the second mass of inertia φ_2, ω_2. Hence, the new control gains p_{rpm}, d_{rpm} are calculated as

$$p_{rpm} = p\frac{\pi}{30R}, \quad d_{rpm} = d\frac{\pi}{30R}, \tag{5.53}$$

since it is

$$u = -\underbrace{p\frac{\pi}{30R}}_{=p_{rpm}}(\varphi_1 - R\varphi_2) - \underbrace{d\frac{\pi}{30R}}_{=d_{rpm}}(\omega_1 - R\omega_2), \tag{5.54}$$

with φ_1, φ_2 in $rounds$ and ω_1, ω_2 in rpm.

The nominal case, where no time delay is added, is illustrated on the far left of Fig. 5.9 and Fig. 5.10. The stability charts confirm the analysis from Chapter 3 that the system is more damped with higher proportional gain d_{rpm} applied to the torsion angular velocity $\Delta\omega$. Though, proportional control gains $d_{rpm} > 4.25$ destabilize the system, since the system plant is discretized with sampling time $T_0 = 5\ ms$ and therefore, time delay $\frac{T_0}{2}$ is introduced inherently, see Eq. (5.4). The more time delay is added to the system, the smaller the stable regions are. In particular the regions with high damping are becoming increasingly more

compact, such that a pure controller on the angular velocity $\Delta\omega$, with $p_{rpm} = 0, d_{rpm} \neq 0$, cannot enable a closed loop system with appropriate damping for time delay $\tau > 10\ ms$. Hence, the state-feedback controller (5.41) reaches its limits, when larger time delays are present. This shows that time delay compensation methods are necessary.

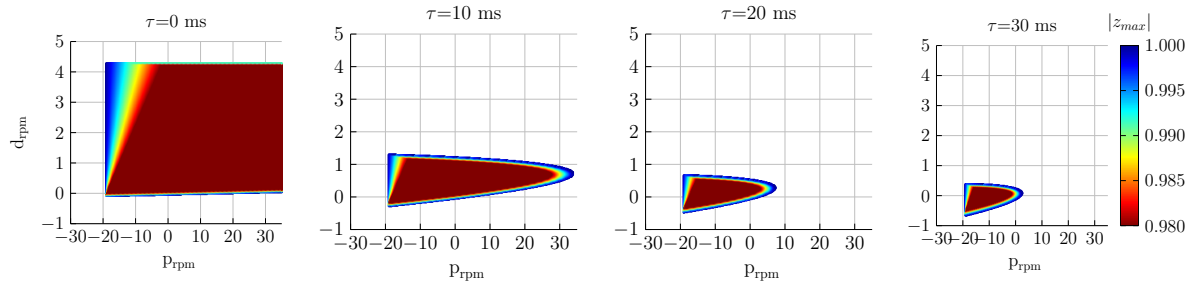

Figure 5.9: Numerically calculated stability charts for the battery-electric powertrain control model with color coded maximum absolute value for various time delay.

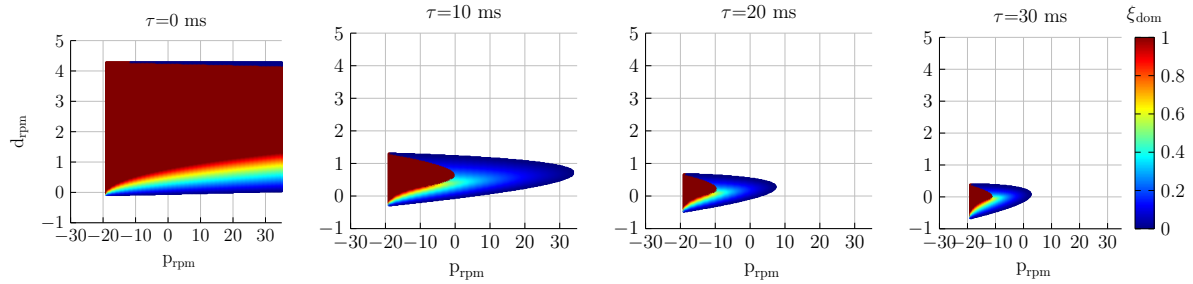

Figure 5.10: Numerically calculated stability charts for the battery-electric powertrain control model with color coded dominant damping ratio for various time delay.

5.3.2.2 Varying Time Delay

The magnitude of time delay has an important impact to the system stability. Therefore, stability charts with varying time delay are investigated in the following. Besides the control gain d, the time delay is varied on the y-axis. The output controller $u = -d\Delta\omega$, as described in Eq. (3.83), is applied to the two-mass control model from Eq. (2.29). Figure 5.11 shows the stability regions with color coded maximum absolute eigenvalue $|z_{max}|$ and color coded dominant damping ratio ξ_{dom}. The stability charts illustrate the delay margins of the closed loop system for fixed control gain $p_{rpm} = 0$ and various control gains d_{rpm}. The boundary of the stability region in the stability chart is the delay margin of a specific gain d_{rpm}. For instance a control gain of $d_{rpm} = 2$ has a delay margin $\tau_{margin} \approx 8\ ms$.

The delay-margin is a significant size of time delayed systems and it is formally defined as

Definition 4 ([Normey-Rico07]). *The delay margin is characterized by the minimum time delay $\tau_{margin} > 0$ such that the closed-loop system becomes unstable.*

Additionally, it can be calculated by the phase margin ϕ_r and the crossover frequency ω_0 of the open loop system with

$$\tau_{margin} = \frac{\phi_r}{\omega_0}. \tag{5.55}$$

However, the stability charts enable a good overview of delay margins for several control gains d_{rpm}. Figure 5.11 shows that the larger the control gain $d_{rpm} > 0$ becomes, the smaller the delay margin τ_{margin} is. In addition, the delay margin decreases significantly for control gains $d_{rpm} > 0.5$. These stability charts enable the important finding, that regions with good stability and high damping behavior are only for control gains $d_{rpm} \approx 0.8$ and time delays up to 10 ms possible.

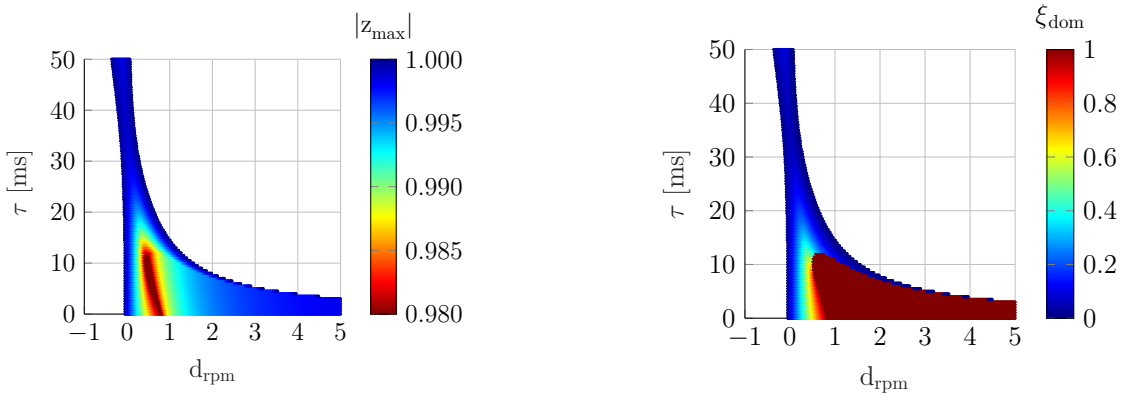

Figure 5.11: Numerically calculated stability charts with color coded maximum absolute value of the discrete eigenvalues (left) and color coded damping ratio of the dominant eigenvalue (right) for various control gain d_{rpm} and time delay τ.

5.4 Compensation Methods

The stability diagrams, presented in the last section, indicate that time delay in a feedback control system greatly restrict the stability and the damping behavior of the system. Hence, time delay compensation methods are derived in this section to enable a well damped stable system. In Fig. 5.12 a digital control loop with system Σ, time delays τ_{act}, τ_{ms}, feedforward and feedback controller u_{ff}, u_{FB} and dead time compensation is shown. The two-mass control system of the battery electric powertrain from Eq. (2.29) is considered here as the system Σ, which was also considered in the previous Sec. 5.3.

The flatness-based approach, as shown in Fig. 3.6, planes desired trajectories $x_{des,k}$ depending on the driver's request by the throttle pedal at discrete time step k and calculates the feedforward controller $u_{FF,k}$. A feedforward controller cannot destabilize a

digital control loop system with dead times, since no delayed signals are used in a feedback manner. However, the feedforward controller $u_{FF}(t)$ will be delayed by the actuator dead time τ_{act}, see [Rudolph05]. This time shift cannot be prevented, since the trajectories would have to be planned ahead for dead time compensation, before the driver changes the pedal position. As the intention of the driver cannot always be predicted, a compensation of this time shift is not possible. Thus, the feedforward control approach, as presented in Chapter 3, with feedforward control law (3.63) is used for the time delayed system.

The second controller in the system is a state feedback controller, as presented in Sec. 3.4.2. It is assumed that the undelayed state $\tilde{\boldsymbol{x}}_{\boldsymbol{k}}$ is available due to a dead time compensator. The state feedback control law reads $u_{FB} = -\boldsymbol{k}^T (\tilde{\boldsymbol{x}}_{\boldsymbol{k}} - \boldsymbol{x}_{des})$ with control gain $\boldsymbol{k}^T$, see Eq. (3.79).

The focus of this section is to investigate different dead time compensation methods, namely Smith predictor, observer based design, and state prediction, in order to compensate the total dead time $\tau_{total} = \tau_{act} + \tau_{ms}$ of the delayed state $x_{k-n_{act}-n_{ms}}$. The corresponding stability charts of the compensation methods are calculated and used to compare the methods. Furthermore, time simulations are analyzed.

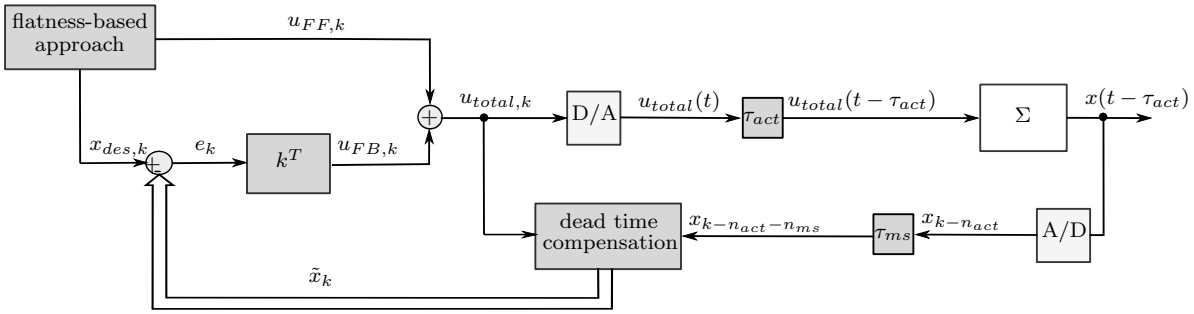

Figure 5.12: Overall control loop with time delays and dead time compensation.

5.4.1 Smith Predictor

A well-known method to compensate dead time is the Smith predictor, see for instance [Smith57], and [Levine10]. The Smith predictor uses an internal model $\tilde{\Sigma}$ to predict system states to overcome dead time. If the internal model of the Smith predictor represents exactly the real system and the dead time is known, then the dead time is compensated completely. However, there are always model uncertainties and disturbances, therefore the performance of the Smith predictor is restricted by its model accuracy.

The objective is to investigate the sensitivity of the Smith predictor to model uncertainties. In [HajduInsperger16] the Smith predictor is investigated using analytically calculated stability charts. In contrast, in this work the stability charts are calculated numerically and

additionally with information of the maximum absolute discrete eigenvalue and dominant damping ratio, as discussed in Sec. 5.3. In the following the closed loop equation of the overall system with Smith predictor is derived. All states and parameters of the compensation method are denoted with a tilde to distinguish them from states and parameters of the real system Σ.

The total time delay τ_{total} and discrete delayed steps n_{total} of the real system are given as

$$\tau_{total} = \tau_{act} + \tau_{ms}, \quad n_{total} = \frac{\tau_{total}}{T_0}, \tag{5.56}$$

with sampling time T_0, as shown in Eq. (5.26). The assumed time delay and delayed steps of the compensation method are defined as

$$\tilde{\tau}_{total} = \tilde{\tau}_{act} + \tilde{\tau}_{ms}, \quad \tilde{n}_{total} = \frac{\tilde{\tau}_{total}}{T_0}. \tag{5.57}$$

Figure 5.13 shows how the Smith predictor works. The calculated undelayed state $\tilde{\boldsymbol{x}}_k$ is predicted by the internal model of the Smith predictor $\tilde{\Sigma}$. The real system model is given as

$$\Sigma: \quad \boldsymbol{x}_{k+1} = \boldsymbol{A}_d \boldsymbol{x}_k + \boldsymbol{B}_d u_{total,k}. \tag{5.58}$$

On the other hand the internal model of the Smith predictor reads

$$\tilde{\Sigma}: \quad \tilde{\boldsymbol{x}}_{k+1} = \tilde{\boldsymbol{A}}_d \tilde{\boldsymbol{x}}_k + \tilde{\boldsymbol{B}}_d u_{total,k}. \tag{5.59}$$

In order to consider time delay, real system and Smith predictor model are augmented by delayed states as discussed in Sec. 5.2.2. Then, the augmented real system is defined as

$$\boldsymbol{x}_{a,k+1} = \boldsymbol{A}_{d,a} \boldsymbol{x}_{a,k} + \boldsymbol{B}_{d,a} u_{total,k}, \tag{5.60}$$

with augmented system matrix $\boldsymbol{A}_{d,a}$ calculated as given in Eq. (5.34), augmented state $\boldsymbol{x}_{a,k}$, as given in Eq. (5.33), and augmented input matrix $\boldsymbol{B}_{d,a}$ as given in Eq. (5.35). The

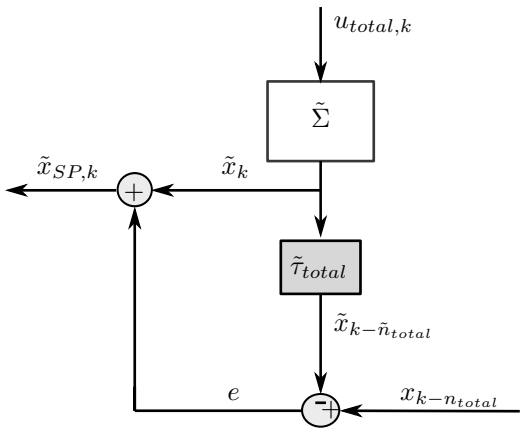

Figure 5.13: Compensation method Smith predictor.

real number of extended states reads

$$n_{ext} = n \cdot n_{total} = 2n_{total}, \tag{5.61}$$

as defined in Eq. (5.29).

Furthermore, the augmented internal model of the Smith predictor is defined as

$$\tilde{\boldsymbol{x}}_{a,k+1} = \tilde{\boldsymbol{A}}_{d,a}\tilde{x}_{a,k} + \tilde{\boldsymbol{B}}_{d,a}u_{total,k} \tag{5.62}$$

with augmented matrices and states as in the case of the real augmented system (5.60). The number of extended states of the prediction system is given as

$$\tilde{n}_{ext} = 2\tilde{n}_{total}. \tag{5.63}$$

However, the number of extended state $\tilde{n}_{ext}$ of the Smith predictor may differ from the number of extended state n_{ext} of the real system, in the case that the real time delay is not known exactly.

The prediction $\tilde{\boldsymbol{x}}_k$ from Eq. (5.59) is corrected by the error between predicted delayed state $\tilde{\boldsymbol{x}}_{k-\tilde{n}_{total}}$ from (5.62) and real delayed state $\boldsymbol{x}_{k-n_{total}}$ from (5.60). Then, the final state prediction of the Smith predictor reads

$$\tilde{\boldsymbol{x}}_{SP,k} = \tilde{\boldsymbol{x}}_k + \boldsymbol{x}_{k-n_{total}} - \tilde{\boldsymbol{x}}_{k-\tilde{n}_{total}}. \tag{5.64}$$

The next step is important to consider the overall system dynamics of the real system and the prediction system. The augmented state vector of the real system and the augmented state vector of the prediction system are put together to an overall state vector in order to calculate the overall closed loop system matrix. Thus, it yields

$$\begin{aligned}\boldsymbol{x}_{all,k} &= \left[\boldsymbol{x}_{a,k}^T, \tilde{\boldsymbol{x}}_{a,k}^T\right]^T \\ &= \left[\Delta\varphi_k, \Delta\omega_k, \ldots, \Delta\varphi_{k-n_{total}}, \Delta\omega_{k-n_{total}}, \Delta\tilde{\varphi}_k\Delta\tilde{\omega}_k, \ldots, \Delta\tilde{\varphi}_{k-\tilde{n}_{total}}, \Delta\tilde{\omega}_{k-\tilde{n}_{total}}\right]^T.\end{aligned} \tag{5.65}$$

Then, the overall system dynamics is given as

$$\boldsymbol{x}_{all,k+1} = \begin{bmatrix}\boldsymbol{A}_{d,a} & \boldsymbol{0} \\ \boldsymbol{0} & \tilde{\boldsymbol{A}}_{d,a}\end{bmatrix}\boldsymbol{x}_{all,k} + \begin{bmatrix}\boldsymbol{B}_{d,a} \\ \tilde{\boldsymbol{B}}_{d,a}\end{bmatrix}u_{total,k}. \tag{5.66}$$

For the sake of simplicity the reference $\boldsymbol{x}_{des,k}$ and the feedforward controller $u_{FF,k}$ is set to zero for stability analysis. Using Eq. (5.64), the feedback controller reads

$$u_{total,k} = u_{FB,SP} = -\boldsymbol{k}^T\tilde{\boldsymbol{x}}_{SP,k} = -\boldsymbol{k}^T\left(\tilde{\boldsymbol{x}}_k + \boldsymbol{x}_{k-n_{total}} - \tilde{\boldsymbol{x}}_{k-\tilde{n}_{total}}\right), \tag{5.67}$$

with control gain $\boldsymbol{k} = [p, d]^T$, see Eq. (5.41).

The Smith predictor controller $u_{FB,SP}$ can be rewritten to

$$u_{FB,SP} = -\boldsymbol{k}_{all,SP}^T\boldsymbol{x}_{all,k}, \tag{5.68}$$

as a function of the overall state vector $\boldsymbol{x}_{all}$. Hence, the overall control gain vector reads

$$\boldsymbol{k}_{all,SP} = \left[0, 0, \ldots, \underbrace{p, d}_{x_{k-n_{total}}}, \underbrace{p, d}_{\tilde{x}_k}, 0, \ldots, 0, \underbrace{-p, -d}_{\tilde{x}_{k-\tilde{n}_{total}}}\right]^T . \tag{5.69}$$

Applying the controller $u_{FB,SP}$ from Eq. (5.68) to the augmented overall system (5.66) yields

$$\boldsymbol{x}_{all,k+1} = \underbrace{\left(\begin{bmatrix} \boldsymbol{A}_{d,a} & \boldsymbol{0} \\ \boldsymbol{0} & \tilde{\boldsymbol{A}}_{d,a} \end{bmatrix} - \begin{bmatrix} \boldsymbol{B}_{d,a} \\ \tilde{\boldsymbol{B}}_{d,a} \end{bmatrix} \boldsymbol{k}_{all,SP}^T \right)}_{\tilde{\boldsymbol{A}}_{cl,SP}} \boldsymbol{x}_{all,k}. \tag{5.70}$$

Stability charts of the Smith predictor can be calculated now using closed loop system matrix $\tilde{\boldsymbol{A}}_{cl,SP}$.

5.4.2 Observer Based Method

The design of an observer is presented to predict undelayed states of the two-mass control system, described in (2.29). Similar to the Smith predictor, the observer compensation method uses measured delayed states $\boldsymbol{x}_{k-n_{total}}$ and the system input $u_{total,k}$ to predict undelayed states $\tilde{\boldsymbol{x}}_{obsv,k}$. Figure 5.14 illustrates the prediction scheme. Several observer methods can be applied for prediction. In this work a Luenberger observer, see [Luenberger64], is chosen due to its simplicity.

In order to predict the undelayed state $\tilde{\boldsymbol{x}}_{obsv,k}$, the observer is designed based on an augmented prediction system. The augmented prediction system from (5.62) is applied with augmented observer state vector $\tilde{\boldsymbol{x}}_{obsv,a,k}$ by $\tilde{n}_{total}$ delayed steps, see Eq. (5.57). Furthermore, the real system is also augmented by delayed steps, see Eq. (5.60) with augmented real state vector $\boldsymbol{x}_{a,k}$.

Using the augmented matrices and states, the Luenberger observer reads

$$\tilde{\boldsymbol{x}}_{obsv,a,k+1} = \tilde{\boldsymbol{A}}_{d,a}\tilde{\boldsymbol{x}}_{obsv,a,k} + \tilde{\boldsymbol{B}}_{d,a}u_{total,k} + \boldsymbol{L}\left(\boldsymbol{x}_{k-n_{total}} - \tilde{\boldsymbol{x}}_{obsv,k-\tilde{n}_{total}}\right), \tag{5.71}$$

with observer gain $\boldsymbol{L}$. The observer gain has the size $(2 + 2\tilde{n}_{total}) \times 2$. The number of rows is the system order of the augmented prediction system, see Eq. (5.28). Furthermore, the

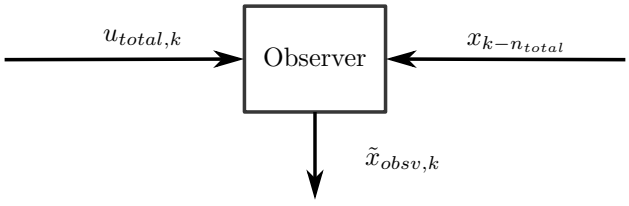

Figure 5.14: Observer to predict undelayed states.

first part is a model based prediction and the last term is the correction of the error between model based delayed prediction $\tilde{\boldsymbol{x}}_{obsv,k-\tilde{n}_{total}}$ and real delayed state $\boldsymbol{x}_{k-n_{total}}$ weighted by the observer gain $\boldsymbol{L}$.

The observer from (5.71) can be rewritten to

$$\tilde{\boldsymbol{x}}_{obsv,a,k+1} = \underbrace{\left(\tilde{\boldsymbol{A}}_{d,a} - \boldsymbol{L}\tilde{\boldsymbol{C}}_{d,a}\right)}_{=\tilde{\boldsymbol{A}}_{obsv,cl}} \tilde{\boldsymbol{x}}_{obsv,a,k} + \tilde{\boldsymbol{B}}_{d,a} u_{total,k} + \boldsymbol{L}\boldsymbol{C}_{d,a}\boldsymbol{x}_{a,k}, \tag{5.72}$$

with output matrices

$$\boldsymbol{C}_{d,a} = \begin{bmatrix} 0 & 0 & \dots & 0 & 1 & 0 \\ 0 & 0 & \dots & 0 & 0 & 1 \end{bmatrix} \in \mathbb{R}^{2\times(2+2n_{total})} \tag{5.73}$$

and

$$\tilde{\boldsymbol{C}}_{d,a} = \begin{bmatrix} 0 & 0 & \dots & 0 & 1 & 0 \\ 0 & 0 & \dots & 0 & 0 & 1 \end{bmatrix} \in \mathbb{R}^{2\times(2+2\tilde{n}_{total})}. \tag{5.74}$$

The number of columns of the output vectors are the system orders of the respective augmented systems. The observer gain can be found for instance by pole placing of the closed loop observer matrix $\tilde{\boldsymbol{A}}_{obsv,cl}$. For the investigated application here, the observer poles $\lambda_{obsv,i}$ are chosen approximately as a third of the discrete system poles $\lambda_{sys,i}$

$$\lambda_{obsv,i} \approx \frac{1}{3}\lambda_{sys,i}.$$

Thus, the state feedback controller using the undelayed predicted state reads

$$u_{FB,obsv} = -\boldsymbol{k}^T \tilde{\boldsymbol{x}}_{obsv,k}, \tag{5.75}$$

with control gain $\boldsymbol{k} = [p, d]^T$, see Eq. (5.41).

This feedback controller is rewritten in order to consider the whole system dynamics of the real system and the observer prediction system. The overall state vector $\boldsymbol{x}_{all,k}$ is the same as the overall state vector of the Smith predictor in Eq. (5.65). Then, the observer controller is rewritten to

$$u_{FB,obsv} = -\boldsymbol{k}_{all,obsv}^T \boldsymbol{x}_{all,k}, \tag{5.76}$$

with overall control gain

$$\boldsymbol{k}_{all,obsv} = \left[0, 0, \dots, \underbrace{0, 0}_{x_{k-n_{total}}}, \underbrace{p, d}_{\tilde{x}_k}, 0, \dots, 0, \underbrace{0, 0}_{\tilde{x}_{k-\tilde{n}_{total}}}\right]^T. \tag{5.77}$$

Applying the feedback controller, the closed loop system yields

$$\boldsymbol{x}_{all,k+1} = \underbrace{\left(\begin{bmatrix} \boldsymbol{A}_{d,a}, & 0 \\ \boldsymbol{L}\boldsymbol{C}_{d,a}, & \tilde{\boldsymbol{A}}_{d,a} - \boldsymbol{L}\tilde{\boldsymbol{C}}_{d,a} \end{bmatrix} - \begin{bmatrix} \boldsymbol{B}_{d,a} \\ \tilde{\boldsymbol{B}}_{d,a} \end{bmatrix} \boldsymbol{k}_{all,obsv}^T\right)}_{\tilde{\boldsymbol{A}}_{cl,obsv}} \boldsymbol{x}_{all,k}. \tag{5.78}$$

Stability charts of the closed loop system can be calculated using matrix $\tilde{\boldsymbol{A}}_{cl,obsv}$.

5.4.3 State Prediction

The state predictor calculates $\tilde{n}_{total}$ steps into the future in order to compensate the assumed total dead time $\tilde{\tau}_{total}$, as for instance applied in [VadamaluBeidl16]. The approach is recursive and model-based, however the actual delayed measurement $\boldsymbol{x}_{k-n_{total}}$ is used as initial condition in each prediction.

Using the prediction model $\tilde{\Sigma}$ from (5.59) the undelayed state can be calculated by the recursive law

$$\tilde{\boldsymbol{x}}_{pred,k} = \tilde{\boldsymbol{A}}_d^{\tilde{n}_{total}} \boldsymbol{x}_{k-n_{total}} + \sum_{i=0}^{\tilde{n}_{total}-1} \tilde{\boldsymbol{A}}_d^i \tilde{\boldsymbol{B}}_d u_{total,k-1-i}. \tag{5.79}$$

For instance to compensate the assumed dead time $\tilde{\tau}_{total} = 20\ ms$ with sampling time $T_0 = 5\ ms$, the prediction law reads

$$\tilde{\boldsymbol{x}}_{pred,k} = \tilde{\boldsymbol{A}}_d^4 \boldsymbol{x}_{k-4} + \tilde{\boldsymbol{A}}_d^3 \tilde{\boldsymbol{B}}_d u_{total,k-4} + \tilde{\boldsymbol{A}}_d^2 \tilde{\boldsymbol{B}}_d u_{total,k-3} + \tilde{\boldsymbol{A}}_d \tilde{\boldsymbol{B}}_d u_{total,k-2} + \tilde{\boldsymbol{B}}_d u_{total,k-1}. \tag{5.80}$$

Figure 5.15 illustrates inputs and output of the recursive state prediction. The input $u_{total,k}$ is delayed by one, two, ..., $\tilde{n}_{total}$ time steps illustrated by $z^{-1}, z^{-2}, \ldots, z^{-\tilde{n}_{total}}$.

The delayed inputs $u_{total,k-1}, u_{total,k-2}, \ldots, u_{total,k-\tilde{n}_{total}}$ are necessary for prediction. Its dynamics can be described as a chain of integrator and read

$$\tilde{\boldsymbol{x}}_{u,k+1} = \underbrace{\begin{bmatrix} 0 & 0 & \ldots & 0 & 0 \\ 1 & 0 & \ldots & 0 & 0 \\ \vdots & \ddots & & & \vdots \\ 0 & 0 & \ldots & 1 & 0 \end{bmatrix}}_{\tilde{\boldsymbol{A}}_u} \tilde{\boldsymbol{x}}_{u,k} + \underbrace{\begin{bmatrix} 1 \\ 0 \\ \vdots \\ 0 \end{bmatrix}}_{\tilde{\boldsymbol{B}}_u} u_{total,k}. \tag{5.81}$$

with input state $\tilde{\boldsymbol{x}}_{u,k} = [u_{total,k-1}, u_{total,k-2}, \ldots, u_{total,k-\tilde{n}_{total}}]^T$.

A state feedback controller uses the undelayed predicted state from Eq. (5.79) and is given as

$$u_{FB,pred} = -\boldsymbol{k}^T \tilde{\boldsymbol{x}}_{pred,k}, \tag{5.82}$$

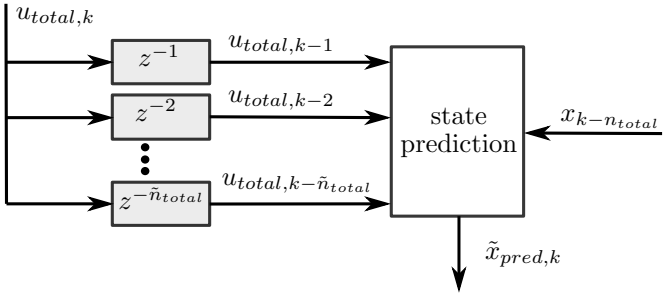

Figure 5.15: Compensation using a recursive state prediction method.

with control gain

$$\boldsymbol{k} = [p, d]^T \in \mathbb{R}^2. \tag{5.83}$$

In order to calculate the closed loop stability, an overall state vector is constructed with real system states and input states. It is

$$\begin{aligned} \boldsymbol{x}_{all,u,k} &= \left[\boldsymbol{x}_{a,k}^T, \tilde{\boldsymbol{x}}_{u,k}^T\right]^T \\ &= \left[\boldsymbol{x}_k^T, \boldsymbol{x}_{k-1}^T, \ldots, \boldsymbol{x}_{k-n_{total}}^T, u_{total,k-1}, u_{total,k-2}, \ldots, u_{total,k-\tilde{n}_{total}}\right]^T. \end{aligned} \tag{5.84}$$

Using the overall state vector and the prediction law (5.79), the prediction controller from Eq. (5.82) can be rewritten to

$$\begin{aligned} u_{FB,pred} = &- \boldsymbol{k}^T \tilde{\boldsymbol{A}}_d^{\tilde{n}_{total}} \boldsymbol{x}_{k-n_{total}} - \boldsymbol{k}^T \tilde{\boldsymbol{B}}_d u_{total,k-1} - \boldsymbol{k}^T \tilde{\boldsymbol{A}}_d \tilde{\boldsymbol{B}}_d u_{total,k-2} - \\ &\ldots - \boldsymbol{k}^T \tilde{\boldsymbol{A}}_d^{\tilde{n}_{total}-1} \tilde{\boldsymbol{B}}_d u_{total,k-\tilde{n}_{total}}. \end{aligned} \tag{5.85}$$

The equation can be further reformulated to

$$u_{FB,pred} = -\boldsymbol{k}_{all,pred}^T \boldsymbol{x}_{all,u,k}, \tag{5.86}$$

with

$$\boldsymbol{k}_{all,pred} = \left(\left[0, 0, \ldots, 0, \boldsymbol{k}^T \tilde{\boldsymbol{A}}_d^{\tilde{n}_{total}}, \boldsymbol{k}^T \tilde{\boldsymbol{B}}_d, \boldsymbol{k}^T \tilde{\boldsymbol{A}}_d \tilde{\boldsymbol{B}}_d, \ldots, \boldsymbol{k}^T \tilde{\boldsymbol{A}}_d^{\tilde{n}_{total}-1} \tilde{\boldsymbol{B}}_d\right]\right)^T \tag{5.87}$$

and control gain $\boldsymbol{k}^T$ from (5.83).

Hence, the closed loop system is given as

$$\boldsymbol{x}_{all,u,k+1} = \underbrace{\left(\begin{bmatrix} \boldsymbol{A}_{d,a} & 0 \\ 0 & \tilde{\boldsymbol{A}}_u \end{bmatrix} - \begin{bmatrix} \boldsymbol{B}_{d,a} \\ \tilde{\boldsymbol{B}}_u \end{bmatrix} \boldsymbol{k}_{all,pred}^T\right)}_{\tilde{\boldsymbol{A}}_{cl,pred}} \boldsymbol{x}_{all,u,k}. \tag{5.88}$$

Stability properties can be analyzed using overall closed loop prediction matrix $\tilde{\boldsymbol{A}}_{cl,pred}$.

5.5 Simulation Applications - Comparison of the Compensation Methods

Following from the stability charts from Fig. 5.9 and Fig. 5.10 dead time compensation methods are necessary to enable effective powertrain control in the presence of time delay. Therefore, in the previous section compensation methods were presented and the respective closed loop system matrices were derived. In this section, these compensation methods are compared using the derived closed loop system matrices by constructing stability charts. The assumed stiffness parameter and dead time of the prediction models are varied in order to evaluate robustness to model uncertainty. Furthermore, the compensation methods are compared in time simulation, using the detailed battery electric powertrain model, described in Sec. 2.4.1.

5.5.1 Stability Diagrams

In the ideal case, the prediction model $\tilde{\boldsymbol{A}}_d, \tilde{\boldsymbol{B}}_d$ corresponds to the real system $\boldsymbol{A}_d, \boldsymbol{B}_d$ and the assumed total dead time $\tilde{\tau}_{total}$ is equal to the real dead time τ_{total}. Hence, all three compensation methods Smith predictor, observer based method, and state prediction can fully compensate the dead time and the closed loop system behaves like there is no dead time. Consequently, the stability diagrams of the compensation methods for various time delay are equal to the diagrams on the left in Fig. 5.9 and Fig. 5.10 for $\tau = 0\ ms$.

However, the ideal case is not a realistic scenario, therefore it is necessary to investigate robustness of the compensation methods to model uncertainties. Exemplary, the total time delay of $\tau_{total} = 20\ ms$ is chosen. Stiffness $\tilde{c}$ and dead time $\tilde{\tau}$ of the prediction system are varied separately. The stiffness of the prediction system is varied by $\pm 20\%$ and the assumed dead time is set to $\tilde{\tau} = 15\ ms$ and to $\tilde{\tau} = 25\ ms$ in each case.

5.5.1.1 Variation of Stiffness

A variation of the stiffness parameter has a major influence on the frequency of the system. For instance a variation of $\tilde{c} = \gamma c$ with $\gamma \in \mathbb{R}$ affects the natural frequency of the system by the factor $\sqrt{\gamma}$, as given in Eq. (3.29). Thus, a reduction of 20% of the system stiffness results in a reduction of 11% of the assumed natural frequency. On the other hand, an increase of 20% of the system stiffness results in an increase of 9.5% of the assumed natural frequency.

Figure 5.16 and Fig. 5.17 shows the stability plots using the compensation methods Smith predictor, observer based method, and state prediction with underestimated stiffness parameter. The stability regions are comparably large to the real system without dead time. The stability regions of the observer based method and state prediction are even larger than of the Smith Predictor and very similar to each other. By contrast the damping behavior of the underestimated Smith predictor is low.

The stability charts of overestimated stiffness parameter can be seen in Fig. 5.18 and Fig. 5.19. The stability regions are significantly smaller than in the underestimation case. Especially, the stability region of the Smith predictor is strongly reduced. The stability charts of the observer based method and state prediction are again very similar. Hence, the destabilizing effect of parameter mismatch can be clearly seen for stiffness overestimation. Furthermore, an overestimation of the stiffness parameter is much worse than an underestimation, since overestimation deteriorates the stability much more.

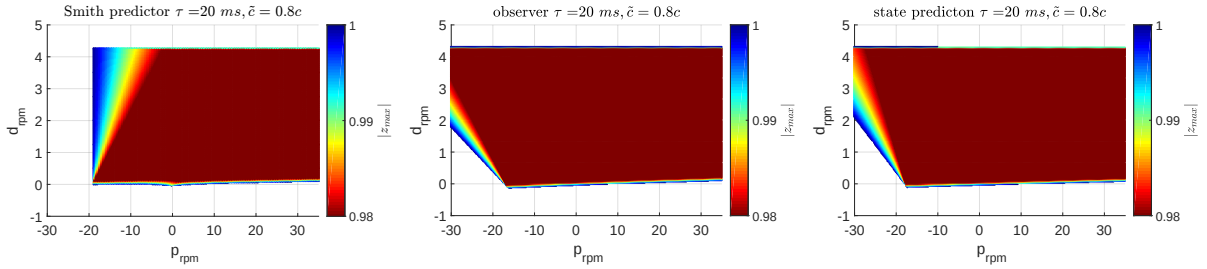

Figure 5.16: Numerically calculated stability charts with color coded maximum absolute value and underestimated stiffness $\tilde{c} = 0.8c$ for various compensation methods.

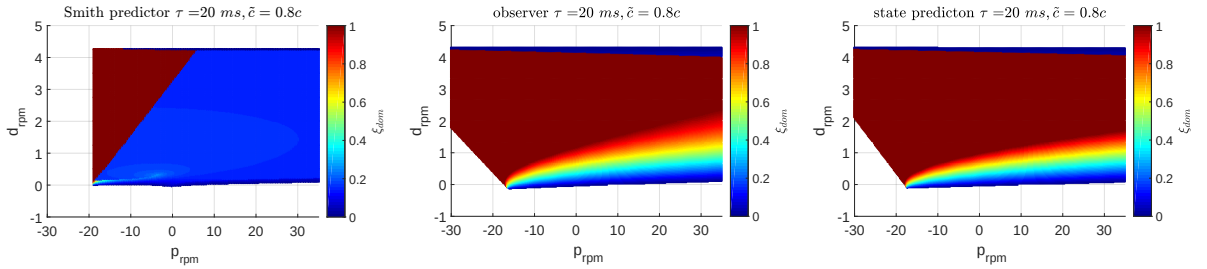

Figure 5.17: Numerically calculated stability charts with color coded damping ratio and underestimated stiffness $\tilde{c} = 0.8c$ for various compensation methods.

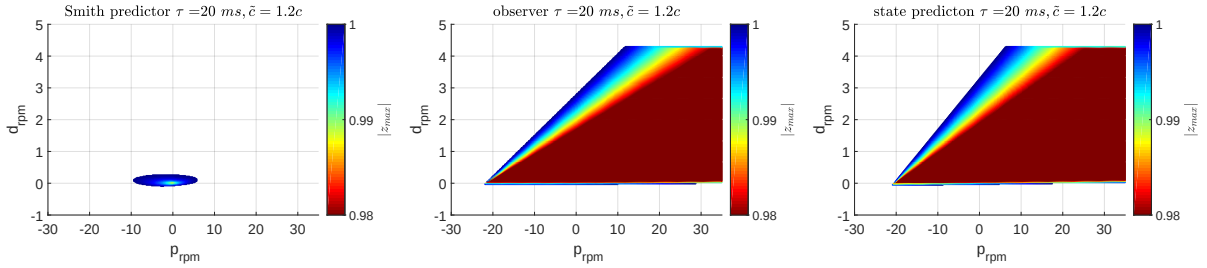

Figure 5.18: Numerically calculated stability charts with color coded maximum absolute value and overestimated stiffness $\tilde{c} = 1.2c$ for various compensation methods.

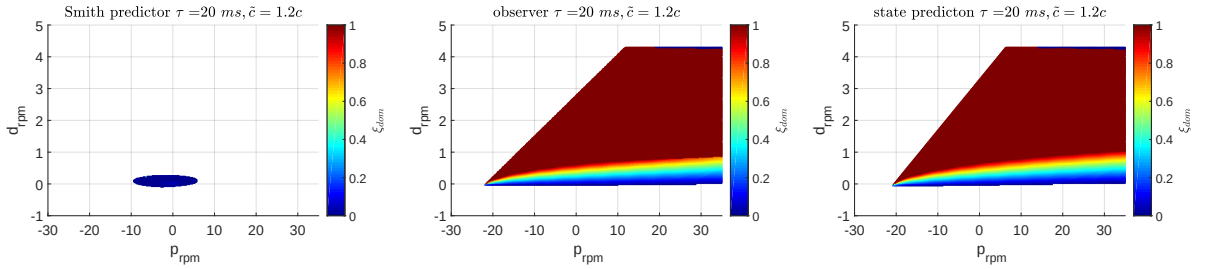

Figure 5.19: Numerically calculated stability charts with color coded damping ratio and overestimated stiffness $\tilde{c} = 1.2c$ for various compensation methods.

5.5.1.2 Variation of Dead Time

A variation of the prediction dead time $\tilde{\tau}_{total}$ changes the amount of delayed steps $\tilde{n}_{total}$, see Eq. (5.57) and therefore, the system order of the augmented prediction system and the amount of prediction steps change, respectively. Stability charts are calculated for $\tilde{\tau}_{total} = 15\ ms$ and $\tilde{\tau}_{total} = 25\ ms$, but the real dead time is defined as $\tau_{total} = 20\ ms$.

Figure 5.20 and Fig. 5.21 shows the stability plots using the compensation methods with underestimated dead time. The underestimation reduces the stability regions. The stability region of the Smith predictor is reduced most. Compensation using the observer based method have the largest stability region.

The stability charts of overestimated dead time are illustrated in Fig. 5.22 and Fig. 5.23. The size of the stability regions are comparable the case of underestimated dead time. The stability region of the observer based method is again the largest and the region of the Smith predictor is very small. In contrast to the variation of the stiffness parameter, the underestimation or overestimation of the dead time leads to similar reduction of the stability region. However, an overestimation is preferred due to the slightly greater stability regions.

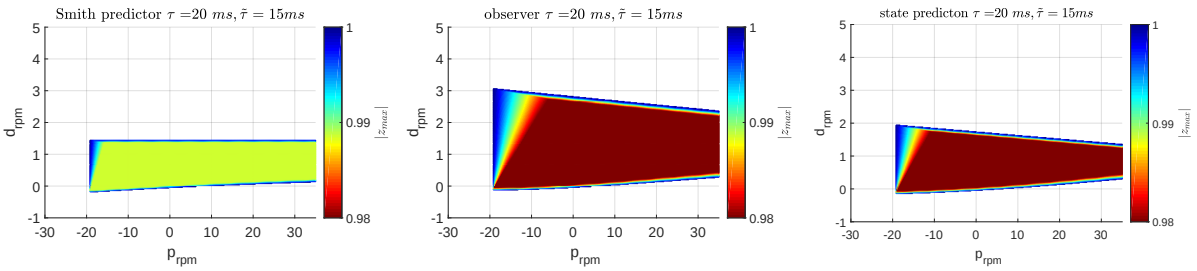

Figure 5.20: Numerically calculated stability charts with color coded maximum absolute value and underestimated dead time $\tilde{\tau} = 15\ ms$ for various compensation methods.

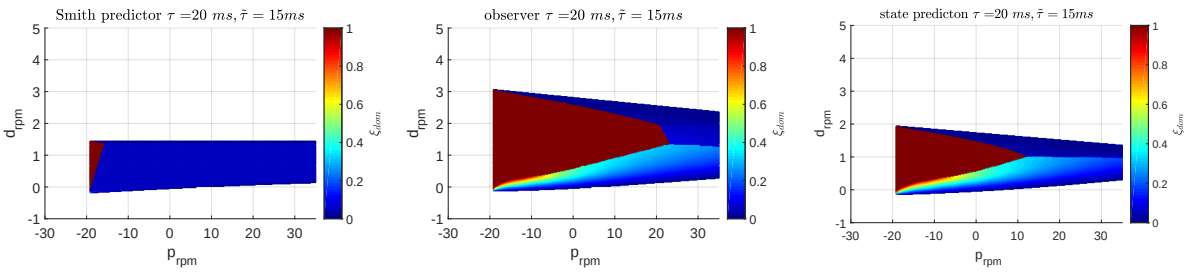

Figure 5.21: Numerically calculated stability charts with color coded damping ratio and underestimated dead time $\tilde{\tau} = 15\ ms$ for various compensation methods.

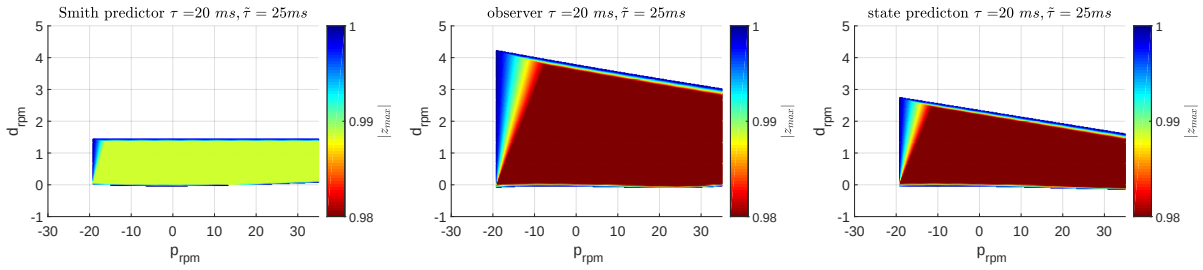

Figure 5.22: Numerically calculated stability charts with color coded maximum absolute value and overestimated dead time $\tilde{\tau} = 25\ ms$ for various compensation methods.

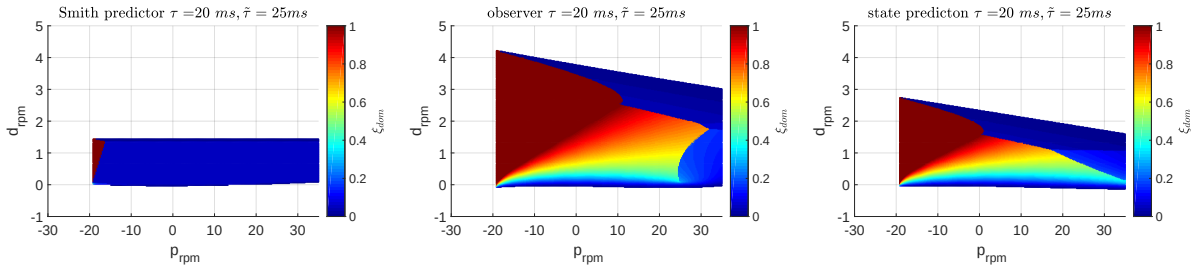

Figure 5.23: Numerically calculated stability charts with color coded damping ratio and overestimated dead time $\tilde{\tau} = 25\ ms$ for various compensation methods.

5.5.2 Time Simulation

All three compensation methods Smith predictor, observer based method, and state prediction method are used in simulation of the detailed battery electric powertrain model, described in Sec. 2.4.1. An overall dead time $\tau = 20\ ms$ is implemented in the simulation model. Moreover, a state feedback controller with control gains $p_{rpm} = 0$ and $d_{rpm} = 1$ is chosen.

Time simulation shows that the powertrain system becomes unstable in the presence of time delay τ, when no compensation methods are applied. On the other hand, as shown in the previous section the control system is stable using one of the presented compensation methods even for varied stiffness and dead time parameters. Evidence for this applied to the detailed model is depicted in Fig. 5.24. The vehicle acceleration a_{VEH} is stable for various compensation methods. As indicated by the stability plots, shown in the previous section, the observer based method and state prediction method have the best damping behavior. Furthermore, the Smith predictor with overestimated stiffness parameter $\tilde{c} = 1.2\ c$ tends to be unstable. However, the steady-state behavior of the observer and state prediction method implies an offset error due to model uncertainties originating from the detailed model.

The steady-state error can be corrected by introducing the error integral $y_{int} = \int (x_{1,des} - x_1)\, dt$ as a new state. The new state is added to the control loop and is controlled to zero. Figure 5.25 shows the simulation results with error integral. The

steady-state error is eliminated, however an strong overshoot is still present for $\tilde{c} = 1.2c$ and $\tau = \tilde{2}5\ ms$.

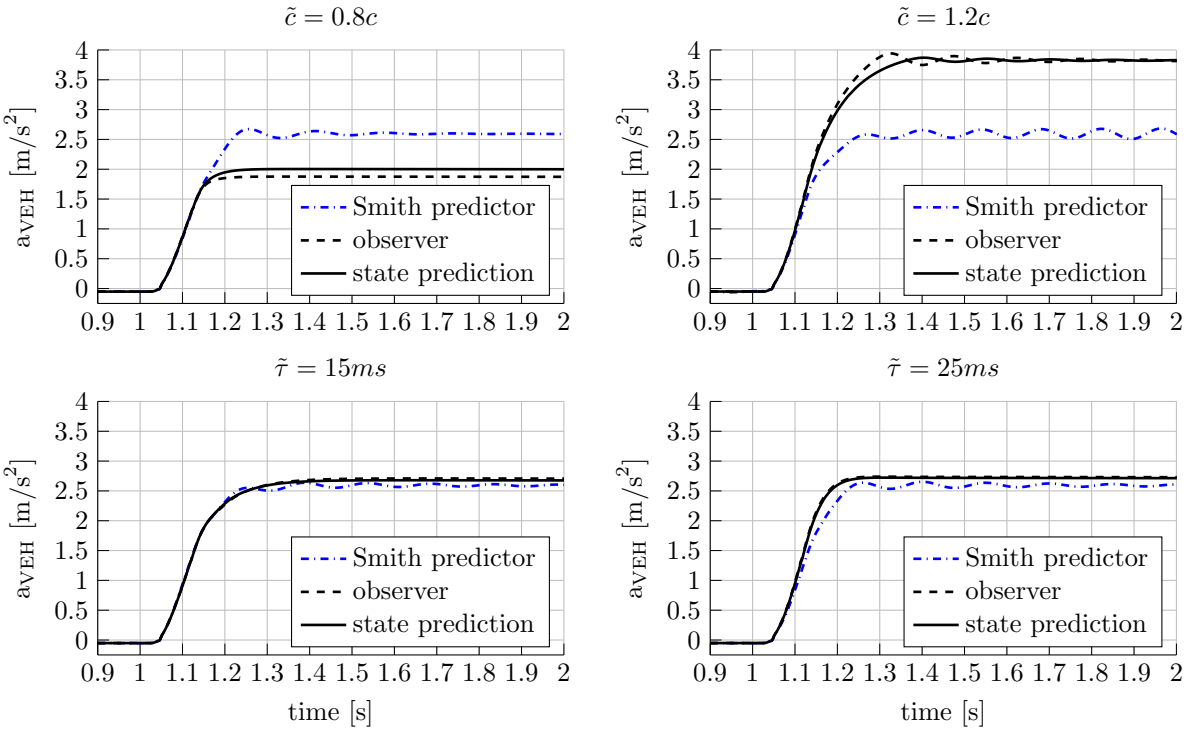

Figure 5.24: Simulation of load changes with dead time in the system and using different compensation methods. The stiffness and dead time parameter of the compensation methods are varied to investigate robustness.

5.5.3 Summary

All dead time compensation methods can control the system in the presence of dead time $\tau = 20\ ms$. Investigations of robustness to model uncertainties show that if the stiffness parameter is not known exactly, it should be underestimated rather than overestimated. Furthermore, the sensitivity to dead time is not as critical as to the stiffness. However, an overestimation of the dead time lead to slightly greater stability regions than for underestimation, as shown in Fig.5.20, Fig. 5.21, Fig. 5.22, and Fig. 5.23. The Smith predictor is most sensitive to model uncertainties and the observer based method and state prediction method show the best robustness in the stability charts. However, observer based method and state prediction method lead to a steady-state error due to model uncertainties, as visible in time simulation. When the error integral is introduced as a new state and is controlled to zero, the error can be eliminated. The evaluation of the methods are summarized in Tab. 5.3.

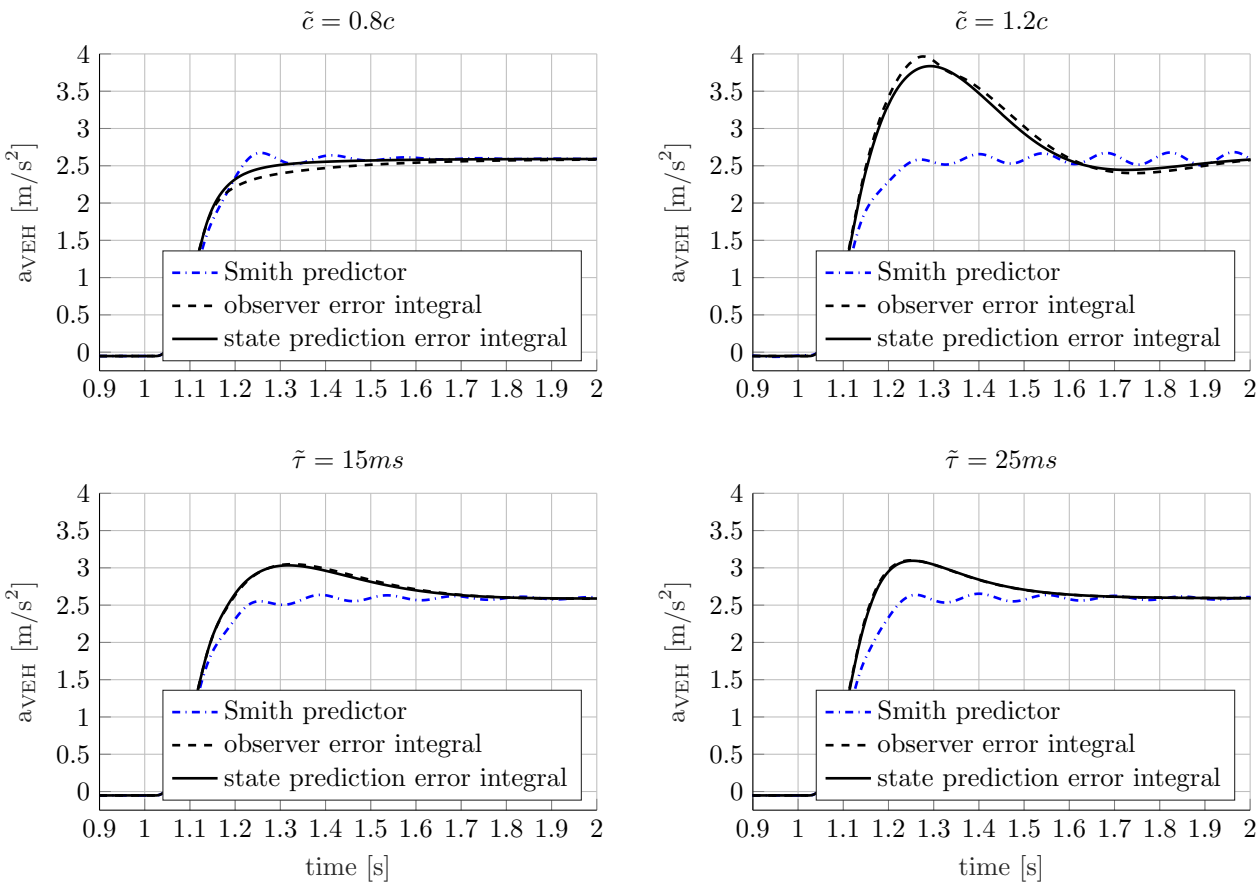

Figure 5.25: Simulation of load changes with dead time in the system and using different compensation methods with additional error integrator.

	Smith predictor	observer based method	state prediction
$\tilde{c}$ underestimation	++	++	++
$\tilde{c}$ overestimation	− −	+	+
$\tilde{\tau}$ underestimation	-	+	+
$\tilde{\tau}$ overestimation	-	++	++

Table 5.3: Evaluation of compensation methods.

Chapter 6

An Ad Hoc Control Approach for Powertrains with Backlash and Time Delay

The previous two chapters investigated independently in detail backlash and time delay in powertrain control. Suitable control methods were developed for each. Now, this chapter presents first results of an ad hoc approach, which connects both methods. The previously derived control concepts are combined by a switching controller to enable smooth backlash control with dead time compensation. Even if the subsystems are all asymptotically stable, switching between these systems can enable instability, see [LiberzonMorse99] or [Liberzon03]. Therefore, the system dynamics of the switched systems is investigated in simulation. Here, the battery electric powertrain is considered as application. The switched system is designed based on the corresponding two-mass control model from Eq. (2.29) and simulations are based on the detailed simulation model from Sec. 2.4. Backlash and time delay are considered as discussed in Sec. 4.4 and Sec. 5.5, respectively.

6.1 Smoothed Backlash Control with Dead Time Compensation

Backlash is traversed during load changes from pull to thrust condition and vice versa. The hard nonlinearity of backlash dynamics leads to enhanced powertrain oscillations of the uncontrolled system. Therefore, a control method using a smooth backlash model was derived in Chapter 4. The control method includes a nonlinear flatness-based feedforward controller and an output feedback controller using smooth desired trajectories. However, this method can lead to an unstable control loop, when time delay is present. The destabilizing effect of time delay in general was analyzed in Chapter 5. Compensation

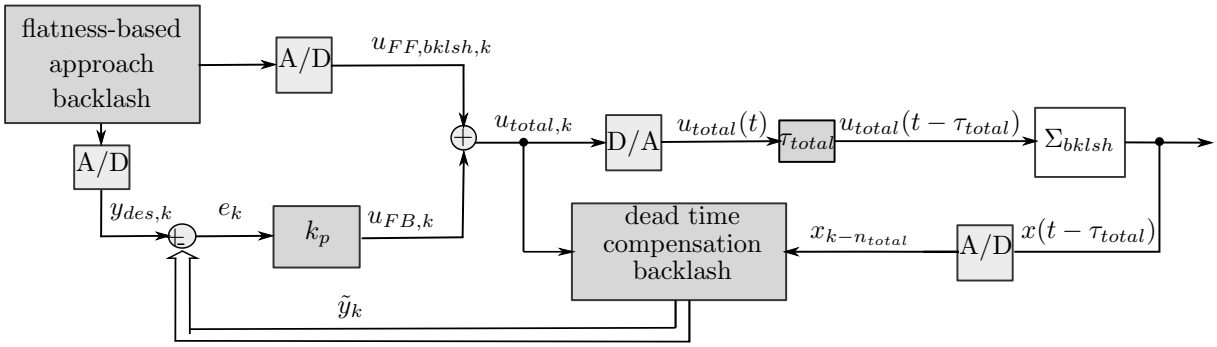

Figure 6.1: Overall control loop with backlash and dead time control.

methods were presented, but for linear systems. Hence, an adaption of the backlash method as well as of the dead time compensation method is necessary.

The adapted overall control loop structure for control of backlash and time delay is shown in Fig. 6.1. Following Sec. 4.3, the flatness-based feedforward controller $u_{FF,bklsh}(t)$ using a smooth backlash model is applied as derived in Eq. (4.17) for a two-mass control model. The desired trajectory $y_{des}(t)$ is the first derivative of the desired flat output $z_{des}(t)$ as discussed in Sec. 4.3.3. Both, feedforward controller and the corresponding desired trajectory have to be discretized in the digital control loop.

Furthermore, the backlash output feedback controller with control gain k_p is complemented by a time delay compensation method using a backlash model. For dead time compensation, the state prediction method from Sec. 5.4.3 is chosen, since the previous chapter shows that this method is robust to uncertainties and a simple recursive law, see Eq. (5.79), is applied. In contrast to the observer based method, no Riccati equation has to be solved in advance using this approach. In the following, the state predictor using a linear piece-wise defined backlash model is derived.

Switching Feedback Control

The recursive prediction law, Eq. (5.79), applies the discrete prediction system matrix $\tilde{\boldsymbol{A}}_d$ and prediction input matrix $\tilde{\boldsymbol{B}}_d$. These matrices have to represent the backlash dynamics. A well suited backlash model for state prediction is the dead zone model, as presented in Sec. 4.2, since it is piece-wise linear and the matrices can be constructed.

The dead-zone model is formulated with three separate linear functions and therefore a switching system is given. The condition for switching depends on the state torsion rotation angle $\Delta\varphi$. Figure 6.2 illustrates the state machine of this switched system.

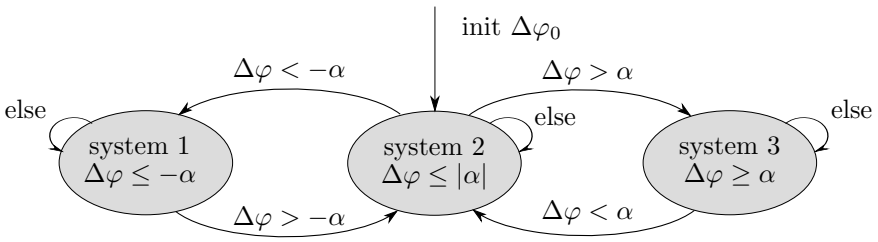

Figure 6.2: State machine for choosing the prediction system.

For initial state $\Delta\varphi_0 = 0$ the system starts at system 2, which is the backlash gap mode. When the torsion rotation angles becomes greater than half backlash gap α, then right system 3 is active, which is the positive contact mode. On the other hand, when the torsion rotation angle $\Delta\varphi$ becomes smaller than half negative backlash gap $-\alpha$, then left system 1 is active, which is the negative contact mode.

The two-mass control model with dead-zone for backlash gap 2α is rewritten as a switching system. An additional constant state Λ is introduced for the backlash gap offset. The constant reads

$$\Lambda = \Lambda_0 = \Theta c \alpha, \tag{6.1}$$

with summarized moments of inertia Θ, spring stiffness c, and half backlash gap α.

Bringing the two-mass control model from Eq. (3.12) together with dead-zone model from Eq. (4.3), yields the following three systems:

System 1 negative contact mode:

$$\begin{aligned} \Delta\dot{\varphi} &= \Delta\omega, \\ \Delta\dot{\omega} &= -\Theta c \Delta\varphi - \Theta d \Delta\omega - \Lambda + \frac{1}{J_1 R} u, \\ \dot{\Lambda} &= 0. \end{aligned} \tag{6.2}$$

System 2 backlash gap mode:

$$\begin{aligned} \Delta\dot{\varphi} &= \Delta\omega, \\ \Delta\dot{\omega} &= \frac{1}{J_1 R} u, \\ \dot{\Lambda} &= 0. \end{aligned} \tag{6.3}$$

System 3 positive contact mode:

$$\begin{aligned} \Delta\dot{\varphi} &= \Delta\omega, \\ \Delta\dot{\omega} &= -\Theta c \Delta\varphi + \delta - \Theta d \Delta\omega + \Lambda + \frac{1}{J_1 R} u, \\ \dot{\Lambda} &= 0. \end{aligned} \tag{6.4}$$

The initial conditions of all three systems are given as

$$\Delta\varphi(0) = \Delta\varphi_0, \quad \Delta\omega(0) = \Delta\omega_0, \quad \delta(0) = \Theta c \alpha. \tag{6.5}$$

The only difference between system 1 and system 3 is the sign of the constant Λ. The three systems are discretized in each case for state prediction. The resulting discrete system matrices are $\tilde{\boldsymbol{A}}_{d,1}, \tilde{\boldsymbol{A}}_{d,2}, \tilde{\boldsymbol{A}}_{d,3}$ and the input matrices read $\tilde{\boldsymbol{B}}_{d,1}, \tilde{\boldsymbol{B}}_{d,2}, \tilde{\boldsymbol{B}}_{d,3}$. The appropriate system and input matrices are then chosen depending on the actual torsion rotation angle $\Delta\varphi$ and are then applied to the state prediction law from Eq. (5.79). Hence, dead time compensation using a backlash powertrain control model is realized.

6.2 Application

The overall control strategy of smoothed backlash control with dead time compensation is validated by simulation. The simulation model is the detailed battery electric vehicle and includes several backlashes as described in Sec. 4.4. Furthermore, the model is transformed to a digital control systems with control sampling time $T_0 = 5\ ms$ and the total dead time $\tau_{total} = 20\ ms$ is added to the system. Figure 6.3 shows the simulation results including electric machine torque u and vehicle acceleration a_{VEH}.

The backlash control strategy from Chapter 4 with no compensation method is compared to the overall control strategy with compensation method from this chapter. The controlled system without dead time compensation becomes unstable. However, the system with smoothed backlash control and dead time compensation realizes stable, fast, and comfortable backlash traversing.

This example illustrates the potential of the method. The investigations in this chapter are however only a first outlook. Further studies are necessary with regard to stability and sensitivity to model uncertainties.

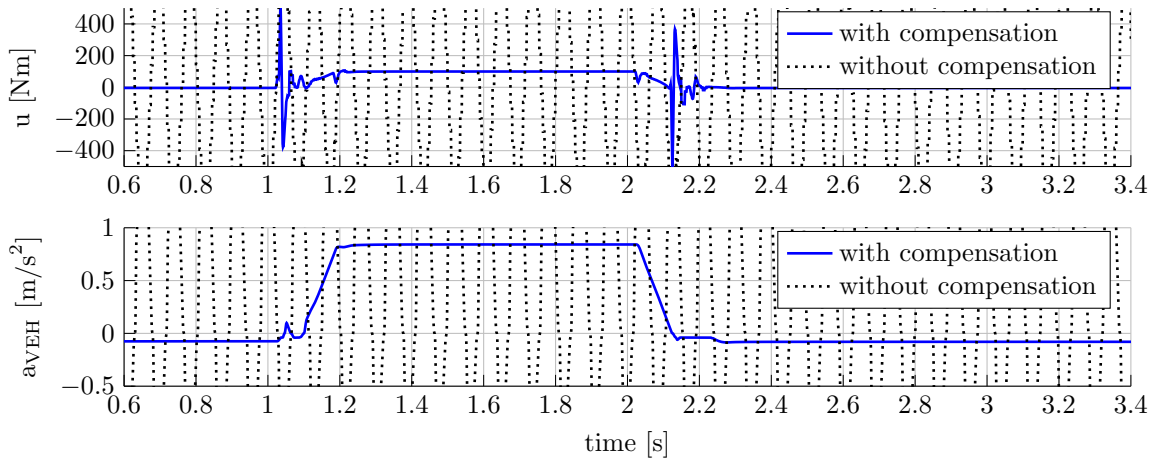

Figure 6.3: Simulation of load changes with the detailed battery electric powertrain model using the backlash control approach with and without dead time compensation.

Chapter 7

Conclusions

In this dissertation the problem of reducing driveline oscillations by using control methods was studied. Contributions to modeling and control of conventional, hybrid electric, and battery electric powertrains were given. The derived methods in this thesis provide improved control performance to the still very challenging problem of powertrain control with backlash and time delay. In the following, key contributions are summarized and discussed. An outlook concludes the dissertation.

7.1 Summary and Discussion

The ongoing in-depth changes in automotive development require to use all available leverage to increase performance, comfort, and component protection. Besides mechanical solutions, electronic control functions make a significant contribution to fulfill the mentioned requirements. Much research in recent years has focused on the design of control functions. Thereby, driveline oscillations play an important role, since the negative impact of these vibrations are in particular loss of drive performance, reduced comfort and high component load. Driveline oscillations can be induced to the powertrain by changes of the steady-state or by disturbances. Especially, low frequencies are dominant during launching or load changes and are very uncomfortable, since the oscillation frequency coincide with the eigenfrequency of the human stomach. There exists several studies on control to reduce driveline oscillations. However, few studies have investigated the dynamics and control design of conventional, hybrid electric, and battery electric powertrains at once. Furthermore, there is a lack of research on feedforward control design for powertrains and there remains a need for more investigations on control design of powertrains with dominant effects of backlash and time delay. These effects of backlash and time delay are still challenging and often lead to unsatisfactory control performance, as for example deteriorated tracking performance or even destabilized closed loop system.

Chapter 2: Driveline Oscillation Dynamics

In Chapter 2 this thesis contributes detailed multibody simulation models and reduced control models for conventional, hybrid electric, and battery electric powertrains. It is shown that the deflection shapes of all three powertrain types are similar for the lowest dominant frequency, see Fig. 2.27, and could be represented by two-mass control models. For conventional and battery electric powertrains, two-mass control models are applied. However, for hybrid electric powertrains an additional mass is necessary due to the two drive units, combustion engine and electric machine. Hence, a three-mass control model is derived for hybrid electric powertrains. Simulation results show oscillations with high amplitudes and slow decay for load changes and launching using the detailed powertrain models. The dominant frequencies are between 2 to 8 Hz. Load changes by electric machines cause particularly bad vibration behavior due to the high agility of the actuator. Furthermore, simulations show that the control models can represent the investigated undesired driveline oscillations and sufficiently correspondent with the detailed simulation models. The control models are the basis for the subsequent control designs and the detailed models are applied for simulative evaluation of the control functions besides test drives.

Chapter 3: Linear Powertrain Control

In Chapter 3 the findings from the analysis of the driveline oscillation dynamics are used for the design of linear powertrain control. First, the two-mass and three-mass control models are reformulated to separate the rigid body mode from the investigated oscillation mode. Then, the uncontrolled damping behavior is analyzed using the control models. On that basis, the desired dynamical behavior is defined, including critically damped step response, independent transition time, and controlled transient behavior. The demand of freely selectable transition time in this work, provide more agile driving and therefore, requires more advanced control methods than for instance torque built-up by ramps with predefined transition time.

One of the main contributions in this work is the presented model-based linear transient control approach in Sec. 3.4. The linear control approach enables to fulfill the stated desired dynamical behavior. At the beginning, the pedal position of the driver is interpreted, afterwards desired trajectories are planned, then feedforward-, feedback controller are calculated and finally, the total desired torque at the actuators of the powertrain is given, see Fig. 3.6. There exists several methods to design a feedforward controller. Flatness-based feedforward control is chosen in this thesis due to several aspects. First, differentially flatness theory provides exact system inversion for arbitrary transition time and no delay is added. Second, desired trajectories of the system states are generated in this approach, which are necessary for feedback control of transient dynamics. And finally, the method

can be used in particular for nonlinear system. This is advantageous, since the linear powertrain is later extended by dynamics from backlash and time delay. The benefits of this method become apparent if it is compared to input shaping, which is an another comment feedforward control method. Input shaping introduces delay, does not provide desired trajectories of the system states and cannot be applied to nonlinear systems.

The flatness-based feedforward control approach is derived for two-mass and three-mass control model, since these two models cover the three powertrain types. Then, pole-placement and proportional output are discussed for feedback control with the aim to provide critical damping behavior.

Then, based on the derived linear control models, a flatness-based feedforward controller is designed with freely chosen transition time to prevent driveline oscillations. Furthermore, the flatness-based approach generates desired trajectories for feedback control. These trajectories are used by a feedback controller to ensure well-damped oscillation behavior, even in the transient section of load changes. Additionally to feedback control, an approach for disturbance rejection is given, since the previous derived feedforward and feedback methods assumed that the disturbance is zero or compensated to zero.

The derived linear powertrain control approach is validated in simulation studies and experimentally with test vehicles. Both, simulation and experimental results, are encouraging and show the high potential of the presented method, since the desired specifications critically damped, independent transition time, and controlled transient behavior are reached.

Chapter 4: Powertrain Control with Backlash

The linear controller from Chapter 3 does not consider the dynamics of backlash. During load changes from pull to thrust condition and vice versa, backlash gap is traversed. The dynamics of backlash is highly nonlinear, since no torque is transmitted in the backlash phase, but when the first contact is achieved, torque is abruptly introduced. Therefore, Chapter 4 investigates the effects of backlash on the system dynamics and backlash models are presented. A dead-zone model, which represents the dynamics of backlash sufficiently accurate, are used for simulation. For control, a smooth backlash model is derived, since this model is integrated into the flatness-based control approach from Chapter 3 and differentiable functions are required for the approach. The main contributions in Chapter 4 are the derivation of a smooth model for backlash and the design of nonlinear differentially flat feedforward controllers for two-mass and three-mass control models. The feedforward controllers are based on the derived smooth backlash models and enables load changes from pull to thrust condition and vice versa with reduced driveline oscillations. An output feedback controller is added to better follow the desired trajectories, generated by the flatness-based approach. Simulation studies show the successful validation of the backlash

models and nonlinear feedforward control laws. Furthermore, simulation of the detailed hybrid electric powertrain with backlash presents improved oscillation damping using the nonlinear feedforward control approach compared to the linear approach. Finally, the overall nonlinear approach with feedforward and feedback controller is compared in simulations with the linear overall approach from Chapter 3. Both approaches provide vibration free backlash traversing. However, the nonlinear approach enables additionally much faster traversing. More detailed analysis show that the feedback controller of the nonlinear approach has high torque interventions. This indicates that the feedforward controller alone cannot enable vibration free and fast backlash traversing, due to model uncertainties, and an additional feedback controller is necessary.

Chapter 5: Powertrain Control with Time Delay

This chapter contributes analysis and control design of powertrains with time delay. Investigations on time delay are important, since the dynamics of time delay may not only degrade the tracking performance of controlled systems, but it can also destabilize the closed loop system. Powertrain control systems contain usually time delay due to electric and mechanical reasons. For instance signal processing, time sampling, and physical delayed behavior of actuators can lead to delay.

First, reasons for time delay in powertrain systems are discussed and the control system is converted to a digital control system in order to take sampling time into account. Second, two-mass and three-mass control models are discretized and time delay were added to the discretized system representation. The third section provide a straightforward numerical approach to calculate stability diagrams for discrete systems with time delay. Furthermore, the approach offers visualization of the degree of stability and damping ratio of the time delayed system. Stability diagrams are calculated to show the effect of time delay to a system with state feedback and to visualize the delay margin of these systems. It is shown for the controlled discrete two-mass powertrain system with state feedback that the damping behavior is greatly restricted by time delay greater than 20 ms.

Therefore, time delay compensation methods are presented and compared in the forth and fifth section. The methods Smith predictor, observer based compensator, and state prediction are designed for the two-mass control model of a battery electric powertrain and the belonging closed loop system matrices were derived. Using the derived closed loop system matrices, stability charts are calculated, besides time simulation, to evaluate sensitivities of these methods to parameter uncertainties. Simulation results show compensated dead time. Best results can be achieved using the observer based method and state prediction. If there are disturbances or greater model uncertainties in the time simulations, then it is suggested to introduce the error integral as a new state and control it to zero. Then, the steady-state error can be eliminated, but on the other hand overshoot appear. Therefore,

further investigations on eliminating steady-state error without overshooting could be promising to improve the compensation methods.

Chapter 6: Ad Hoc Approach Powertrain Control with Backlash and Time Delay

The last chapter presents first results of merging the control methods for backlash and time delay in order to enable controlled backlash traversing with time delay. A switching controller is used to combine the control concepts. First simulation results show stable, fast, and comfortable backlash traversing. Analysis regarding parameter uncertainties and disturbances are left for future work and the presented approach is rather a first outlook in this direction.

7.2 Outlook

The presented control approaches to reduce driveline oscillations can be applied to a wide range of powertrain types. Further work is planned to validate the presented backlash and time delay approaches by more vehicle experiments with various powertrain types. Particularly, the presented smooth feedforward controller for backlash traversing and state prediction method to compensate time delay are promising for application, since they are easy to implements.

Another important question for future studies is to evaluate the derived control methods for vibrations with higher frequencies such as in the case of powertrains with internal combustion engine, where the powertrain can be excited by the rotational irregularity of the crankshaft. These frequencies, originating by combustion engine, are generally higher than 20 Hz and enhance the problems of time delay in controlled systems due to a reduced time delay margin. It remains to be identified how robust the presented time delay compensation methods are regarding higher frequencies. Furthermore, the impact of backlash to these systems should be further explored. For instance undesired rattling may occur in idle speed, which can be caused by the irregularity of the crankshaft.

An important question for future studies is also to determine and enhance the robustness of the presented dead time compensation methods with respect to model uncertainties and disturbances. Possible direction can be adaptive methods, since the presented controllers depends on accurate control models. Finally, the ad hoc approach for powertrains with backlash and time delay remains to be further investigated. Stability of the switching system should be explored in future work.

Bibliography

[AngeringerHornReichhartinger12] Angeringer, U.; Horn, M.; Reichhartinger, M.: Drive Line Control for Electrically Driven Vehicles Using Generalized Second Order Sliding Modes. In IFAC Proceedings Volumes, Vol. 45, pp. 79–84, 2012.

[AwadallahEtAl17] Awadallah, M.; Tawadros, P.; Walker, P.; Zhang, N.: Dynamic modelling and simulation of a manual transmission based mild hybrid vehicle. Mechanism and Machine Theory, Vol. 112, pp. 218–239, 2017.

[Barra16] Barra, M.: Your car will become a second office in 5 years or less, General Motors CEO predicts. Business Insider, 2016.

[BaumannEtAl06] Baumann, J.; Torkzadeh, D.D.; Ramstein, A.; Kiencke, U.; Schlegl, T.: Model-based predictive anti-jerk control. Control Engineering Practice, Vol. 14, No. 3, pp. 259–266, 2006.

[BayindirGözüküçükTeke11] Çağatay Bayindir, K.; Gözüküçük, M.A.; Teke, A.: A comprehensive overview of hybrid electric vehicle: Powertrain configurations, powertrain control techniques and electronic control units. Energy Conversion and Management, Vol. 52, No. 2, pp. 1305–1313, 2011.

[BoveeRizzoni16] Bovee, K.; Rizzoni, G.: Model-Based Torque Shaping for Smooth Acceleration Response in Hybrid Electric Vehicles. In IFAC-PapersOnLine, Vol. 49, pp. 525–532, 2016.

[Brogliato18] Brogliato, B.: Feedback control of multibody systems with joint clearance and dynamic backlash: a tutorial. Multibody System Dynamics, Vol. 42, No. 3, pp. 283–315, 2018.

[BruceEgardtPettersson05] Bruce, M.; Egardt, B.; Pettersson, S.: On powertrain oscillation damping using feedforward and LQ feedback control. In Proceedings of 2005 IEEE International Conference on Control Applications, pp. 1415–1420, 2005.

[ByrnesIsidori88] Byrnes, C.I.; Isidori, A.: Local stabilization of minimum-phase nonlinear systems. Systems & Control Letters, Vol. 11, No. 1, pp. 9–17, 1988.

[ByrnesIsidori91] Byrnes, C.I.; Isidori, A.: Asymptotic stabilization of minimum phase nonlinear systems. IEEE Transactions on Automatic Control, Vol. 36, No. 10, pp. 1122–1137, 1991.

[CAR12] CAR: Modellvielfalt bei Autobauern explodiert. Study of CAR Center Automotive Research, University of Duisburg-Essen, 2012.

[ChanBouscayrolChen10] Chan, C.C.; Bouscayrol, A.; Chen, K.: Electric, Hybrid, and Fuel-Cell Vehicles: Architectures and Modeling. IEEE Transactions on Vehicular Technology, Vol. 59, No. 2, pp. 589–598, 2010.

[DolciniWitBéchart10] Dolcini, P.J.; Canaudas-de Wit, C.; Béchart, H.: Dry Clutch Control for Automotive Applications. Springer, 2010.

[DresigFidlin14] Dresig, H.; Fidlin, A.: Schwingungen mechanischer Antriebssysteme: Modellbildung, Berechnung, Analyse, Synthese. Springer, 2014.

[DresigRockhausenHolzweißig13] Dresig, H.; Rockhausen, L.; Holzweißig, F.: Maschinendynamik. Springer, 2013.

[EmadiLeeRajashekara08] Emadi, A.; Lee, Y.J.; Rajashekara, K.: Power Electronics and Motor Drives in Electric, Hybrid Electric, and Plug-In Hybrid Electric Vehicles. IEEE Transactions on Industrial Electronics, Vol. 55, No. 6, pp. 2237–2245, 2008.

[ErikssonNielsen14] Eriksson, L.; Nielsen, L.: Driveline Control. John Wiley & Sons, Ltd, 2014.

[Ferdinand06] Ferdinand, S.: Zero Dynamics of Linear and Nonlinear Systems: Definitions, Properties and Applications. at - Automatisierungstechnik, Vol. 54, No. 7, pp. 310–322, 2006.

[FidlinSeebacher06] Fidlin, A.; Seebacher, R.: DMF Simulation Techniques. In Proceedings of 8th LuK Symposium, pp. 55–71, 2006.

[FischerEtAl16] Fischer, R.; Kücükay, F.; Jürgens, G.; Pollak, B.: Das Getriebebuch. Springer, 2016.

[FliessEtAl92] Fliess, M.; Lévine, J.; Martin, P.; Rouchon, P.: On differentially flat nonlinear systems. Nonlinear Control Systems Design, pp. 408–412, 1992.

[FliessEtAl95] Fliess, M.; Lévine, J.; Martin, P.; Rouchon, P.: Flatness and defect of non-linear systems: Introductory theory and examples. International Journal of Control, Vol. 61, No. 6, pp. 1327–1361, 1995.

[FranklinPowellEmami-Naeini15] Franklin, G.; Powell, J.; Emami-Naeini, A.: Feedback Control of Dynamic Systems. Pearson Education Limited, 2015.

[FranklinPowellWorkman98] Franklin, G.; Powell, J.; Workman, M.: Digital control of dynamic systems. Addison Wesley Longman, 1998.

[Gillespie92] Gillespie, T.: Fundamentals of Vehicle Dynamics. SAE International, 1992.

[GolkaniEtAl17] Golkani, M.A.; Steinberger, M.; Bachinger, M.; Rumetshofer, J.; Stolz, M.; Horn, M.: Optimal Gear Shift Strategy for Dual Clutch Transmissions. In IFAC-PapersOnLine, Vol. 50, pp. 4800–4805, 2017.

[GraichenHagenmeyerZeitz05] Graichen, K.; Hagenmeyer, V.; Zeitz, M.: A new approach to inversion-based feedforward control design for nonlinear systems. Automatica, Vol. 41, No. 12, pp. 2033–2041, 2005.

[GrotjahnQuernheimZemke06] Grotjahn, M.; Quernheim, L.; Zemke, S.: Modelling and identification of car driveline dynamics for anti-jerk controller design. In Proceedings of 2006 IEEE International Conference on Mechatronics, pp. 131–136, 2006.

[HagenmeyerZeitz09] Hagenmeyer, V.; Zeitz, M.: Flatness-based Design of Linear and Nonlinear Feedforward Controls. at - Automatisierungstechnik, Vol. 52, No. 1, pp. 3–12, 2009.

[HajduInsperger16] Hajdu, D.; Insperger, T.: Demonstration of the sensitivity of the Smith predictor to parameter uncertainties using stability diagrams. International Journal of Dynamics and Control, Vol. 4, No. 4, pp. 384–392, 2016.

[Haschka MarkusVolker07] Haschka Markus, S.; Volker, K.: Observing the Torque of a Powertrain with Backlash. at - Automatisierungstechnik, Vol. 55, No. 3, pp. 127–135, 2007.

[InspergerStépán11] Insperger, T.; Stépán, G.: Semi-Discretization for Time-Delay Systems: Stability and Engineering Applications. Springer, 2011.

[InspergerStépán02] Insperger, T.; Stépán, G.: Semi-discretization method for delayed systems. International Journal for Numerical Methods in Engineering, Vol. 55, No. 5, pp. 503–518, 2002.

[Isidori95] Isidori, A.: Nonlinear Control Systems. Springer, 1995.

[JauchEtAl18] Jauch, C.; Tamilarasan, S.; Bovee, K.; Güvenc, L.; Rizzoni, G.: Modeling for drivability and drivability improving control of HEV. Control Engineering Practice, Vol. 70, pp. 50–62, 2018.

[JoachimHorwathReuss08] Joachim, C.; Horwath, J.; Reuss, H.C.: Ein Verfahren zum Unterdrücken von Triebstrangschwingungen bei schweren Nutzfahrzeugen mit automatisiertem Schaltgetriebe. In Proceedings of 14th Stuttgart International Symposium, 2008.

[JoachimReussHorwath09] Joachim, C.; Reuss, H.C.; Horwath, J.: An example for the use of adaptive methods in powertrain control of heavy duty vehicles. Application of torque control functions for optimized gear shifting. In Proceedings of 2009 VDI International Congress Drivetrain for Vehicles, 2009.

[Karle16] Karle, A.: Elektromobilität: Grundlagen und Praxis. Carl Hanser Verlag GmbH & Company KG, 2016.

[Karlsson01] Karlsson, J.: Powertrain Modelling and Control for Driveability in Rapid Transients. Licentiate Thesis, Chalmers University of Technology, 2001.

[KhajepourFallahGoodarzi14] Khajepour, A.; Fallah, M.; Goodarzi, A.: Electric and Hybrid Vehicles: Technologies, Modeling and Control - A Mechatronic Approach. Wiley, 2014.

[KienckeNielsen05] Kiencke, U.; Nielsen, L.: Automotive Control Systems: For Engine, Driveline, and Vehicle. Springer, 2005.

[Kirchner07] Kirchner, E.: Leistungsübertragung in Fahrzeuggetrieben: Grundlagen der Auslegung, Entwicklung und Validierung von Fahrzeuggetrieben und deren Komponenten. Springer, 2007.

[Kirk12] Kirk, D.: Optimal Control Theory: An Introduction. Dover Publications, 2012.

[KnotheStichel16] Knothe, K.; Stichel, S.: Rail Vehicle Dynamics. Springer, 2016.

[KumPengBucknor11] Kum, D.; Peng, H.; Bucknor, N.K.: Supervisory Control of Parallel Hybrid Electric Vehicles for Fuel and Emission Reduction. Journal of Dynamic Systems, Measurement, and Control, Vol. 133, No. 6, 2011.

[Lagerberg01] Lagerberg, A.: A literature survey on control of automotive powertrains with backlash, 2001.

[LagerbergEgardt05] Lagerberg, A.; Egardt, B.: Model Predictive Control Of Automotive Powertrains With Backlash. In IFAC Proceedings Volumes, Vol. 38, pp. 1–6, 2005.

[LagerbergEgardt07] Lagerberg, A.; Egardt, B.: Backlash Estimation With Application to Automotive Powertrains. IEEE Transactions on Control Systems Technology, Vol. 15, No. 3, pp. 483–493, 2007.

[Levine10] Levine, W.: The Control Handbook, Second Edition. CRC Press, 2010.

[Liberzon03] Liberzon, D.: Switching in Systems and Control. Systems & Control: Foundations & Applications. Birkhäuser, 2003.

[LiberzonMorse99] Liberzon, D.; Morse, A.S.: Basic problems in stability and design of switched systems. IEEE Control Systems, Vol. 19, No. 5, pp. 59–70, 1999.

[Luenberger64] Luenberger, D.G.: Observing the State of a Linear System. IEEE Transactions on Military Electronics, Vol. 8, No. 2, pp. 74–80, 1964.

[Lunze12] Lunze, J.: Regelungstechnik 1: Systemtheoretische Grundlagen, Analyse und Entwurf einschleifiger Regelungen. Berlin: Springer, 2012.

[Lunze16] Lunze, J.: Regelungstechnik 2: Mehrgrößensysteme, Digitale Regelung. Springer, 2016.

[MagnusPoppSextro13] Magnus, K.; Popp, K.; Sextro, W.: Schwingungen: Physikalische Grundlagen und mathematische Behandlung von Schwingungen. Springer, 2013.

[Matthes05] Matthes, B.: Dual Clutch Transmissions - Lessons Learned and Future Potential. In SAE 2005 World Congress & Exhibition, SAE International, 2005.

[MencherEtAl14] Mencher, B.; Gollin, W.; Reiter, F.; Glaser, A.; Landhäußer, F.; Lerchenmüller, K.; Boebel, D.; Hamm, M.; Spingler, T.; Niewels, F.; Ehret, T.; Nenninger, G.; Knoll, P.; Kuttenberger, A.: In Fundamentals of Automotive and Engine Technology: Overview of electrical and electronic systems in the vehicle, pp. 158–160. Springer, 2014.

[NaunheimerBertscheLechner07] Naunheimer, H.; Bertsche, B.; Lechner, G.: Fahrzeuggetriebe: Grundlagen, Auswahl, Auslegung und Konstruktion. Springer, 2007.

[NjehCauetCoirault11] Njeh, M.; Cauet, S.; Coirault, P.: LPV control of ICE torque ripple in hybrid electric vehicles. In IFAC Proceedings Volumes, Vol. 44, pp. 2931–2936, 2011.

[NordinGalic'Gutman97] Nordin, M.; Galic', J.; Gutman, P.O.: New models for backlash and gear play. International Journal of Adaptive Control and Signal Processing, Vol. 11, pp. 49–63, 1997.

[NordinGutman02] Nordin, M.; Gutman, P.O.: Controlling mechanical systems with backlash–a survey. Automatica, Vol. 38, No. 10, pp. 1633–1649, 2002.

[Normey-Rico07] Normey-Rico, J.: Control of Dead-time Processes. Springer, 2007.

[Pacejka12] Pacejka, H.: Tire and Vehicle Dynamics. Elsevier Science, 2012.

[Palmor80] Palmor, Z.: Stability properties of Smith dead-time compensator controllers. International Journal of Control, Vol. 32, No. 6, pp. 937–949, 1980.

[PetterssonNielsen00] Pettersson, M.; Nielsen, L.: Gear shifting by engine control. IEEE Transactions on Control Systems Technology, Vol. 8, No. 3, pp. 495–507, 2000.

[PhamBushnell15] Pham, T.; Bushnell, L.: Two-degree-of-freedom damping control of driveline oscillations caused by pedal tip-in maneuver. In Proceedings of 2015 American Control Conference, pp. 1425–1432, 2015.

[PhamEtAl16] Pham, T.; Seifried, R.; Hock, A.; Scholz, C.: Nonlinear Flatness-Based Control of Driveline Oscillations for a Powertrain with Backlash Traversing. In IFAC-PapersOnLine, Vol. 49, pp. 749–755, 2016.

[PhamEtAl17] Pham, T.; Seifried, R.; Scholz, C.; Bofinger, G.: Driveline Control – Intelligent Actuator Inputs to Improve Component Protection, Performance and Comfort. In Proceedings of 17th VDI International Congress Drivetrain for Vehicles, 2017.

[PhamScholzRoulet16] Pham, T.; Scholz, C.; Roulet, T.: Verfahren zur Steuerung eines Antriebsaggregats. DPMA Patent No. DE102016113326.4, 2016.

[PhamScholzSeifried17] Pham, T.; Scholz, C.; Seifried, R.: Anti-Jerk Control of a Parallel Hybrid Electrified Vehicle with Dead Time. In IFAC-PapersOnLine, Vol. 50, pp. 966–971, 2017.

[PiazziVisioli01] Piazzi, A.; Visioli, A.: Optimal noncausal set-point regulation of scalar systems. Automatica, Vol. 37, No. 1, pp. 121–127, 2001.

[Pistoia10] Pistoia, G.: Electric and Hybrid Vehicles: Power Sources, Models, Sustainability, Infrastructure and the Market. Elsevier, 2010.

[PwC13] PwC: Spotlight on Automotive. Interim update global semiconductor trends – special focus automotive industry, PwC Semiconductor Report, 2013.

[RainerFrankDirk10] Rainer, G.; Frank, H.; Dirk, A.: Flatness Based Feedforward Control of a Parallel Hybrid Drivetrain. at - Automatisierungstechnik, Vol. 58, No. 10, pp. 560–567, 2010.

[Richard03] Richard, J.P.: Time-delay systems: an overview of some recent advances and open problems. Automatica, Vol. 39, No. 1, pp. 1667–1694, 2003.

[Rudolph05] Rudolph, J.: Flatness: A useful Property also for Systems with Delays. at - Automatisierungstechnik, Vol. 53, No. 1, 2005.

[SchiehlenEberhard14] Schiehlen, W.; Eberhard, P.: Technische Dynamik: Rechnergestützte Modellierung mechanischer Systeme im Maschinen- und Fahrzeugbau. Springer, 2014.

[Schlecht09] Schlecht, B.: Maschinenelemente 2. Bd. 2. Pearson Studium, 2009.

[SchrammHillerBardini10] Schramm, D.; Hiller, M.; Bardini, R.: Modellbildung und Simulation der Dynamik von Kraftfahrzeugen. Springer, 2010.

[SciarrettaGuzzella07] Sciarretta, A.; Guzzella, L.: Control of hybrid electric vehicles. IEEE Control Systems, Vol. 27, No. 2, pp. 60–70, 2007.

[SipahiEtAl11] Sipahi, R.; i. Niculescu, S.; Abdallah, C.T.; Michiels, W.; Gu, K.: Stability and Stabilization of Systems with Time Delay. IEEE Control Systems, Vol. 31, No. 1, pp. 38–65, 2011.

[Sira-RamírezAgrawal04] Sira-Ramírez, H.; Agrawal, S.K.: Differentially Flat Systems. CRC Press, 2004.

[Smith57] Smith, O.J.: Closer Control of Loops with Dead Time. Chemistry Engineering Progress, Vol. 53, No. 5, pp. 217–219, 1957.

[Sommer17] Sommer, S.: Driver or be Driven? About new Requirements for the Transmission Industry - and Change as a Chance. Speech presented at the 17th VDI International Congress Drivetrain for Vehicles, 2017.

[Speidel17] Speidel, S.: Conceptual design of feedforward and feedback control of low load changes with backlash traversing. Master's thesis, University of Stuttgart, 2017.

[Stépán89] Stépán, G.: Retarded Dynamical Systems: Stability and Characteristic Functions. Pitman research notes in mathematics series. Longman Scientific & Technical, 1989.

[TemplinEgardt09] Templin, P.; Egardt, B.: An LQR torque compensator for driveline oscillation damping. In Proceedings of 2009 IEEE International Conference on Control Applications, pp. 352–356, 2009.

[TemplinEgardt11] Templin, P.; Egardt, B.: A Powertrain LQR-Torque Compensator with Backlash Handling. Oil & Gas Science and Technology, Vol. 66, No. 4, pp. 645–654, 2011.

[TraubMaierBarbehön17] Traub, M.; Maier, A.; Barbehön, K.L.: Future Automotive Architecture and the Impact of IT Trends. IEEE Software, Vol. 34, No. 3, pp. 27–32, 2017.

[Unbehauen07] Unbehauen, H.: Regelungstechnik II: Zustandsregelungen, digitale und nichtlineare Regelsysteme. Vieweg+Teubner Verlag, 2007.

[VadamaluBeidl16] Vadamalu, R.S.; Beidl, C.: MPC for Active Torsional Vibration Reduction of Hybrid Electric Powertrains. In IFAC-PapersOnLine, Vol. 49, pp. 756–761, 2016.

[WallentowitzFreialdenhoven11] Wallentowitz, H.; Freialdenhoven, A.: Strategien zur Elektrifizierung des Antriebsstranges: Technologien, Märkte und Implikationen. Vieweg+Teubner Verlag, 2011.

[WilliamsLawrence07] Williams, R.; Lawrence, D.: Linear State-Space Control Systems. John Wiley & Sons, 2007.

[Zeitz10] Zeitz, M.: Differential flatness: A useful method also for linear SISO systems. at - Automatisierungstechnik, Vol. 58, No. 1, pp. 5–13, 2010.